New Electrochemical Strategies for Studying Single Nanoparticles

Peter Aaron Defnet

A dissertation

submitted in partial fulfillment of the

requirements for the degree of

Doctor of Philosophy

University of Washington

2021

Reading Committee:

Bo Zhang, Chair

Joshua Vaughan

Ashleigh Theberge

Program Authorized to Offer Degree:

Chemistry

University of Washington

Abstract

New Electrochemical Strategies for Studying Single Nanoparticles

Peter Aaron Defnet

Chair of the Supervisory Committee:
Professor Bo Zhang
Department of Chemistry

This dissertation describes new advances and applications of single nanoparticle collision electrochemistry and is divided into two broad sections. First, new methods are described to overcome longstanding limitations of the collision technique, ranging from expanding the allowable detection conditions to obtaining more accurate single nanoparticle structural characterization measurements. For example, Chapter 2 describes a novel strategy to measure single particle collisions in conditions almost three orders of magnitude more concentrated than previously attainable. This technique facilitated the discovery of a novel process to measure the electroactive surface areas of single platinum nanoparticles. Further, Chapter 3 describes an electrode modification procedure that promotes the adhesion of colliding silver nanoparticles and facilitates their complete oxidative dissolution. This work yielded accurate volumetric

measurements for single silver nanoparticles up to 100 nm in diameter, which is improved from the previous limit of 60 nm.

The second half of the dissertation develops new applications for closed-bipolar electrochemical imaging, a methodology that enables the widescale mapping of redox environments with wireless electrode arrays. Chapter 4 demonstrates the first reported optical detection of short-lived transient events using closed-bipolar imaging in which platinum nanoparticle collisions catalyzing the hydrogen evolution reaction are employed as the source of transient electron transfer. Chapter 5 shows progress toward the optical detection of transient oxidative events using silver nanoparticle oxidative collisions as a model system toward the future goal of mapping biological exocytosis *in-vitro*. Lastly, Chapter 6 demonstrates the spatial mapping of multiple electrochemical processes using a massive array of closed-bipolar electrodes in conjunction with electrochemiluminescence imaging.

TABLE OF CONTENTS

LIST OF FIGURES

LIST OF TABLES

ACKNOWLEDGEMENTS

I would first like to thank my research advisor Professor Bo Zhang for his mentorship and guidance throughout my stay at UW. I have always been inspired by your love for science, which was especially evident in our research meetings. Your excitement for new results was a strong motivator for me. Further, I most appreciated your advice given in my first year, which was to enjoy this time and explore – or as you called it – "to play" in the lab. I truly believe it was the free and supportive work environment you created that allowed me to flourish into the scientist that I am today.

I'd also like to thank my committee members, Josh Vaughan, Ashleigh Theberge, and Xiaohu Gao, for their continued support. Specifically, to Josh Vaughan for inviting me to his lab to learn about high temporal resolution optical imaging, which laid the groundwork for Chapter 4.

To Todd Anderson, with whom I worked very closely with over the 2nd half of my Ph.D. It was a true pleasure working alongside you. As we often remarked, our strengths complement each other well. Thank you, too, for being a good friend; for inviting me to your parent's Thanksgiving, for making bets to keep things lively, and for your humor and wit towards helping make the lab a genuinely fun place to be.

To Chris Gunderson for our many lunches, sushi happy hours, and hikes together, which continued even after you graduated. To Steve Percival and Steve Oja for taking me under your wing during my early summer start to grad school. Memories of Seattle's International Beer Fest hold a special place in my heart. And to all other members of that Zhang Lab; whose contributions to my learning and growth are immeasurable.

I'd especially like to thank my Mom, Jenny, and two sisters Amy and Emily, for each playing a role in making me feel loved and supported, despite being thousands of miles away.

Lastly, to you (the reader) whose continued interest I appreciate. It is for you that I will pass on the mantra that I have found most useful in research. That is, above all else, to stay curious.

I close with a quote that I discovered in my 1st quarter at UW, which I have found most appropriate.

> *"Physical concepts are free creations of the human mind, and are not, however they may seem, uniquely determined by the external world. In our endeavor to understand reality we are somewhat like a man trying to understand the mechanism of a closed watch. He sees the face and the moving hands, even hears its ticking, but he has no way to open the case. If he is ingenious he may form some picture of a mechanism which could be responsible for all of the things he observes, but he may never be quite sure his picture is the only one which could explain his observations. He will never be able to compare his picture with the real mechanism and he cannot even imagine the possibility or the meaning of such a comparison. But he certainly believes that, as his knowledge increases, his picture of reality will become simpler and simpler and will explain a wider and wider range of his sensuous impressions. He may also believe in the existence of the ideal limit of knowledge and that it is approached by the human mind. He may call this ideal limit the objective truth."*

Albert Einstein and Leopold Infeld, 1938.

Quoted from "The Evolution of Physics: From Early Concepts to Relativity and Quanta" (New York: Simon and Schuster, 1966), p. 31. Originally published 1938.

Chapter 1. INTRODUCTION

1.1 SINGLE NANOPARTICLE COLLISION ELECTROCHEMISTRY

Nanoparticles (NPs) have myriad applications in industry, ranging from serving as electrocatalysts in electrochemical fuel cells[1,2] to use as anti-bacterial agents in consumer products.[3] They have advantageous chemical properties including enhanced reactivity over their equivalent bulk materials given their high surface area to volume ratio.[4] Yet the properties of each individual particle can vary from the ensemble response based on their precise physical structure. Small changes in shape, size, volume, and porosity, can produce unique chemical behaviors.[5–8] Thus, there remains a demand for analytical methods that can accurately characterize nanoparticles on a single entity scale.

Electrochemistry is well-poised as an analytical tool quite advantageous to this end due to its relative ease in detecting current signals from individual nanomaterials. A well-known electrochemical technique called 'nanoparticle collision' has been thoroughly demonstrated as a method capable of detecting single nanoparticle electron transfer.[9,10] The technique biases a bare ultramicroelectrode (UME) at a potential sufficient to drive a desired redox reaction across a single diffuse NP interacting, or 'colliding', with the electrode surface. Measured signal may result from direct particle oxidation,[11] NP-driven electrocatalysis,[12,13] or simply blocking an ongoing faradaic process.[14,15] Specific applications range from investigating single particle reactivity,[16,17] incorporation into nanoscale biosensors,[18,19] analytical methods for single particle size determination,[20,21] and studies elucidating physical mechanisms describing the NP-electrode interaction.[22,23]

In the early days of nanoparticle collision beginning with Bard's seminal papers in 2007,[13] physical models were created to simulate the behavior of the NP-electrode interaction.[24] A simplistic perspective was initially taken whereby nanoparticles were treated as separate objects diffusing in solution. While the particle's movement was treated as a random walk, the average collision frequency could be predicted using a series of known parameters. These include the diffusion coefficient of the nanoparticle, *D*, the bulk concentration of NP's, *C*, the radius of the electrode, *r*, and Avogadro's number, N_A. Equation 1 relates these parameters to the rate of collision, *f*, and importantly assumes that particles adhere to the electrode upon landing.[25]

$$f = 4DCrN_A \quad (1)$$

Thirdly, nanoparticles were treated as perfect spheres to easily estimate expected behaviors, such as diffusion-limited mass transport to an adsorbed particle and expected particle volume. Overall, these simplified models provided a strong scaffold to describe the observed collision behavior.

However, problems arose, likely influenced by researchers following these assumptions without question. For example, in 2011 Compton and co-workers published a seminal work describing the collision and oxidation behavior of single silver nanoparticles.[26] Impacting particles generated single oxidative amperometric current spikes for what was envisioned as a particle landing, sticking, and dissolving via full oxidation. Their proposed mechanism precisely followed the early assumptions by Bard and co-workers, namely that particles followed a simple diffusion-limited path, adhered to the electrode, and were fully oxidized. With this mechanism in mind, Ag NP oxidative collisions were reported as a volumetric determination procedure more accurate than dynamic light scattering for particles >10 nm in diameter.[27] A series of follow-up papers were

subsequently published by Compton and co-workers exploring a vast parameter space varying the electrolyte identity,[28] electrolyte concentration,[29] capping agent,[30,31] and even other materials including Ni,[32] Cu,[33] Au,[34,35] and organic particles.[36,37] Importantly, full oxidation was claimed in all cases for Ag NP's ranging from 10 – 50 nm,[27,28] and even for NP aggregates upward to 150 nm in one case.[38]

In 2017, however, three articles utilizing up to 100x higher temporal resolution electrochemical recordings instead observed 'multipeak' collision behavior consisting of rapid successive small peaks separated by millisecond spacing.[39,40,41] These findings were indicative of a more accurate nano-motion mechanism due to the NP rapidly bouncing across the electrode surface. Simulations have suggested the nanoparticle only contacts the electrode in rapid nanosecond-scale bursts due to its fast diffusional motion.[42,43] Importantly, the multipeak papers also reported that particles greater than 50 nm diameter underwent incomplete oxidation due to the high probability of the NP diffusing away from the electrode before fully oxidizing.

The multipeak papers sparked new interest in the field to better understand the precise mechanism guiding the NP motion. Research activity continued utilizing both high-resolution amperometry,[16,44,45] as well as with the incorporation of correlated optical and spectroscopic techniques providing added spatial and chemical information, respectively.[17,46–49] Of particular interest is active discussion regarding the true mechanism for incomplete oxidation of Ag NP's, keeping in mind that if this can be overcome then a powerful technique exists for Ag NP volumetric determination for all sizes. While the multipeak papers reported the mechanism was due to the high probability of partially oxidized particles diffusing away from the electrode, new studies with correlated microscopy were beginning to show that more factors were at play.

For example, use of NP-tracking with 3-D holography has shown that the oxidation of a NP may not commence immediately upon landing.[50] More simply, it suggests that physical contact does not guarantee electrochemical activity. This conclusion was initially doubted since the error margin for 3-D holography is ~10 nm, making it difficult to definitively state whether the particle was in contact. Yet, a series of papers from Wang et al. have convincingly demonstrated this same behavior.[51,52] They employed nano-objects embedded with a redox-active dye whose electrochemical activity can be optically measured. They showed that objects resting on electrodes can maintain such poor electrical contact that electron transfer does not occur. Thus Sun et al. suggests that the multipeak mechanism could plausibly be a result of a stationary NP oscillating between active and non-active states via micro-convection.[53]

We consider one last mechanism that could reasonably prevent full Ag NP oxidation. Both Compton and co-workers and the multipeak papers assumed that the product Ag^+ species were fully soluble in the bulk aqueous medium. Yet, a few studies have instead reported that the large injection of Ag^+ into nearby solution forces the precipitation of Ag-salts either directly onto the particle itself, or onto the nearby electrode. For example, Mckelvey et al. used an adjustable microgap between two opposing microelectrodes with opposite biases to oxidize a colliding particle and subsequently reduce the generated Ag^+.[45] Interestingly, they found that only 50% of the oxidized Ag NP is released as free Ag^+, suggesting the formation of an insoluble complex such as Ag_2O. Separately, Sundaresan et al. used DFM-electrochemistry and noticed Ag_2O particles forming several microns away on the electrode surface following the oxidation and dissolution Ag NPs.[54] A direct consequence of Ag-salt precipitation is that a partially oxidized NP can be encapsulated by insoluble Ag-salts and prevent further oxidation. Such behavior is directly

reported by Robinson et al., who directly validated this mechanism with the characterization of encapsulated NPs with transmission electron microscopy.[55]

Thus, the achievement of full Ag NP oxidation would require a clever experimental design that overcomes possible diffusional motion of partially oxidized Ag NPs, improves NP electrical contact, and prevents NP encapsulation via Ag-salt saturation. In a stroke of scientific serendipity, as described in Chapter 3, I discovered a simple method to overcome each of these problems with two experimental adaptations. The method began as a strategy to overcome the issue of Ag-salt saturation by introducing Lewis bases into the bulk electrolyte solution. Lewis bases form complex ions with Ag^+ and increase the Ag-salt solubility by a factor equivalent to their formation constant, K_f. In Chapter 3 I used $Na_2S_2O_3$ ($K_f = 1.8 \times 10^{13}$) thus increasing the Ag-salt solubility by 13 orders of magnitude. Yet I was pleasantly surprised when I found that $Na_2S_2O_3$ also undergoes electro-oxidation at the same potential required to oxidize Ag NPs, resulting in a thin sulfurous layer deposited across the Au electrode surface.[56] This sulfur layer both adheres colliding Ag NP's and directly reacts with the Ag as a preconcentrated electrolyte to form Ag_2S.

Overall, the sulfurous adhesion layer overcomes the problem of NP diffusional motion at the electrode, the bulk $Na_2S_2O_3$ overcomes the Ag-salt precipitation issue, and the preconcentrated Ag_2S promotes NP reactivity immediately upon landing. Results show a 25x increase in collision frequency, suggesting that use of a sulfide adhesion layer may overcome issues of reactivity associated with poor electrical contact. Further, convincing results demonstrate full particle oxidation up to 100 nm diameter, well surpassing the previous 50 nm threshold, and showcasing a new methodology for accurate single Ag NP quantitation.

1.2 Overcoming Nanoparticle Aggregation

The next chapter tackles the issue of nanoparticle aggregation, a commonly reported behavior occurring within diffusion-limited single particle measurements. If we revisit our mechanistic picture of a particle landing onto an electrode, we have thus far assumed the arrival of single particles. Yet it is often reported in literature that aggregates, or multi-particle clusters, may form due to incompatible solution conditions.[57,58] Specifically, citrate-capped nanoparticles rely on maintaining an overall electrostatic negative charge to repel neighboring particles in solution and thus remain single entities. Neutralization of the particle's surface charge via either protonation in pH environments lower than the pKa of citrate (3.13),[59] or charge screening due to high salt concentrations (>20 mM) leads to particles adhering to their neighbors and forming large clusters.[57] The behavior is instead largely viewed as a negative consequence given that the desired single particle attribute is no longer maintained. Thus, the detection of diffuse single citrate-capped nanoparticles is limited to the parameter space bounded by the bulk solution maintaining a pH greater than 3.13 and less than 20 mM ionic salt. Such conditions are often adhered to, though can be quite limiting particularly in the study of electrocatalytic nanoparticles considering that their equivalent industrial environment often extends below pH 1.[60]

In Chapter 2 I design a new methodology to enable the detection of NP collision events in highly concentrated solutions (demonstrated up to 750 mM), without observing significant particle aggregation.[61] The technique employs pressure-driven flow to deliver nanoparticles to the electrode while limiting the duration for which they are exposed to the aggregate-inducing solution to a few milliseconds. As a result, the available parameter space is vastly widened to include low pH and highly concentrated solutions. This new strategy has aided in the discovery of a new methodology to measure the electroactive surface area of single Pt NPs. High resolution

amperometric measurements revealed a new peak shape due to the temporal resolution of the two-step hydrogen evolution reaction. Quantitation of the first adsorption peak yields electroactive surface area measurements for single particles. Results suggest that more accurate surface area values are obtained for measurement in higher acid concentrations, previously unattainable without the newly developed pressure-driven methodology.

1.3 Closed-Bipolar Electrochemical Imaging

In Chapters 4-6 we pivot towards talking about an entirely different electrochemical topic, known as closed-bipolar electrochemical imaging (c-BPI). A closed-bipolar electrode (c-BPE) is composed of a conductive material embedded in an insulating membrane whereby both poles of the conductor are exposed to separate solutions.[62] The c-BPE is wirelessly addressed such that potential is applied across two driving electrodes positioned in each solution, but not in direct contact with the conductor. The potential drop occurs predominantly at the c-BPE interface and couples complementary half reactions at both poles.[63] The electrons generated at the oxidative pole are transferred directly across the c-BPE to fuel the complementary reductive process. Thus, equivalent amounts of both redox reactions occur to complete the circuit.

The same experimental setup employed for a single c-BPE can be extended toward arrays with *n* c-BPE's positioned in parallel. The same principle applies whereby complementary half reactions are driven at each individual pole since the potential drops across each of them uniformly. However, given that the current is measured at the two driving electrodes, any individual signals measured by each of the n-electrodes is aggregated to a single electrochemical trace. Instead, single electrode spatial resolution within c-BPE arrays is facilitated using a redox-induced light generating reaction. For example, an oxidative process of interest could be coupled to a reductive light generation mechanism on the opposite pole. Individual recording channels for each electrode

are created in the corresponding microscope video, measured as light generated over time at each individual electrode position. Thus, the power of c-BPI is that potential applied across a single set of driving electrodes can wirelessly enable the recording of thousands of individual channels separated in space.

The two common light-generation mechanisms employed in literature are that of redox-induced fluorescence and electrochemiluminescence (ECL). Redox-induced fluorescence typically "turns-on" a fluorophore with the application of potential, transforming a non-fluorescent precursor to a fluorescent species.[64] It is quite advantageous due to its high sensitivity, where a single fluorophore can emit many photons upon stimulation with its excitation source. Given that specialized optical methods can measure single fluorophores,[65] the limit of detection (LOD) for the c-BPI could in theory be extended toward the single electron transfer level. However, one significant drawback is the unbound mass transfer of the fluorophore following its production. Diffusional overlap of fluorophores in array-based imaging schemes can complicate the interpretation of deciding which electrode generated which signal.[66] Instead, fluorophores should ideally be localized to their generation electrode. Both our lab and others are currently in active development of strategies to overcome this issue.

ECL is the second common light generation mechanism employed in c-BPI. The present discussion will focus on anodic ECL, however, cathodic ECL is described in Chapter 5. Anodic ECL proceeds through a multi-step radical mechanism requiring a luminophore $Ru(bpy)_3^{2+}$ and a co-reactant.[67] The selected co-reactant needs to generate a strong reducing agent upon electrochemical oxidation, which will react with the oxidized $Ru(bpy)_3^{2+}$ species to form an unstable radical that emits a single photon upon relaxation. While there are many identified co-reactants, including tripropylamine, and 2-(dibutylamino)ethanol (DBAE),[68] the work herein

utilizes DBAE due to its superior light-generation properties.[69] The multistep radical light-generation mechanism between $Ru(bpy)_3^{2+}$ and DBAE is shown below.[70]

$$Ru(bpy)_3^{2+} - e^- \rightarrow Ru(bpy)_3^{3+} \quad (1)$$

$$DBAE - e^- \rightarrow [DBAE^{\cdot}]^+ \quad (2)$$

$$[DBAE^{\cdot}]^+ \rightarrow DBAE^{\cdot} + H^+ \quad (3)$$

$$Ru(bpy)_3^{3+} + DBAE^{\cdot} \rightarrow Ru(bpy)_3^{2+*} + \text{products} \quad (4)$$

$$Ru(bpy)_3^{2+*} \rightarrow Ru(bpy)_3^{2+} + h\nu \quad (5)$$

ECL is advantageous in c-BPI with regards to its spatial resolution given that only a single photon is emitted directly at the electrode surface whereby proper chemical mixing occurs. The mechanism does not allow for diffusional broadening as in redox-induced fluorescence. However, its main limitation is its relative lack of sensitivity. Not all oxidized species meet their complement in solution and thus consume electrons without light generation. The ECL efficiency (# of photons generated / electron transferred) is estimated as 0.05 for $Ru(bpy)_3^{2+}$.[67] Meaning a mere 5% of electrons transferred generate a single photon, making ECL orders of magnitude less sensitive than fluorescence.

Array-based c-BPI was initially developed by our lab in 2012, by the name of "Fluorescence Enable Electrochemical Microscopy" (FEEM).[71] Our lab and others have previously used the technique to spatially map heterogeneous redox environments such as in the 3D mapping microelectrode diffusion layers,[72] measuring electrocatalytic activity,[71] and detecting cellular respiration of MCF-7 cell spheroids.[73]

Yet, the analytical goals of the technique had long been to extend its sensitivity to be the same (or better) than that of classical electrochemical measurements. Quantitation in

electrochemistry is limited by its shot noise,[74] whereas c-BPI could in theory measure single electron transfer via the detection of singly generated fluorophores. The first step in this process was to bridge the gap from long steady-state measurements, as previously described, toward the detection of rapid current transients as they appear in both nanoparticle collision events and biological systems. Given that the nanoparticle collision transient current signal is easily tunable with particle diameter and solution condition, it can be used as a model system to explore the LOD of c-BPI under various optical configurations.

The detection of quick nanoparticle collision events is indeed quite trivial when measured electrochemically, yet when extended to the c-BPI system it becomes a challenging task, given that the recording mechanisms are fundamentally different. The electrochemical recordings in Chapters 2 and 3 are sampled at 100 kHz, giving 10 μs temporal resolution. Current is reported as the rate of electron flow at any 10 μs time interval. Adjusting the sampling rate does not influence the measured current, but rather only influences the resolution at which it is output. However, the recording mechanism for optical channels is fundamentally different. Instead, the camera outputs the sum of the photons per exposure time between optical frames. Thus, changing the sampling rate directly influences the measured signal, whereby a faster frame rate (increased temporal resolution) produces inversely lower sensitivity (photons per image).

In Chapters 4 and 5 I further explore this imaging dichotomy with the use of nanoparticle collisions as a model system to explore the detection of transient optical events with c-BPI. Specifically, Chapter 4 demonstrates the successful detection of sub-second transient cathodic Pt NP collision events coupled to anodic ECL across a single bipolar microelectrode.[75] The work demonstrates the first time that current transients have been measured using the c-BPI approach. Chapter 5 utilizes Ag NP oxidation as a model system towards the detection of transient oxidative

events, similar in size to biological events of interest. Here, I investigate two different cathodic light generation mechanisms and their limitations as they are extended to the c-BPI system. Chapter 6 lastly describes the collaborative efforts pursued with Todd J. Anderson whereby we design electrochemical imaging experiments to showcase the power of his newly fabricated microelectrode arrays containing over 146,000 electrodes in a 1 cm^2 area.[76] Emphasis is given from the experimentalist's point of view to highlight features of array design that should be considered to create a usable product.

1.4 REFERENCES

(1) Selamet, O. F.; Becerikli, F.; Mat, Mahmut, D.; Kaplan, Y. Development and Testing of a Highly Efficient Proton Exchange Membrane (PEM) Electrolyzer Stack. *Int. J. Hydrogen Energy* **2011**, *36*, 11480–11487.

(2) Debe, M. K. Electrocatalyst Approaches and Challenges for Automotive Fuel Cells. *Nature* **2012**, *486* (7401), 43–51.

(3) Zhang, X. F.; Liu, Z. G.; Shen, W.; Gurunathan, S. Silver Nanoparticles: Synthesis, Characterization, Properties, Applications, and Therapeutic Approaches. *Int. J. Mol. Sci.* **2016**, *17*, 1534.

(4) Bai, C.; Liu, M. From Chemistry to Nanoscience: Not Just a Matter of Size. *Angew. Chemie - Int. Ed.* **2013**, *52*, 2678–2683.

(5) Solla-Gullon, J.; Vidal-Iglesias, F. J.; Lopez-Cudero, A.; Garnier, E.; Feliu, J. M.; Aldaz, A. Shape-Dependent Electrocatalysis: Methanol and Formic Acid Electrooxidation on Preferentially Oriented Pt Nanoparticles. *Phys. Chem. Chem. Phys.* **2008**, *10*, 3689–3698.

(6) Wang, S.; Kuai, L.; Huang, Y.; Yu, X.; Liu, Y.; Li, W.; Chen, L.; Geng, B. A Highly Efficient, Clean-Surface, Porous Platinum Electrocatalyst and the Inhibition Effect of Surfactants on Catalytic Activity. *Chem. Eur. J.* **2013**, *19*, 240–248.

(7) Tang, Y.; Cheng, W. Nanoparticle-Modified Electrode with Size- and Shape-Dependent Electrocatalytic Activities. *Langmuir* **2013**, *29*, 3125–3132.

(8) Kinoshita, K. Particle Size Effects for Oxygen Reduction on Highly Dispersed Platinum in Acid Electrolytes. *J. Electrochem. Soc.* **1990**, *137*, 845–848.

(9) Goines, S.; Dick, J. E. Review—Electrochemistry's Potential to Reach the Ultimate Sensitivity in Measurement Science. *J. Electrochem. Soc.* **2020**, *167* (3), 037505.

(10) Patrice, F. T.; Qiu, K.; Ying, Y.; Long, Y. Single Nanoparticle Electrochemistry. *Annu. Rev. Anal. Chem.* **2019**, *12*, 347–370.

(11) Defnet, P. A.; Anderson, T. J.; Zhang, B. Stochastic Collision Electrochemistry of Single Silver Nanoparticles. *Curr. Opin. Electrochem.* **2020**, *22*, 129–135.

(12) Kwon, S. J.; Zhou, H.; Fan, F. R. F.; Vorobyev, V.; Zhang, B.; Bard, A. J. Stochastic Electrochemistry with Electrocatalytic Nanoparticles at Inert Ultramicroelectrodes - Theory and Experiments. *Phys. Chem. Chem. Phys.* **2011**, *13*, 5394–5402.

(13) Xiao, X.; Bard, A. J. Observing Single Nanoparticle Collisions at an Ultramicroelectrode by Electrocatalytic Amplification. *J. Am. Chem. Soc.* **2007**, *129*, 9610–9612.

(14) Bonezzi, J.; Boika, A. Deciphering the Magnitude of Current Steps in Electrochemical Blocking Collision Experiments and Its Implications. *Electrochim. Acta* **2017**, *236*, 252–259.

(15) Deng, Z.; Renault, C. Detection of Individual Insulating Entities by Electrochemical Blocking. *Curr. Opin. Electrochem.* **2021**, *25*, 100619.

(16) Zhang, F.; Defnet, P. A.; Fan, Y.; Hao, R.; Zhang, B. Transient Electrocatalytic Water Oxidation in Single-Nanoparticle Collision. *J. Phys. Chem. C* **2018**, *122*, 6447–6455.

(17) Sundaresan, V.; Monaghan, J. W.; Willets, K. A. Visualizing the Effect of Partial Oxide Formation on Single Silver Nanoparticle Electrodissolution. *J. Phys. Chem. C* **2018**, *122*, 3138–3145.

(18) Castañeda, A. D.; Brenes, N. J.; Kondajji, A.; Crooks, R. M. Detection of MicroRNA by Electrocatalytic Amplification: A General Approach for Single-Particle Biosensing. *J. Am. Chem. Soc.* **2017**, *139* (22), 7657–7664.

(19) Yi, W.; Xu, C.; Xiong, T.; Gao, T.; Yu, P.; He, X.; Mao, L. Label-Free Analysis of Adsorbed Protein Heterogeneity on Individual Particles, Based on Single Particle Collision Events. *Electrochem. commun.* **2020**, *111*, 106666.

(20) Bartlett, T. R.; Sokolov, S. V; Compton, R. G. Electrochemical Nanoparticle Sizing Via Nano-Impacts: How Large a Nanoparticle Can Be Measured? *ChemistryOpen* **2015**, *4*, 600–605.

(21) Holt, L. R.; Plowman, B. J.; Young, N. P.; Tschulik, K.; Compton, R. G. The Electrochemical Characterization of Single Core–Shell Nanoparticles Angewandte. *Agnew. Chem. Int. Ed.* **2016**, *55*, 397–400.

(22) Percival, S. J.; Zhang, B. Fast-Scan Cyclic Voltammetry Allows Determination of Electron-Transfer Kinetic Constants in Single Nanoparticle Collision. *J. Phys. Chem. C* **2016**, *120*, 20536–20546.

(23) Huang, X.; Deng, H.; Liu, C.; Jiang, J.; Zeng, Q.; Wang, L. A Snapshot of the Properties of Single Nanoparticles at the Moment of a Collision. *Chem. - A Eur. J.* **2016**, *22*, 9523–9527.

(24) Xiao, X.; Fan, F. F.; Zhou, J.; Bard, A. J. Current Transients in Single Nanoparticle Collision Events. *J. Am. Chem. Soc.* **2008**, *130*, 16669–16677.

(25) Ortiz-Ledon, C. A.; Zoski, C. G. Pt Nanoparticle Collisions Detected by Electrocatalytic Amplification and Atomic Force Microscopy Imaging: Nanoparticle Collision Frequency, Adsorption, and Random Distribution at an Ultramicroelectrode Surface. *Anal. Chem.* **2017**, *89*, 6424–6431.

(26) Zhou, Y.; Rees, N. V; Compton, R. G. The Electrochemical Detection and Characterization of Silver Nanoparticles in Aqueous Solution. *Agnew. Chem. Int. Ed.* **2011**, *50*, 4219–4221.

(27) Batchelor-mcauley, C.; Ellison, J.; Tschulik, K.; Hurst, P. L.; Boldt, R.; Compton, R. G. In Situ Nanoparticle Sizing with Zeptomole Sensitivity. *Analyst* **2015**, *140*, 5048–5054.

(28) Ngamchuea, K.; Clark, R. O. D.; Sokolov, S. V; Young, N. P.; Batchelor-Mcauley, C.; Compton, R. G. Single Oxidative Collision Events of Silver Nanoparticles : Understanding the Rate-Determining Chemistry. *Chem. Eur. J.* **2017**, *23*, 16085–16096.

(29) Sokolov, S. V; Tschulik, K.; Batchelor-Mcauley, C.; Jurkschat, K.; Compton, R. G. Reversible or Not? Distinguishing Agglomeration and Aggregation at the Nanoscale. *Anal. Chem.* **2015**, *87*, 10033–10039.

(30) Toh, H. S.; Jurkschat, K.; Compton, R. G. The Influence of the Capping Agent on the Oxidation of Silver Nanoparticles: Nano-Impacts versus Stripping Voltammetry. *Chem. Eur. J.* **2015**, *21*, 2998–3004.

(31) Tanner, E. E. L.; Tschulik, K.; Tahany, R.; Jurkschat, K.; Batchelor-mcauley, C.; Compton, R. G. Nanoparticle Capping Agent Dynamics and Electron Transfer: Polymer-Gated Oxidation of Silver Nanoparticles. *J. Phys. Chem. C* **2015**, *119* (32), 18808–18815.

(32) Zhou, Y.; Haddou, B.; Rees, V.; Compton, R. G. The Charge Transfer Kinetics of the Oxidation of Silver and Nickel Nanoparticles via Particle – Electrode Impact Electrochemistry. **2012**, 14354–14357.

(33) Haddou, B.; Rees, N. V.; Compton, R. G. Nanoparticle–Electrode Impacts: The Oxidation of Copper Nanoparticles Has Slow Kinetics. *Phys. Chem. Chem. Phys.* **2012**, *14*, 13612–13617.

(34) Zhou, Y.; Rees, N. V; Pillay, J.; Tshikhudo, R.; Compton, R. G. Gold Nanoparticles Show Electroactivity: Counting and Sorting Nanoparticles upon Impact with Electrodes. *ChemComm* **2012**, *48*, 224–226.

(35) Suherman, A. L.; Zampardi, G.; Kuss, S.; Tanner, E. E. L.; Amin, H. M. A.; Young, N. P.; Compton, R. G. Understanding Gold Nanoparticle Dissolution in Cyanide-Containing Solution via Impact-Chemistry. *Phys. Chem. Chem. Phys.* **2018**, *20*, 28300–28307.

(36) Stuart, E. J. E.; Tschulik, K.; Batchelor-Mcauley, C.; Compton, R. G. Electrochemical Observation of Single Collision Events: Fullerene Nanoparticles. *ACS Nano* **2014**, *8*, 7648–7654.

(37) Zhou, X. F.; Cheng, W.; Compton, R. G. Nano-Impacts of Bifunctional Organic Nanoparticles. *Nanoscale* **2014**, *6*, 6873–6878.

(38) Rees, N. V; Zhou, Y.; Compton, R. G. The Aggregation of Silver Nanoparticles in Aqueous Solution Investigated via Anodic Particle Coulometry. *ChemPhysChem* **2011**, *12*, 1645–1647.

(39) Oja, S. M.; Robinson, D. A.; Vitti, N. J.; Edwards, M. A.; Liu, Y.; White, H. S.; Zhang, B. Observation of Multipeak Collision Behavior during the Electro- Oxidation of Single Ag Nanoparticles. *J. Am. Chem. Soc.* **2017**, *139*, 708–718.

(40) Ustarroz, J.; Kang, M.; Bullions, E.; Unwin, P. R. Impact and Oxidation of Single Silver Nanoparticles at Electrode Surfaces : One Shot versus Multiple Events. *Chem. Sci.* **2017**, *8*, 1841–1853.

(41) Ma, W.; Ma, H.; Chen, J. F.; Peng, Y. Y.; Yang, Z. Y.; Wang, H. F.; Ying, Y. L.; Tian, H.; Long, Y. T. Tracking Motion Trajectories of Individual Nanoparticles Using Time-Resolved Current Traces. *Chem. Sci.* **2017**, *8* (3), 1854–1861.

(42) Robinson, D. A.; Liu, Y.; Edwards, M. A.; Vitti, N. J.; Oja, S. M.; Zhang, B.; White, H. S. Collision Dynamics during the Electrooxidation of Individual Silver Nanoparticles. *J. Am. Chem. Soc.* **2017**, *139*, 16923–16931.

(43) Robinson, D. A.; Edwards, M. A.; Ren, H.; White, H. S. Effects of Instrumental Filters on Electrochemical Measurement of Single-Nanoparticle Collision Dynamics. *ChemElectroChem* **2018**, *5*, 1–10.

(44) Zhang, F.; Edwards, M. A.; Hao, R.; White, H. S.; Zhang, B. Collision and Oxidation of Silver Nanoparticles on a Gold Nanoband Electrode. *J. Phys. Chem. C* **2017**, *121*, 23564–23573.

(45) Mckelvey, K.; Robinson, D. A.; Vitti, N. J.; Edwards, M. A.; White, H. S. Single Ag Nanoparticle Collisions within a Dual-Electrode Micro-Gap Cell. *Faraday Discuss.* **2018**, *210*, 189–200.

(46) Patel, A. N.; Martinez-Marrades, A.; Brasiliense, V.; Koshelev, D.; Besbes, M.; Kuszelewicz, R.; Combellas, C.; Tessier, G.; Kanoufi, F. Deciphering the Elementary Steps of Transport-Reaction Processes at Individual Ag Nanoparticles by 3D Superlocalization Microscopy. *Nano Lett.* **2015**, *15*, 6454–6463.

(47) Hao, R.; Fan, Y.; Zhang, B. Imaging Dynamic Collision and Oxidation of Single Silver Nanoparticles at the Electrode/Solution Interface. *J. Am. Chem. Soc* **2017**, *139*, 12274–12282.

(48) Fang, Y.; Wang, W.; Wo, X.; Luo, Y.; Yin, S.; Wang, Y.; Shan, X.; Tao, N. Plasmonic Imaging of Electrochemical Oxidation of Single Nanoparticles. *J. Am. Chem. Soc.* **2014**, *136*, 12584–12587.

(49) Wonner, K.; Evers, M. V; Tschulik, K. Simultaneous Opto- and Spectro-Electrochemistry: Reactions of Individual Nanoparticles Uncovered by Dark-Field Microscopy. *J. Am. Chem. Soc.* **2018**, *140*, 12658–12661.

(50) Brasiliense, V.; Patel, A. N.; Martinez-marrades, A.; Shi, J.; Chen, Y.; Combellas, C.; Tessier, G.; Kanoufi, F. Correlated Electrochemical and Optical Detection Reveals the Chemical Reactivity of Individual Silver Nanoparticles. *J. Am. Chem. Soc.* **2016**, *138*, 3478–3483.

(51) Wei, W.; Yuan, T.; Jiang, W.; Gao, J.; Chen, H. Y.; Wang, W. Accessing the Electrochemical Activity of Single Nanoparticles by Eliminating the Heterogeneous Electrical Contacts. *J. Am. Chem. Soc.* **2020**, *142*, 14307–14313.

(52) Jiang, W.; Wei, W.; Yuan, T.; Liu, S.; Niu, B.; Wang, H.; Wang, W. Tracking the Optical Mass Centroid of Single Electroactive Nanoparticles Reveals the Electrochemically Inactive Zone. *Chem. Sci.* **2021**, *12*, 8556–8562.

(53) Sun, L.; Wang, W.; Chen, H. Dynamic Nanoparticle-Substrate Contacts Regulate Multi-Peak Behavior of Single Silver Nanoparticle Collisions. *ChemElectroChem* **2018**, *5*, 2995–2999.

(54) Sundaresan, V.; Monaghan, J. W.; Willets, K. A. Monitoring Simultaneous Electrochemical Reactions with Single Particle Imaging. *ChemElectroChem* **2018**, *5*, 3052–3058.

(55) Robinson, D. A.; White, H. S. Electrochemical Synthesis of Individual Core@Shell and Hollow Ag/Ag2S Nanoparticles. *Nano Lett.* **2019**, *19*, 5612–5619.

(56) Zelinsky, A. G. RDE Study of Thiosulfate Oxidation on Gold. *J. Electroanal. Chem.* **2014**, *735*, 111–114.

(57) Robinson, D. A.; Kondajji, A. M.; Castañeda, A. D.; Dasari, R.; Crooks, R. M.; Stevenson, K. J. Addressing Colloidal Stability for Unambiguous Electroanalysis of Single Nanoparticle Impacts. *J. Phys. Chem. Lett.* **2016**, *7*, 2512–2517.

(58) Robinson, D. A.; Duay, J.; Kondajji, A. M.; Stevenson, K. J. Mechanistic Aspects of Hydrazine-Induced Pt Colloid Instability and Monitoring Aggregation Kinetics with Nanoparticle Impact Electroanalysis. *Faraday Discuss.* **2016**, *193*, 293–312.

(59) Xiang, Z. P.; Deng, H. Q.; Peljo, P.; Fu, Z. Y.; Wang, S. L.; Mandler, D.; Sun, G. Q.; Liang, Z. X. Electrochemical Dynamics of a Single Platinum Nanoparticle Collision Event for the Hydrogen Evolution Reaction. *Angew. Chemie - Int. Ed.* **2018**, *57*, 3464–3468.

(60) Spry, D. B.; Fayer, M. D. Proton Transfer and Proton Concentrations in Protonated Nafion Fuel Cell Membranes. *J. Phys. Chem. B.* **2009**, *113*, 10210–10221.

(61) Defnet, P. A.; Han, C.; Zhang, B. Temporally-Resolved Ultrafast Hydrogen Adsorption and Evolution on Single Platinum Nanoparticles. *Anal. Chem.* **2019**, *91*, 4023–4030.

(62) Cox, J. T.; Guerrette, J. P.; Zhang, B. Steady-State Voltammetry of a Microelectrode in a Closed Bipolar Cell. *Anal. Chem.* **2012**, *84*, 8797–8804.

(63) Guerrette, J. P.; Oja, S. M.; Zhang, B. Coupled Electrochemical Reactions at Bipolar Microelectrodes and Nanoelectrodes. *Anal. Chem.* **2012**, *84*, 1609–1616.

(64) Oja, S. M.; Guerrette, J. P.; David, M. R.; Zhang, B. Fluorescence-Enabled Electrochemical Microscopy with Dihydroresorufin as a Fluorogenic Indicator. *Anal. Chem.* **2014**, *86* (12), 6040–6048.

(65) Lakowicz, J. R. Single-Molecule Detection. In *Principles of Fluorescence Spectroscopy*; 2006; pp 757–795.

(66) Qin, X.; Li, Z. Q.; Zhou, Y.; Pan, J. Bin; Li, J.; Wang, K.; Xu, J. J.; Xia, X. H. Fabrication of High-Density and Superuniform Gold Nanoelectrode Arrays for Electrochemical Fluorescence Imaging. *Anal. Chem.* **2020**, *92*, 13493–13499.

(67) Richter, M. M. Electrochemiluminescence (ECL). *Chem. Rev.* **2004**, *104* (3), 3003–3006.

(68) Yuan, Y.; Han, S.; Hu, L.; Parveen, S.; Xu, G. Coreactants of Tris(2,2′-Bipyridyl)Ruthenium(II) Electrogenerated Chemiluminescence. *Electrochim. Acta* **2012**, *82*, 484–492.

(69) Liu, X.; Shi, L.; Niu, W.; Li, H.; Xu, G. Environmentally Friendly and Highly Sensitive Ruthenium(II) Tris(2,2′-Bipyridyl) Electrochemiluminescent System Using 2-(Dibutylamino)Ethanol as Co-Reactant. *Angew. Chemie - Int. Ed.* **2007**, *46* (3), 421–424.

(70) Xue, L.; Guo, L.; Qiu, B.; Lin, Z.; Chen, G. Mechanism for Inhibition of $Ru(Bpy)_3^{2+}$/DBAE Electrochemiluminescence System by Dopamine. *Electrochem. commun.* **2009**, *11* (8), 1579–1582.

(71) Guerrette, J. P.; Percival, S. J.; Zhang, B. Fluorescence Coupling for Direct Imaging of Electrocatalytic Heterogeneity. *J. Am. Chem. Soc.* **2013**, *135*, 855–861.

(72) Oja, S. M.; Zhang, B. Imaging Transient Formation of Diffusion Layers with Fluorescence-Enabled Electrochemical Microscopy. *Anal. Chem.* **2014**, *86*, 12299–12307.

(73) Iwama, T.; Inoue, K. Y.; Abe, H.; Matsue, T.; Shiku, H. Bioimaging Using Bipolar Electrochemical Microscopy with Improved Spatial Resolution. *Analyst* **2020**, *145*, 6895–6900.

(74) Gao, R.; Edwards, M. A.; Harris, J. M.; White, H. S. Shot Noise Sets the Limit of Quantification in Electrochemical Measurements. *Curr. Opin. Electrochem.* **2020**, *22*, 170–177.

(75) Defnet, P. A.; Zhang, B. Detection of Transient Nanoparticle Collision Events Using Electrochemiluminescence on a Closed Bipolar Microelectrode. *ChemElectroChem* **2020**, *7*, 252–259.

(76) Anderson, T. J.; Defnet, P. A.; Zhang, B. Electrochemiluminescence (ECL)-Based Electrochemical Imaging Using a Massive Array of Bipolar Ultramicroelectrodes. *Anal. Chem.* **2020**, *92*, 6748–6755.

Chapter 2. TEMPORALLY-RESOLVED ULTRAFAST HYDROGEN ADSORPTION AND EVOLUTION ON SINGLE PLATINUM NANOPARTICLES*

2.1 INTRODUCTION

Metal nanoparticles (NPs) have been intensively studied over the past decades due to their unique electrocatalytic properties.[1,2] Platinum NPs, in particular, have superior catalytic activity over many other materials for the hydrogen evolution reaction (HER),[3] supporting their use in electrolyzers for hydrogen generation as a clean energy source.[4] Previous research has shown that the electrocatalytic activity of single NPs can deviate from their ensemble activity due to structural influences, including size,[5] shape,[6,7] porosity,[8,9] and abundance of edge versus planar surfaces.[10] While many attempts have been made to synthesize monodispersed NPs,[11,12,13] it can be challenging to yield accurate structure-function information using NP ensembles due to minute structural differences. Alternatively, many groups have studied electrocatalytic behavior of single NPs using probe-based methods and NP collision electrochemistry. Probe-based methods such as scanning electrochemical microscopy (SECM),[14,15] scanning ion-conductance microscopy (SICM),[16,17] and scanning electrochemical cell microscopy (SECCM),[18,19] have limited temporal resolution due to the need to precisely position and scan the probe and require the use surface-immobilized NPs. Instead, methods based on single NP collisions have emerged as high-throughput techniques to characterize electrocatalytic activity of freely diffusing NPs.

The method of electrocatalytic amplification (EA), first reported by Xiao and Bard,[20] has been used to probe single NPs for various redox reactions including proton reduction,[21,22,23] oxygen

---

* This chapter is adapted with permission from:
Defnet, P. A.; Han, C.; Zhang, B. Temporally-Resolved Ultrafast Hydrogen Adsorption and Evolution on Single Platinum Nanoparticles. *Anal. Chem.* **2019**, *91*, 4023–4030. Copyright (2019) American Chemical Society.

reduction,[24] hydrazine oxidation,[25,26,27] and others.[28,29,30] Traditionally a simple diffusion-based apparatus is used in which NPs are injected and allowed to diffuse freely in bulk redox solution. Upon collision with an inert ultramicroelectrode (UME), they catalyze the redox reaction, resulting in an enhanced current signal. The catalytic signal may be related to the holding potential, size, and catalytic activity of the NP, the redox concentration, and its diffusivity. Traditional EA method is often limited to the use of low concentrations of both redox species (e.g., a few mM) and supporting electrolyte due to NP instability when exposed to high ionic strength solutions.[26] The presence of aggregated NPs may cause uncertainty and complexity in data interpretation. It has been suggested that citrate-capped Pt NPs are only stable in acids below 1 mM[21] and in electrolyte solutions of mild salt concentrations.[26]

In this work we use a method called the "microjet collision system" to study the HER process across single Pt NP collisions in acid concentrations as high as 3 M ($[H^+]$∼750 mM on the electrode, vide infra) without observing significant NP aggregation. The system uses a pressure-driven flow to deliver Pt NPs from a glass micropipette onto a detecting carbon-fiber microelectrode (CFE) placed ∼10 μm away. NPs are exposed to the aggregate-inducing acid environment for < 1 ms, compared with seconds to minutes spent in previous diffusion-based system. The limited solution exposure permits continuous recording of thousands of collision events in concentrated acids.

Our microjet setup is derived from Macpherson's microjet electrode originally developed in 1994.[31] Macpherson,[32,33] Unwin,[34] and Compton[35] had developed the use of the microjet electrode for studying fast electron-transfer rate constants. Application of a similar wall-jet system was used to study Pt NP collisions and hydrazine oxidation in 2016 by Jiang et al.[36] Their study focused on the effect of convection on collision dynamics and did not explore the use of the pipet

to circumvent NP aggregation. They also used hydrazine solution conditions commonly reported in the literature for NP collisions.[27,37]

Here, we used the microjet collision system to generate rapid, consistent, and repeatable single-particle collision results in $HClO_4$ with effective $[H^+]$ from 1 to 750 mM on the electrode, which is 2 orders of magnitude more concentrated than previously reported.[21] With this system, we have resolved the ultrafast hydrogen adsorption process from hydrogen evolution in HER across individual Pt NPs. We measure a fast (~50 μs) spike, followed by a slow, seconds long decay in an apparent separation of the two processes, enabled by their disparate kinetic rates.

Previous reports have demonstrated the resolution of hydrogen adsorption and evolution reactions with potential scanning on Pt electrodes,[38,39,40] and with a unique carbon-supported electrodeposited Pt nanocrystal system reported by Kucernak et al.[41] One drawback of Kucernak's system, however, is the need to use larger particles, e.g., >72 nm, due to an insufficient current/noise ratio on smaller particles. Moreover, it requires a time-intensive fabrication process to study a single particle.

In our present work, we use the measured hydrogen adsorption charge to calculate the electroactive surface area (EASA) and roughness factor of single colliding Pt NPs. We also derive the kinetic parameters k^0 , K^0 , and α from our hydrogen evolution steady state currents. Overall, we demonstrate a clear advantage for single NP characterization with the use of concentrated redox solutions and the NP collision technique.

2.2 Experimental Section

2.2.1 *Chemicals and Materials*

The following chemicals were used as received from the manufacturers. Perchloric acid ($HClO_4$, Sigma-Aldrich, 70%), sodium perchlorate monohydrate ($NaClO_4 \cdot H_2O$, Fluka, >99.0%), ferrocenemethanol (FcMeOH, Sigma-Aldrich, 97%), potassium chloride (KCl, Fluka, >99%), potassium ferricyanide ($K_3Fe(CN)_6$, Mallinckrodt, >99%), sodium citrate dihydrate (Baker, >99.0%), citrate-capped Pt NPs with diameters 30 ± 3 and 50 ± 4 nm dispersed in 2 mM sodium citrate (NanoComposix), and citrate-capped Pt NPs with diameter 70 ± 4 nm dispersed in 4 mM sodium citrate (NanoComposix). All solutions were prepared with 18.2 $M\Omega \cdot cm^{-1}$ deionized water from a Barnstead NANOpure water purification system (ThermoScientific). Perchloric acid solutions ranged from 5 mM to 3 M with constant 20 mM $NaClO_4$ electrolyte. (*Caution: concentrated perchloric acid solutions are highly corrosive and should be handled with care.)*

2.2.2 *Fabrication and Characterization of Microelectrodes and Micropipettes*

CFEs were prepared by modifying the procedure of two previously reported methods.[42,43] A 5 µm diameter carbon fiber (Besfight G40-800) was aspirated into a glass capillary (1.2 mm O.D./0.69 mm I.D., Sutter) and pulled into two separate tips on a Sutter P-97 puller. Silver epoxy (Dupont) was used to connect a tungsten wire to the fiber inside the pipet. Epoxy was used to hold the tungsten wire in place. Excess carbon fiber protruding from the electrode tip was cut until flush with the pulled glass tip, dipped in epoxy (Epo-Tek 301) for 10 min and then allowed to set at 80 and 150 °C each for 2 h. Electrodes were beveled to a 45° angle using a home-built microelectrode beveler. CFEs were characterized using cyclic voltammetry from -400 to +700 mV versus

Ag/AgCl in 1 mM FcMeOH and 100 mM KCl. Only electrodes with stable i-V curves were used. A fresh surface was exposed by beveling the CFEs before and after each collision experiment.

Glass micropipettes of ~3 μm diameter orifice were prepared by pulling borosilicate glass capillary tubes (1 mm O.D./0.5 mm I.D., with filament; Sutter, BF100-50-10) on a P-97 puller. The following two-line program was used: heat = ramp value, pull = 0, velocity = 30, time = 250; heat = ramp + 10, pull = 70, velocity = 30, time = 250. A scalpel was used to trim pulled pipet to the desired size.

2.2.3 *Nanoparticle Characterization*

Transmission electron microscopy (TEM) imaging was performed on a FEI Technai G2 F20 TEM operating at 200 kV with a single tilt sample holder. The 30, 50, and 70 nm Pt NPs were drop-casted onto carbon-coated Formvar copper TEM grids (Ted Pella, Inc.) for TEM imaging. TEM images were used to characterize the size distribution of the NPs.

2.2.4 *Microjet Collision System Setup and Signal Processing*

A Petri dish containing the bulk acid solution with concentrations ranging from 5 mM to 3 M $HClO_4$ and 20 mM $NaClO_4$ was placed on an Olympus IX71 inverted microscope stage. A micropipette was filled with Pt NPs, connected to a Femtojet microinjector (Eppendorf), and attached to a micropositioner so that the orifice was dipped in the acid and positioned at a 45° angle. Stock NP solutions containing concentrations of 300, 55, and 20 pM for the 30, 50, and 70 nm NPs, respectively, were used unless otherwise stated. The CFE was connected to a separate micropositioner directly opposite from the micropipette's position. The position of the micropipette and the electrode were adjusted until both were in focus using a 20x (0.4 NA Olympus

LCPlanFl) objective and were approximately 10 μm apart facing each other. See Figure 2.1A for reference.

A constant pressure of 1 PSI was applied with a constant 10 μm pipet-electrode distance, unless otherwise stated. Due to the displacement of acid from the ejected NP and citrate solution, the effective acid concentration on the electrode surface was ~25% of the bulk concentration under these pressure and distance conditions. See Figure 2.10 for more details. All acid concentrations mentioned hereafter are effective surface concentrations on the electrode.

Peaks containing a singular spike and possible slow decay were accepted. Some peaks were broadened and of lower amplitude due to repeated NP collisions prior to sticking. These multipeak collision events were about 10% depending on particle size. Because we focus on hydrogen adsorption and evolution on fully adsorbed Pt NPs, these events were not considered for analysis in this work. Additionally, less than 5% of the peaks were distinctly larger than the rest, indicative of particle aggregation, and were also not used for analysis. Despite the small remaining overlap between the hydrogen adsorption spike and the hydrogen evolution steady state displayed in Figure 2.2A, the adsorption spikes were integrated back to the baseline to quantify their full charge.

All data reported in Appendix 2.1 are represented as the average ± one standard deviation. The error bars on the plots also represent the average ± one standard deviation. The method for extracting kinetic parameters are explicitly outlined in Appendix 2.2 and follows procedures recently published by Luo et al.[44]

2.2.5 *Electrochemical Measurements*

The CFE was held at a constant potential ranging from -200 to -800 mV versus Ag/AgCl. Its current was recorded with an Axopatch 200B amplifier (Axon Instruments). The current signal was sampled at 100 kHz using a 1322A digitizer (Axon Instruments) and filtered at 10 kHz with

an internal low-pass Bessel filter. Amperometric data were recorded using Axoscope 10.0 software (Molecule Devices) and analyzed with Clampfit 10.4 (Molecular Devices). All electrochemical experiments were performed in a home-built, grounded faraday cage. An Ag/AgCl quasi-reference electrode was used for all experiments reported herein.

2.3 Results and Discussion

2.3.1 *NP Recording with the Microjet Collision System*

We used the microjet collision system to measure single NP collision under low pH, high ionic strength conditions. As shown in Figure 2.1A, Pt NPs are housed in a micropipette, dispensed under pressure-driven flow through the bulk solution and land on a CFE probe positioned 10 µm away. With a pressure of 1 psi, the estimated time it takes for the NP to travel across the pipet-electrode gap is 0.8 ms (see Appendix 2.3 for more details). This contrasts with the traditional NP collision setups, where NPs freely diffuse in solution for tens to hundreds of seconds before colliding on the electrode. The minimal exposure to aggregate-inducing solution conditions is the key to the collection of thousands of single NP collisions in highly concentrated redox solutions. Moreover, it helps to preserve the freshness of the NP surfaces by greatly reducing possible contamination prior to collision on the electrode. As Scherson and Tolmachev have described, the surface of a nanometer-scale electrode or particle can be quickly contaminated when exposed to even trace amounts of organic impurities.[45] Jerkiewicz et al. has also reported that trace halides may foul Pt surfaces[46] and mitigate HER kinetic rates.[47]

Figure 2.1B shows an example of a *i-t* trace recorded at -400 mV on a 5 µm CFE in 25 mM $HClO_4$ using the microjet system. Each peak corresponds to a single 30 nm Pt NP landing on the electrode and catalyzing the reduction of protons ($H^+ + e^- = H_{ads}$, vide infra). Hundreds of collision

events were collected within tens of seconds and contain consistent peak shape, suggesting that these events are free of NP aggregation. The average collision frequency seen in Figure 2.1B is about 10 Hz. As a comparison, Figure 2.1C shows an *i-t* trace collected also at -400 mV in the classical diffusion-driven collision apparatus in 25 mM $HClO_4$. Since the acid concentration is well above the 1 mM aggregation limit, suggested by Liang and co-workers,[21] symptoms of particle aggregation are seen, including a decay in collision frequency and an increase in peak amplitude over time. Variable peak size is even observed within the first 20 s after NP injection. This comparison highlights the advantage of the microjet system for obtaining more reliable NP collision data in concentrated redox solutions.

Further experiments describing the method validation of the microjet experiment can be found in Figures 2.7-2.10, demonstrating that each peak is due to a single collision, that the NPs stick to the electrode independent of applied pressure, and an analysis of the effective H^+ concentration on the electrode surface while considering solution displacement due to the ejected NP solution from the microjet. Due to the low electrocatalytic activity of carbon, the proton reduction current on the recording carbon electrode is quite minimal. As such, NP collision is primarily driven by a pressure-driven flow from the glass pipet and by diffusion.

2.3.2 *Separation of Hydrogen Adsorption and Evolution on Single Pt NPs*

We used the microjet system to study the HER on single colliding Pt NPs under various concentrations, potentials, and NP sizes. Interestingly, we observed a new peak shape consisting of a fast (< 100 μs) current spike followed by a slow (seconds long) decay. We sought to determine the physical mechanism of the fast spike and slow decay processes.

We first studied the peak shape under potential-dependent conditions. As shown in Figure 2.2A, a fast spike that decays immediately back to baseline is generated from potentials ranging

from 0 to -400 mV. At further reducing potentials ranging from -500 to -800 mV, however, the same fast spike is observed, except instead of immediately returning to baseline, it is followed by an increasingly severe slow decay process.

We further studied the effect of H^+ concentration ranging from approximately 1 to 750 mM over the -400 and -700 mV potential values. In Figure 2.3A, we observe that the -400 mV fast spike becomes increasingly faster and taller as the proton concentration increases. In Figure 2.3B we also observe that the -700 mV fast spike becomes progressively faster and taller as the proton concentration increases, in a nearly identical way. We further note that the slow decay process becomes increasingly severe as the concentration increases.

We believe that the known mechanism of the HER on Pt surfaces explains the occurrence of this unique fast spike and slow decay peak shape. Illustrated in Figure 2.4A, reduction of protons proceeds through the following three steps on Pt:[48]

Volmer Step:

$$H^+ + e^- = H_{ads} \quad (1)$$

Heyrovsky Step:

$$H^+ + H_{ads} + e^- = H_2\ (g) \quad (2)$$

Tafel Step:

$$H_{ads} + H_{ads} = H_2\ (g) \quad (3)$$

where H^+ denotes protons in the bulk, H_{ads} is surface-adsorbed H atoms, and $H_2\ (g)$ is the H_2 molecules evolved from the Pt surface. Upon initial collision, protons are quickly reduced onto the NP surface forming a monolayer of H_{ads}. If the applied potential is further increased in the negative direction, hydrogen evolution may occur through two possible processes, where either one H_{ads} combines with one H^+ and an electron to form H_2 (the Heyrovsky step) or two H_{ads} combine to

form H_2 (the Tafel step). It is known that the hydrogen adsorption step is very rapid, whereas hydrogen evolution is the rate-determining step across Pt surfaces.[49]

We believe that the fast current spike is due to the initial hydrogen adsorption process (the Volmer step, $H^+ + e^- = H_{ads}$), while the slow decay is due to the hydrogen evolution process. At potentials ranging from 0 to -400 mV there is insufficient overpotential to drive the evolution reaction, and therefore the hydrogen adsorption will proceed until the entire Pt surface is covered by a monolayer of H_{ads} (Figure 2.4B). The fact that the current spike returns to the baseline also suggests that it is likely due to a self-limiting process, which supports this hypothesis. When the potential is moved to the -500 to -800 mV range, the initial hydrogen adsorption and subsequent evolution processes both occur and are temporally resolved from each other (Figure 2.4C). We note that we will evaluate the possible overlapping electrochemical processes later in the manuscript in our discussion of electroactive surface area determination.

While the fast hydrogen adsorption spike is distinguishable from the slow current decay, some overlap remains evident, as can be seen in Figure 2.2A. However, we found that the charge generated by the hydrogen evolution process during the fast (<100 μs) adsorption spike is minimal across increasingly negative potentials (Figure 2.2B), as evidenced by the charge limit approached at -600 mV for 30 nm NPs. This result demonstrates sufficient resolution of the two overlapping processes and suggests that complete monolayer surface coverage is obtained at around -600 mV. Previous literature supports this idea where a full hydrogen adsorption monolayer coverage is not reached until the overlapping hydrogen evolution process is also occurring.[38] Similar results were obtained for 50 and 70 nm Pt NPs, as shown in Figure 2.11B. Figures 2.2C, 2.11C, and 2.11D demonstrate that the duration of the hydrogen adsorption event for 30, 50, and 70 nm NPs, respectively, becomes progressively faster with increasing potential.

We also determined the effect of acid concentration on the charge and duration of the hydrogen adsorption spikes at -700 mV. We found that the adsorption charge reaches a maximum value at 12.5 mM proton concentration (Figure 2.3C), suggesting that the particle reaches its maximum hydrogen monolayer coverage at and above this value. At lower acid concentrations, the rate of proton adsorption is not fast enough to reach maximal surface coverage prior to hydrogen evolution. Interestingly, the duration of these adsorption events reaches a minimum 40 μs also at 12.5 mM concentration and above, as shown in Figure 2.3D. The 40 μs value approaches the 33 μs theoretical limit of the fastest event measurable using a 10 kHz low-pass instrumental filter,[50] as was used in this work. This suggests that the true hydrogen adsorption process may be even faster than measured.

The separation of the two mechanistic steps of the HER across Pt NPs is likely due to use of the 10 kHz low pass instrumental filter. We explicitly explore the effect of applied filter frequency in Figure 2.12 and can mimic previously reported results, absent of the <100 μs hydrogen adsorption spike, by applying a lower filter frequency of 1 kHz. This finding is consistent with recent NP collision studies, where the use of higher bandwidth recording allows the temporal resolution of multipeak collisions on silver NPs.[51,52,53]

We last examined the charge transfer properties of single Pt NPs catalyzing the HER as a means to demonstrate that the kinetic parameters k^0 , K^0 , and α can be derived for citrate-capped Pt NPs using our NP collision methodology. To this end, we followed a procedure recently published by Chen and Luo.[44] As thoroughly described in Appendix 2.2, we plotted the HER current at various potentials (Figure 2.5A), fit a nonlinear regression using Equations 7-9, and extracted kinetic parameters from the fitting protocol. The HER current was best fitted using the Heyrovsky model suggesting that it is the rate-limiting step in the entire HER process. We also

note that platinum (100) and (111) surfaces follow a Heyrovsky rate-limiting step mechanism for the HER.[54] The standard rate constant (k^0) and the charge-transfer coefficient (α) of the Heyrovsky step, and the equilibrium constant for the Volmer step (K^0) were extracted with values of $k^0 = 2.58 \times 10^{-3} \pm 1.2 \times 10^{-2}$ m/s, $K^0 = 5.56 \times 10^{-3} \pm 3.7 \times 10^{-8}$ mM^{-1} , $\alpha = 0.77 \pm 0.15$. The k^0 and α values are consistent with value reported for Pt nanoelectrodes, whereas the K^0 value is approximately 2 orders of magnitude greater.[44] Despite this difference, we also found that the value of K^0 does not significantly impact that fitting curve when it is greater than 5.0×10^{-5} mM^{-1} , since the a_{H+} term at 25 mol/m^3 dominates its contribution. In fact, the determined value of K^0 only becomes relevant at approximately µM concentrations of H^+. This suggests that the rate of hydrogen adsorption on the Pt NPs is sufficiently fast to negligibly impact the hydrogen evolution current in the studied mM acid concentrations.

2.3.3 *Calculating the Electroactive Surface Area of Single Pt NPs*

Our ability to resolve the hydrogen adsorption process enables us to calculate the electroactive surface area (EASA) and roughness factor (R_f) across single Pt NPs. This calculation is nearly identical to the extensively studied hydrogen-underpotential deposition (H-UPD) for EASA determination of Pt electrodes.[55] If we assume that one hydrogen atom is adsorbed across each surface Pt atom, then the measured hydrogen adsorption charge (Q_m) can be converted to EASA using the known charge density of hydrogen across a single monolayer of polycrystalline Pt (210 µC/cm^2 ; C_{mL}).[56] We acknowledge that the value of 210 µC/cm^2 does not consider the possibility of the citrate capping ligand blocking some of the active Pt surface sites on the NP. We would expect a smaller charge density of adsorbed hydrogen if this blocking effect had been considered, although to the best of our knowledge, a more appropriate charge density considering ligand effects has not been reported in literature. Therefore, the electroactive surface areas derived

in this manuscript may represent an overestimation from their true value due to the use of 210 μC/cm^2 for C_{ML}. As shown in Equation 4, the surface coverage (θ_H) must also be considered, where it has been estimated that approximately 92% of surface Pt sites are accessible to hydrogen adsorption.[55] Table A.2.2 shows the calculated EASA values from the measured hydrogen adsorption charge limits identified in Figures 2.2B and 2.11B across 30, 50, and 70 nm Pt NPs.

$$EASA = \frac{Q_m}{\theta_H C_{ML}} \tag{4}$$

We further calculated the electrochemical roughness factor (R_f) across single citrate-capped Pt NPs. The R_f value quantifies the surface roughness of an electrode as it deviates from its predicted atomically smooth geometry. Reports of R_f values range from 2 to 3 for well-polished Pt electrodes[40] and can be 200-500 for nanostructured, electrodeposited Pt structures,[57] both characterized using bulk H-UPD methods. The R_f value was calculated using Equation 5, where the measured charge (Q_m) was divided by the predicted hydrogen adsorption charge assuming a perfectly spherical geometry (Q_g) with diameters of 30, 50, and 70 nm. The R_f values are given in Table A.2.2 and range from approximately 10 to 17. These values are reasonable given that the Pt NPs have mesoporous structure and are visibly rough in their TEM images (Figure 2.6). Again, since our Pt NPs were citrate capped, we might expect the Q_m and R_f values to be underestimated due to the possibility of citrate ligands blocking some of the electroactive surface sites on platinum.

$$R_f = \frac{Q_m}{Q_g} \tag{5}$$

We determined the experimental error of the calculated EASA and R_f values by considering charge contributions of overlapping electrochemical processes including capacitive charging, and the oxygen reduction reaction (ORR). The capacitive charging contribution was calculated by assuming a 20 μF/cm^2 double layer capacitance for a smooth, spherical 30 nm NP undergoing a 0.5 V change upon collision.[58,59] This contributes 0.28 fC, accounting for 0.4% of the total 61.4 fC measured charge. The ORR contribution was calculated by assuming a constant 250 μM dissolved oxygen concentration,[60] and steady-state diffusion-limited conditions for dissolved O_2 approaching a spherical particle on a planar surface.[61] The ORR contributes 2.5 fC over a 100 μs period, accounting for 4.1% of the overall measured charge. Using the same method, we also calculated the effect of the ORR on the HER steady state current to contribute to the expected error for Figure 2.5A. We found that this accounts for 12.4 pA of current at the ORR steady state of ~-0.6 V,[62] contributing to a less than 3% error. We further acknowledge that effect of hydrogen spillover may be present, since it has been reported to occur for Pt supported on carbon.[56,63,64] Although we do not have a method to quantify its charge contribution, we expect its effect to be minimal relative to the total charge measured.

2.4 Conclusion

In summary, we have developed the microjet collision system to study single NP electrochemistry in highly concentrated electrolyte conditions without observing significant particle aggregation. Here we chose to study the hydrogen evolution reaction in acid concentrations ranging from 1 to 750 mM. We find that with the application of a high filtering frequency, we can record a new peak shape consisting of a fast (~50 μs) spike followed by a slow (seconds long) decay, to which we identify as the temporal separation of hydrogen adsorption and

evolution processes on a single colliding NP. We demonstrate that these electrochemical processes are distinguished from each other, which enables the calculation of electroactive surface area and roughness factor across individually colliding NPs. The use of high acid concentrations is critical toward obtaining a full adsorbed monolayer of adsorbed hydrogen before overlapping with the evolution process, enabling a more precise measure of NP size. This report represents an important advancement in the study of single NP electrocatalysts and toward the broadly applicable ability to study single NP properties in highly concentrated redox solutions using the NP collision method.

2.5 FIGURES

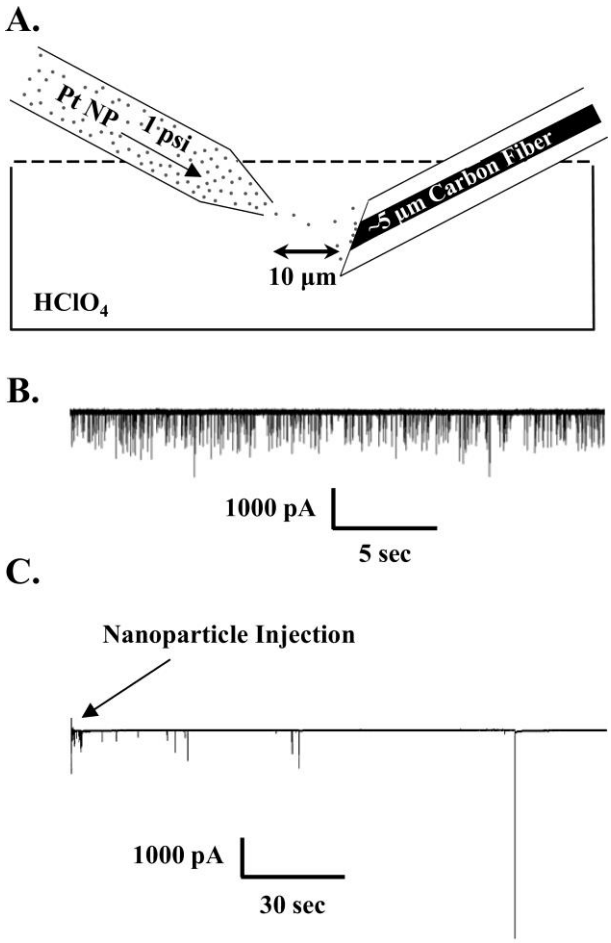

Figure 2.1. Microjet and Diffusion-Limited Collision Examples.

(A) Schematic of microjet collision setup. Pt NPs are dispensed under 1 PSI pressure through a bulk acid solution ranging from 5 mM to 3 M acid concentration and onto a 5 µm carbon fiber electrode surface. Note that due to displacement of the acid from dispensed NP solution, the effective acid concentration on the electrode surface ranges from 1.25 to 750 mM. (B) *i-t* trace of NP collisions recorded with the microjet system at -400 mV, 25 mM $HClO_4$ effective concentration on the electrode surface, and 30 nm Pt NPs. (C) *i-t* trace of NP collisions recorded in a traditional diffusion-limited apparatus at -400 mV and in 25 mM $HClO_4$ with 30 nm Pt NPs.

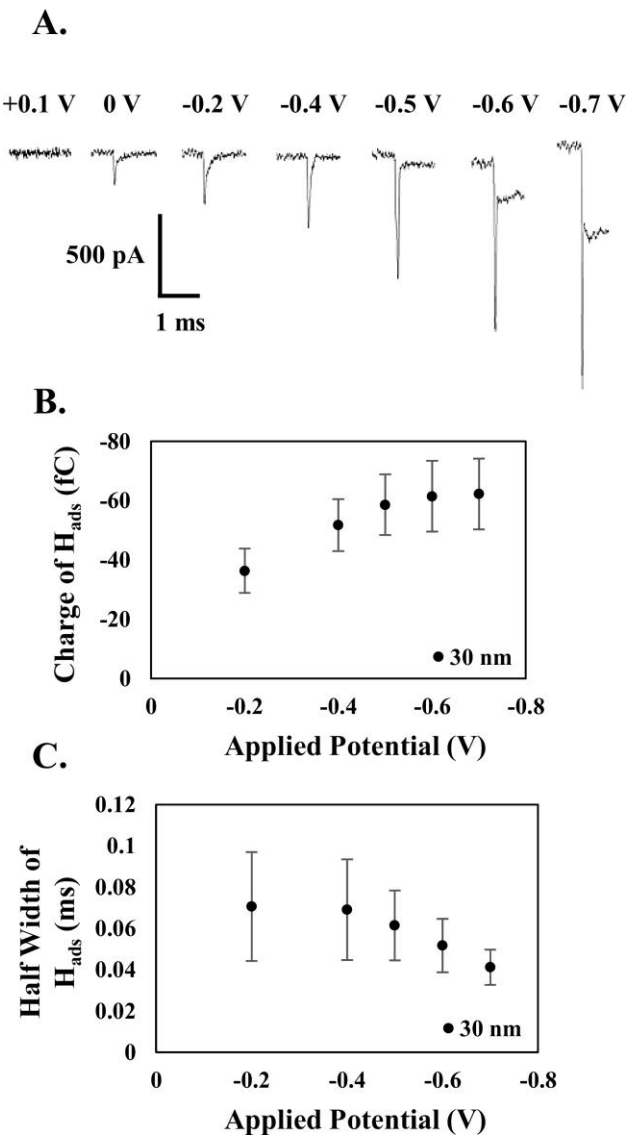

Figure 2.2. Potential-Dependent Microjet Collision Analysis.

(A) Comparison of microjet collision peak-shapes at various potentials. Peaks were recorded in 25 mM $HClO_4$, with 30 nm Pt NPs. (B) Integration of the fast H_{ads} spike at various applied potentials for 30 nm Pt NPs. (C) The half width of the fast H_{ads} spike at various potentials for 30 nm Pt NPs. The 'n' values for (B) and (C) are both equal to 35.

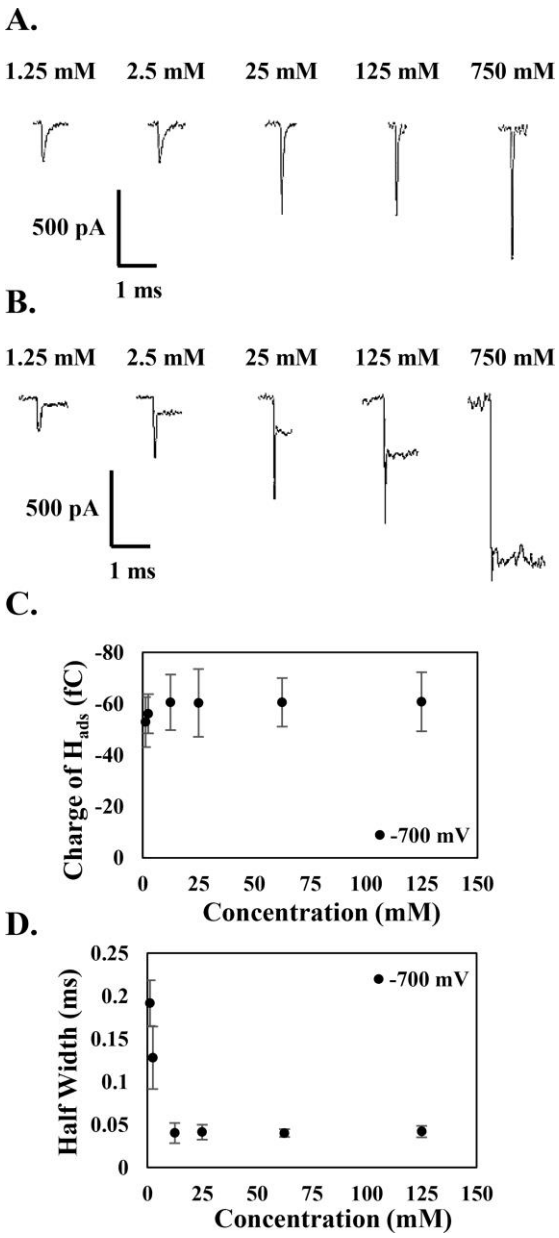

Figure 2.3. Concentration-Dependent Microjet Collision Analysis.

A comparison of collision events at various concentrations at (A) -400 mV and (B) -700 mV. (C) Integration of the hydrogen adsorption spike at various $HClO_4$ concentrations collected at -700 mV for 30 nm Pt NPs. (D) The half width of the fast H_{ads} spike at various concentrations collected at -700 mV for 30 nm Pt NPs. The 'n' values for (C) and (D) are both equal to 35.

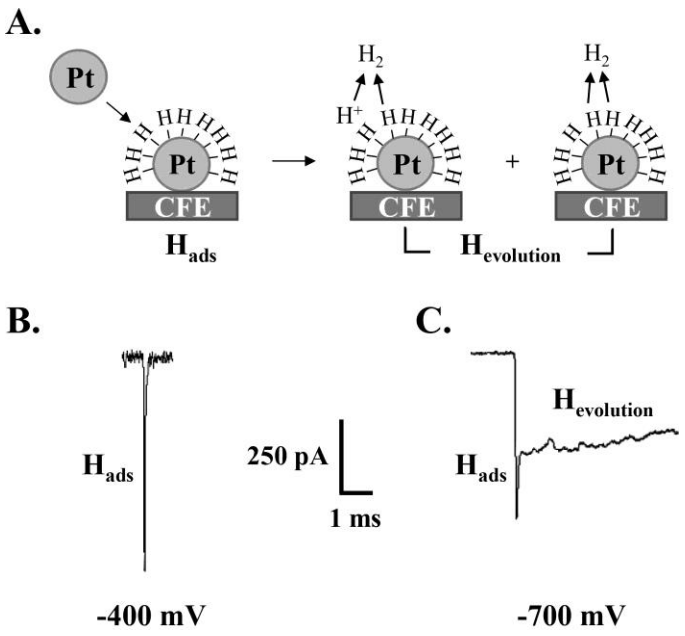

Figure 2.4. Proposed Mechanism for Ultrafast Collision Peaks.

(A) Diagram illustrating the proposed mechanism for the fast spike, slow decay observed peak shape. The Pt NPs undergo hydrogen adsorption upon collision with the electrode, yielding the fast spike. Hydrogen evolution subsequently occurs if enough overpotential is applied, giving rise to the slow decay. (B) The fast spike is due to hydrogen adsorption on the colliding Pt NP. (C) The slow decay is due to hydrogen evolution.

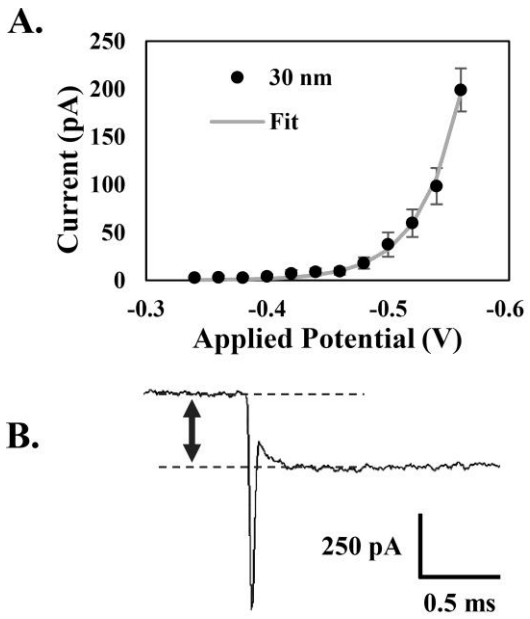

Figure 2.5. Plot of HER Steady-State Current vs. Applied Potential for 30 nm Pt NPs.

A nonlinear regression method was used to fit the curve with Equation 8, suggesting that the Heyrovsky step is rate-determining for the HER on colliding Pt NPs. Kinetic parameters of k^0 = $2.58 \times 10^{-3} \pm 1.2 \times 10^{-2}$ m/s, $K^0 = 5.56 \times 10^{-3} \pm 3.7 \times 10^{-8}$ mM^{-1} , and $\alpha = 0.77 \pm 0.15$ were extracted as the three fitting parameters. The values of 'n' for (A) are equal to 25. (B) The definition of the hydrogen evolution steady-state current is displayed. It is determined by taking the difference between the baseline current before the spike and the decayed current value after the spike.

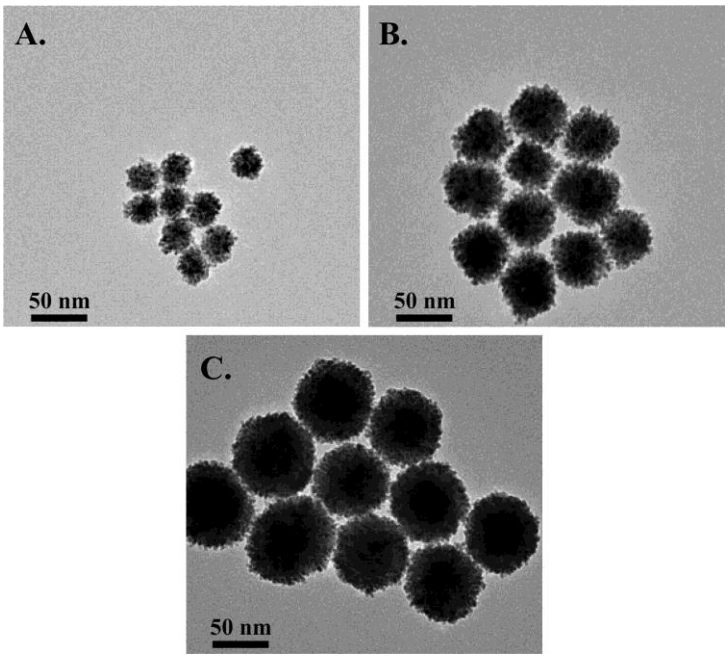

Figure 2.6. TEM Images of 30, 50, and 70 nm Pt NPs.

TEM images showing the surface roughness of (A) 30 nm, (B) 50 nm, and (C) 70 nm Pt NPs. The surface roughness of the 30, 50, and 70 nm NPs were measured to be approximately 10.3 ± 2.0, 14.1 ± 4.8, and 17.1 ± 1.6, respectively, using the reported microjet collision experiment.

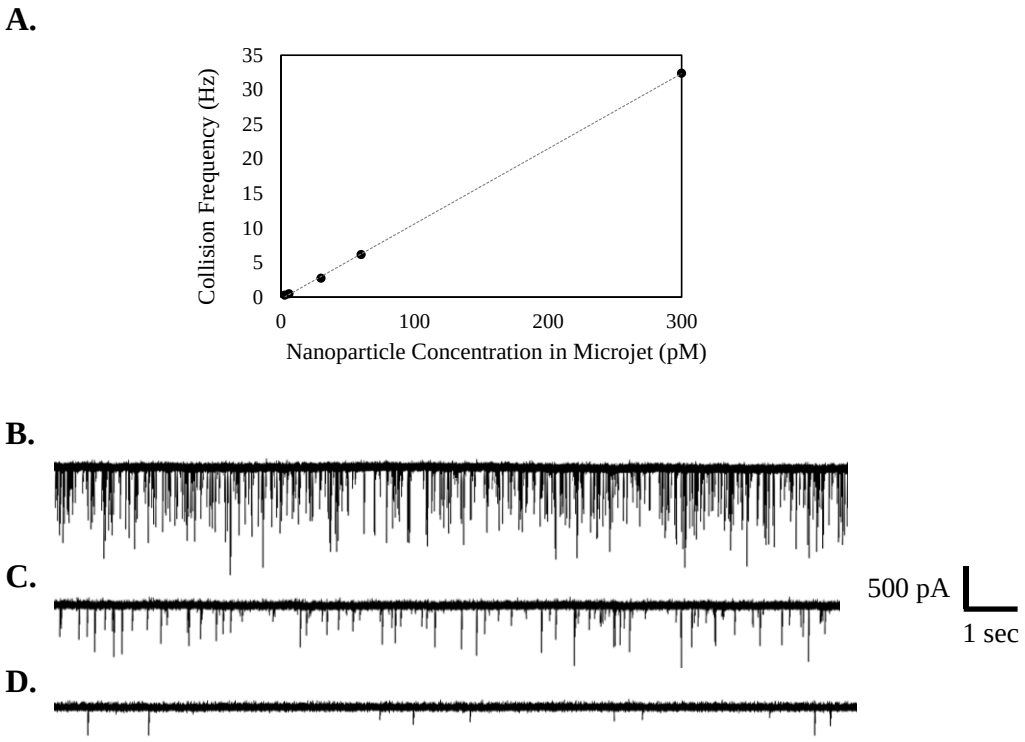

Figure 2.7. Concentration-Dependent Collision Frequency.

(A) A plot of collision frequency at various nanoparticle concentrations recorded at -400 mV in 25 mM $HClO_4$ concentration on the electrode surface. A linear correlation indicates that each peak is from a single nanoparticle. (B-D) *i-t* traces recorded at -400 mV and 300 pM (B), 60 pM (C), and 6 pM (D) 30 nm platinum NP concentration inside the microjet pipette.

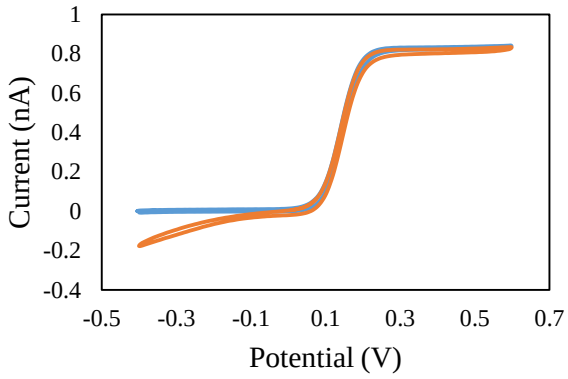

Figure 2.8. Cyclic Voltammogram of UME Before and After NP Collision Experiment.

Cyclic Voltammograms of a CFE in 1 mM ferrocenemethanol and 100 mM KCl before (blue), and after (orange) a microjet particle collision experiment collected at -400 mV applied potential. The oxygen reduction wave measured here starting at -100 mV is indicative that platinum nanoparticles have stuck to the electrode surface.

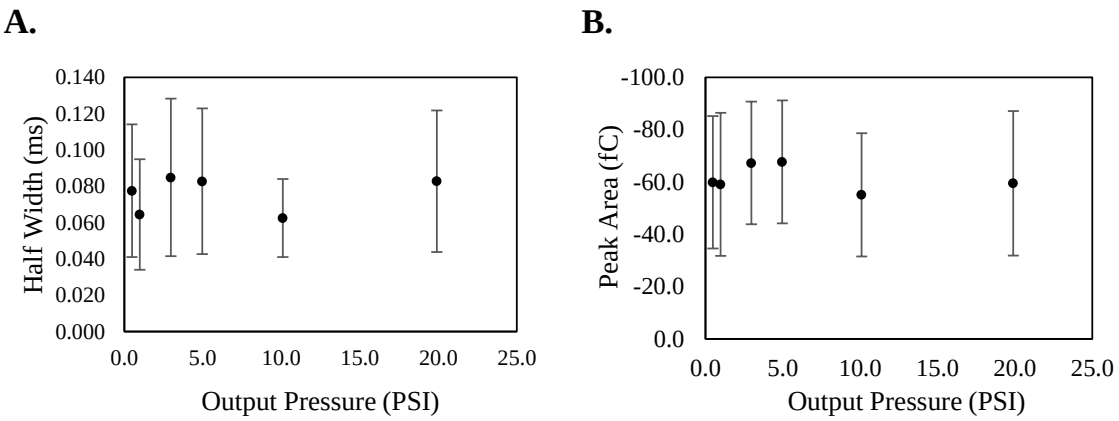

Figure 2.9. Peak Size vs. Microjet Output Pressure.

(A) Hydrogen adsorption half width and (B) peak area at various microjet output pressures recorded at -400 mV with 25 mM $HClO_4$ on the electrode surface. Since neither peak parameter is pressure dependent, this provides evidence that the nanoparticles during the fast spike events are not being pushed off the electrode surface with applied pressure. The 'n' values for these data are over 50.

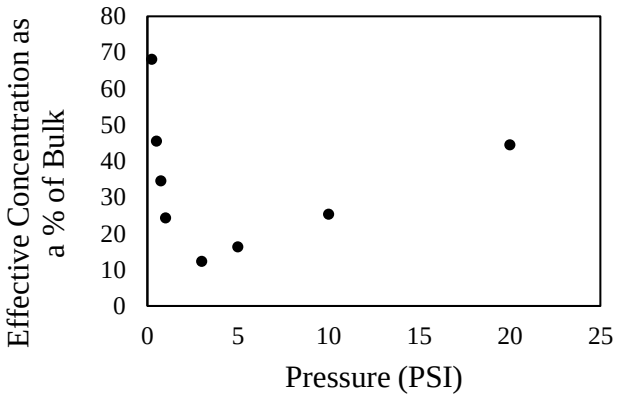

Figure 2.10. Effective Redox Concentration on the Electrode Surface.

Here we plot the effective concentration on the electrode surface as a function of applied pressure from the microjet, investigating the effect of solution displacement on measured electrode concentration.

Figure 2.10 Discussion.

In this experiment, the microjet was filled with 2 mM sodium citrate, while the bulk concentration was 700 mM ferrocyanide with 50 mM KCl. A sufficiently oxidizing potential was applied to oxidize the ferrocyanide and steady state currents were measured at varying different applied pressures. Identical microjet geometry with 1 PSI pressure at a 10 μm distance were maintained throughout all experiments presented in this report, therefore approximately 25% of the bulk acid concentration in reported experiments was the effective concentration on the surface of the electrode. Concentration values in the text are reported as the effective concentration on the electrode surface.

When a particle lands on the surface of the electrode in the main microjet particle collision experiments, the mass transfer of the acid to the particle is likely dominated by pressure-induced convection, rather than diffusion. However, this is accounted for in our control ferricyanide experiment above, since the same applied pressure profile is influencing the ferricyanide mass transfer.

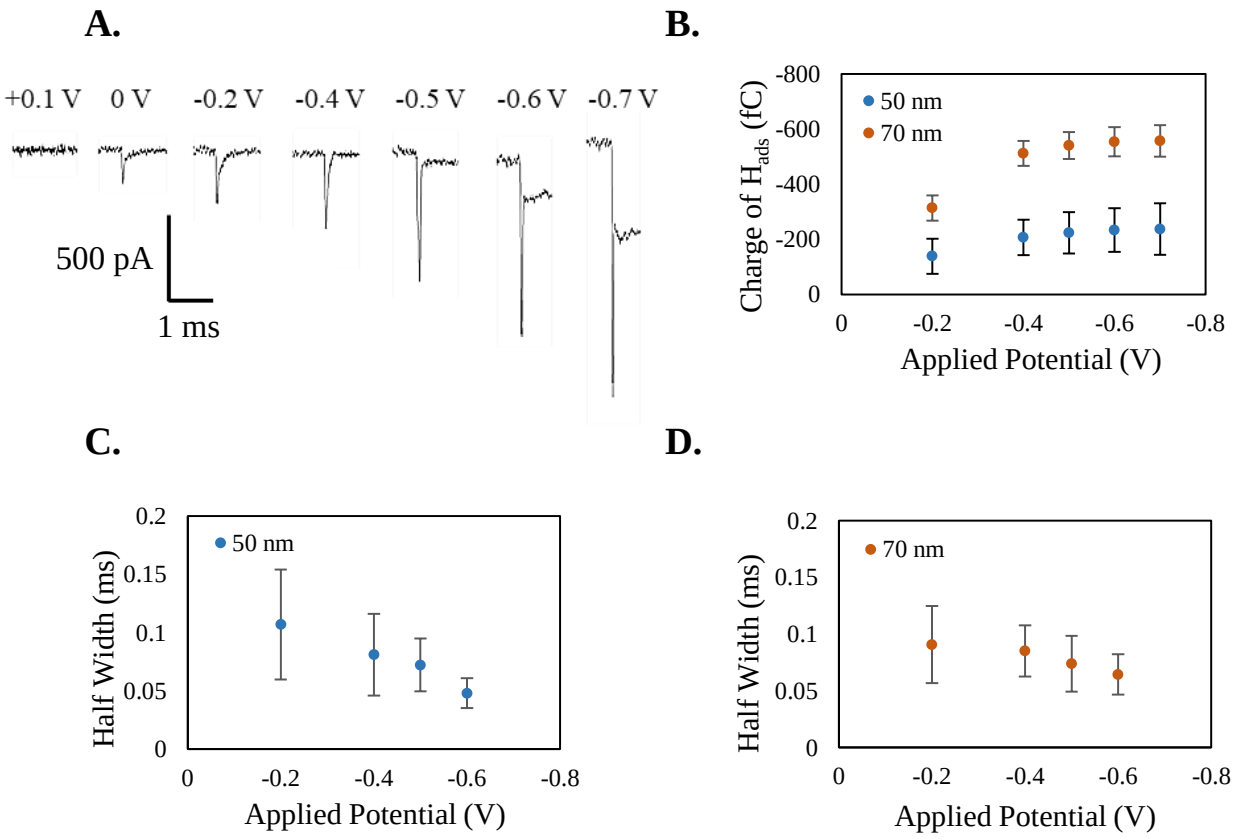

Figure 2.11. Potential-Dependent Microjet Collisions for 50, 70 nm Pt NPs.

(A) Integration of the fast hydrogen adsorption spike at various applied potentials for 50 and 70 nm platinum nanoparticles. The charge approaches -233 fC for 50 nm nanoparticles at -400 mV, and -554 fC for 70 nm nanoparticles at -500 mV. (B) The half width of the fast H_{ads} spike at various potentials for 50 nm platinum nanoparticles. (C) The half width of the fast H_{ads} spike at various potentials for 70 nm platinum nanoparticles. The 'n' value for the 50 nm and 70 nm data is 30.

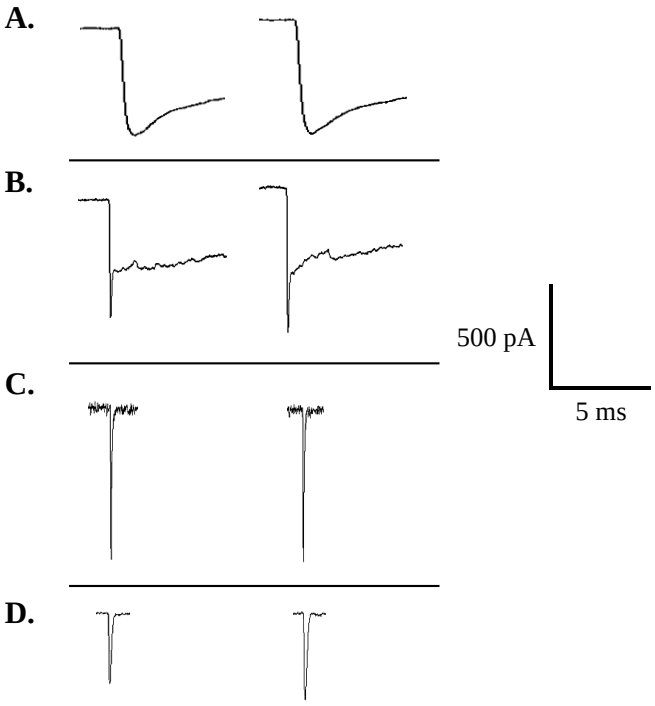

Figure 2.12. The Effect of Instrumental Filter Frequency on Peak Shape.

(A) and (B) are representative NP collision peaks recorded on 30 nm Pt NPs in 25 mM $HClO_4$ at different potentials and filtering frequencies: -700 mV and 1 kHz (A), -700 mV and 10 kHz (B). (C) and (D) are peaks collected at-400 mV on 30 nm Pt NPs in 25 mM $HClO_4$ in a microjet system (C) and in a diffusion-based beaker system (D).

Figure 2.12 Discussion.

While previous reports studying HER on colliding NPs do not always specify their filter frequency, we were able to mimic their peak shapes at -700 mV, absent of the fast spike, with a 1 kHz filter in diffusion-limited conditions (A).[21] By simply applying a 10 kHz filter instead, the fast spike becomes visible (B). This finding is consistent with recent NP collision studies, where the use of high-bandwidth recording allows the temporal resolution of multipeak collision dynamics on silver NPs.[51,52,53] (C) and (D) illustrate the differences between using a microjet and diffusion-limited systems, respectively. The microjet system generates a peak roughly 3 times faster (Table A.2.1) in width, demonstrating superior catalytic efficiency likely due to a reduction in the adsorbed contaminants as described in the main text.

Appendix 2.1

Tabular Data.

Table A.2.1. Peak Characteristics for Microjet and Diffusion-Limited Collisions.

	Microjet	Diffusion-Limited
Charge of H_{ads} Spikes (fC)	-61.0 ± 8.7	-55.6 ± 9.6
Half Width (ms)	0.077 ± 0.036	0.25 ± 0.14

Average hydrogen adsorption charge and half width recorded at -400 mV in 25 mM $HClO_4$ and filtered at 10 kHz. Note that the beaker peak half width is approximately 3 times longer than the microjet peak half width. Peaks are illustrated in Figure 2.12C and 2.12D. The ‘n’ values for the microjet data is equal to 35, while the ‘n’ values for the diffusion data is equal to 20.

Table A.2.2. Calculated Electroactive Surface Area and Roughness Factors for Pt NPs.

NP Diameter (nm)	Predicted Charge (fC)	Measured Charge (fC)	Roughness Factor	EASA (μm^2)
30	5.94	61.4 ± 11.9	10.3 ± 2.0	3.18 ± 0.6
50	16.49	233.1 ± 79.2	14.1 ± 4.8	12.1 ± 4.1
70	32.33	553.8 ± 52.6	17.1 ± 1.6	28.7 ± 2.7

The measured charge, roughness factor, and EASA values are reported as the average ± 1 standard deviation. We note that 'n' = 35 for the 30 nm data, 'n' = 35 for the 50 nm data, and 'n' = 45 for the 70 nm data.

Appendix 2.2

Calculation of HER Kinetic Parameters.

Here we will explain how the kinetic parameters k^0, K^0, and α were extracted from the nanoparticle collision data. We explicitly followed the recently published method by Luo et al.[44] We first measured the steady state current of the $H_{evolution}$ reaction by measuring difference between the baseline current before the collision peak and the decay current following the H_{ads} spike, shown in Figure 2.5B. The steady state current was averaged for over 25 peaks at each potential condition. The steady state current, i, was converted to electron transfer current (i_{et}) by subtracting the mass transfer current (i_{mt}) using the Koutecký-Levich equation, shown in Equation 6. Here, F is faraday's constant (96,485 C/mol), n is the number of electrons transferred in a single redox process (1, since H_{ads} has already occurred), D_{H+} is the diffusion coefficient of H^+ in solution (7.8 $\times 10^{-5}$ cm^2/s), C_{H+} is the concentration of H^+ (25 mM), and r is the radius of the nanoparticle (1.5 $\times 10^{-8}$ m).

$$\frac{1}{i_{et}} = \frac{1}{i} - \frac{1}{i_{mt}} = \frac{1}{i} - \frac{1}{4\pi \ln(2) n F D_{H+} C_{H+} r} \qquad (6)$$

The i_{et} values were plotted versus applied potential ranging from -340 to -560 mV, as shown in Figure 2.5A. Potentials more positive than -340 mV yielded negligible steady state current values. Potentials more negative than -560 mv yielded currents larger than the i_{mt}, indicating that a second electrochemical process such as water reduction overlapped the HER current, and therefore these potential values were excluded from analysis.

The curve was then fit using a non-linear regression model with Equations 7-9, and k^0, K^0, and α as the three fitting parameters. Here, A is the nanoparticle surface area, a H^+ is the proton

activity estimated as C_{H+}, f is equal to F/RT (F is Faraday's constant, R is the universal gas constant, T is the temperature), η is the overpotential, k^0 is the standard rate constant, K^0 is the equilibrium constant for the Volmer step, and α is the transfer coefficient of the rate-determining step.

Volmer Step: $$i_{et} = nFAk^0 a_{H^+} \exp(-\alpha f \eta) \quad (7)$$

Heyrovsky Step: $$i_{et} = nFA \frac{k^0 K^0 \alpha_{H^+}^2 \exp(-\alpha f \eta)}{\exp(f\eta) + K^0 \alpha_{H^+}} \quad (8)$$

Tafel Step: $$i_{et} = nFAk^0 \left[\frac{K^0 \alpha_{H^+}^2}{\exp(f\eta) + K^0 \alpha_{H^+}}\right]^2 \quad (9)$$

The overpotential, η, was defined in reference to the thermodynamic potential of the H^+/H_2 couple at approximately -0.2 V.[61] Specifically, η was calculated by adding 0.2 V to the applied potential at each point.

The 'Solver' function in Microsoft Excel was used to fit the curve by minimizing the sum of the squared residuals. Equation 8 provided the best fit, demonstrating that the Heyrovsky reaction, was the rate-determining step. Extracted fitting parameters with values of $k^0 = 2.58 \times 10^{-3}$ m/s, $K^0 = 5.56 \times 10^{-3}$ mM^{-1} , $\alpha = 0.77$ were obtained. The generated fit was then overlaid with the data points, shown in Figure 2.5A.

Appendix 2.3

Calculation of Time NP Spends in Bulk Solution Before Collision.

This quantitative evaluation directly follows calculations reported by McKelvey et al.[65] The pressure driven flow in a conical nanopipette is related with a volumetric flow rate given by

$$Q = \frac{3\pi r_0^3 \Delta p}{8\eta cot\theta} \tag{10}$$

In our experiments, r^0 = 1.5 µm is the nanopipette radius, Δp = 1 psi is the applied pressure, η is the viscosity (1 × 10^{-3} Pa), and θ is the nanopipette cone angle (set to 10°), which gives Q = 4.83x10^{-12} m^3/s.

The fluid velocity is spherically symmetric and decreases with the square of the distance from the orifice, r, the radial component of the velocity can be described by

$$v(r) = \frac{Q}{4\pi r^2} \tag{11}$$

A fair approximation of the delivery time, t, can be obtained through assuming the particle follows a radial streamline and integrating the analytical expression for v^{-1} from Equation 12.

$$t = \int v^{-1} dr = \left(\frac{4\pi}{3Q}\right) r^3 \tag{12}$$

When r is 10 µm, t is 0.8 ms.

2.6 REFERENCES

(1) Daniel, M. C. M.; Astruc, D. Gold Nanoparticles: Assembly, Supramolecular Chemistry, Quantum-Size Related Properties and Applications toward Biology, Catalysis and Nanotechnology. *Chem. Rev.* **2004**, *104*, 293–346.

(2) Debe, M. K. Electrocatalyst Approaches and Challenges for Automotive Fuel Cells. *Nature.* **2012**, *486*, 43–51.

(3) Seh, Z. W.; Kibsgaard, J.; Dickens, C. F.; Chorkendorff, I.; Nørskov, J. K.; Jaramillo, T. F. Combining Theory and Experiment in Electrocatalysis: Insights into Materials Design. *Science*. **2017**, *146*, 1–12.

(4) Selamet, O. F.; Becerikli, F.; Mat, Mahmut, D.; Kaplan, Y. Development and Testing of a Highly Efficient Proton Exchange Membrane (PEM) Electrolyzer Stack. *Int. J. Hydrogen Energy* **2011**, *36*, 11480–11487.

(5) Kinoshita, K. Particle Size Effects for Oxygen Reduction on Highly Dispersed Platinum in Acid Electrolytes. *J. Electrochem. Soc.* **1990**, *137*, 845–848.

(6) Solla-Gullon, J.; Vidal-Iglesias, F. J.; Lopez-Cudero, A.; Garnier, E.; Feliu, J. M.; Aldaz, A. Shape-Dependent Electrocatalysis: Methanol and Formic Acid Electrooxidation on Preferentially Oriented Pt Nanoparticles. *Phys. Chem. Chem. Phys.* **2008**, *10*, 3689–3698.

(7) Tang, Y.; Cheng, W. Nanoparticle-Modified Electrode with Size- and Shape-Dependent Electrocatalytic Activities. *Langmuir*. **2013**, *29*, 3125–3132.

(8) Sanles-sobrido, M.; Correa-duarte, M. A.; Carregal-romero, S.; Rodriguiez-Gonzalez, B.; Alvarez-Puebla, R. A.; Herves, P.; Liz-Marzan, L. M. Highly Catalytic Single-Crystal Dendritic Pt Nanostructures Supported on Carbon Nanotubes. *Chem. Mater.* **2009**, *21*, 1531–1535.

(9) Wang, S.; Kuai, L.; Huang, Y.; Yu, X.; Liu, Y.; Li, W.; Chen, L.; Geng, B. A Highly Efficient, Clean-Surface, Porous Platinum Electrocatalyst and the Inhibition Effect of Surfactants on Catalytic Activity. *Chem. Eur. J.* **2013**, *19*, 240–248.

(10) Zalitis, C. M.; Kucernak, A. R.; Sharman, J.; Wright, E. Design Principles for Platinum Nanoparticles Catalysing Electrochemical Hydrogen Evolution and Oxidation Reactions: Edges Are Much More Active than Facets. *J. Mater. Chem. A.* **2017**, *5*, 23328–23338.

(11) Sambur, J. B.; Chen, P. Approaches to Single-Nanoparticle Catalysis. *Annu. Rev. Phys. Chem.* **2014**, *65*, 395–422.

(12) Chen, J.; Lim, B.; Lee, E. P.; Xia, Y. Shape-Controlled Synthesis of Platinum Nanocrystals for Catalytic and Electrocatalytic Applications. *Nano Today*. **2009**, *4*, 81–95.

(13) Tao, A. R.; Habas, S.; Yang, P. Shape Control of Colloidal Metal Nanocrystals. *Small*. **2008**, *4*, 310–325.

(14) Kim, J.; Renault, C.; Nioradze, N.; Leonard, K. C.; Bard, A. J. Electrocatalytic Activity of Individual Pt Nanoparticles Studied by Nanoscale Scanning Electrochemical Microscopy. *J. Am. Chem. Soc.* **2016**, *138*, 8560–8568.

(15) Yu, Y.; Sun, T.; Mirkin, M. V. Scanning Electrochemical Microscopy of Single Spherical Nanoparticles: Theory and Particle Size Evaluation. *Anal. Chem.* **2015**, *87*, 7446–7453.

(16) Kang, M.; Perry, D.; Bentley, C. L.; West, G.; Page, A.; Unwin, P. R. Simultaneous Topography and Reaction Flux Mapping at and around Electrocatalytic Nanoparticles. *ACS Nano.* **2017**, *11* (9), 9525–9535.

(17) O'Connell, M. A.; Lewis, J. R.; Wain, A. J. Electrochemical Imaging of Hydrogen Peroxide Generation at Individual Gold Nanoparticles. *Chem. Commun.* **2015**, *51*, 10314–10317.

(18) Lai, S. C. S.; Dudin, P. V; Macpherson, J. V; Unwin, P. R. Visualizing Zeptomole ElectroCatalysis at Single Nanoparticles within an Ensemble. *J. Am. Chem. Soc.* **2011**, *133*, 10744–10747.

(19) Momotenko, D.; Byers, J. C.; McKelvey, K.; Kang, M.; Unwin, P. R. High-Speed Electrochemical Imaging. *ACS Nano*. **2015**, *9*, 8942–8952.

(20) Xiao, X.; Bard, A. J. Observing Single Nanoparticle Collisions at an Ultramicroelectrode by Electrocatalytic Amplification. *J. Am. Chem. Soc.* **2007**, *129*, 9610–9612.

(21) Xiang, Z. P.; Deng, H. Q.; Peljo, P.; Fu, Z. Y.; Wang, S. L.; Mandler, D.; Sun, G. Q.; Liang, Z. X. Electrochemical Dynamics of a Single Platinum Nanoparticle Collision Event for the Hydrogen Evolution Reaction. *Angew. Chemie - Int. Ed.* **2018**, *57*, 3464–3468.

(22) Jiao, X.; Batchelor-McAuley, C.; Young, N. P.; Compton, R. G. Simultaneous Activity and Surface Area Measurements on Single Mesoporous Nanoparticle Aggregates. *Phys. Chem. Chem. Phys.* **2018**, *20*, 23847–23850.

(23) Elbert, K.; Hu, J.; Ma, Z.; Zhang, Y.; Chen, G.; An, W.; Liu, P.; Isaacs, H. S.; Adzic, R. R.; Wang, J. X. Elucidating Hydrogen Oxidation/Evolution Kinetics in Base and Acid by Enhanced Activities at the Optimized Pt Shell Thickness on the Ru Core. *ACS Catal.* **2015**, *5*, 6764–6772.

(24) Stockmann, T. J.; Angelé, L.; Brasiliense, V.; Combellas, C.; Kanoufi, F. Platinum Nanoparticle Impacts at a Liquid|Liquid Interface. *Angew. Chemie.* **2017**, *129*, 13678–13682.

(25) Kleijn, S. E. F.; Serrano-Bou, B.; Yanson, A. I.; Koper, M. T. M. Influence of Hydrazine-Induced Aggregation on the Electrochemical Detection of Platinum Nanoparticles. *Langmuir*. **2013**, *29*, 2054–2064.

(26) Robinson, D. A.; Kondajji, A. M.; Castan, A. D.; Dasari, R.; Crooks, R. M.; Stevenson, K. J. Addressing Colloidal Stability for Unambiguous Electroanalysis of Single Nanoparticle Impacts. *J. Phys. Chem. Lett.* **2016**, *7*, 6–11.

(27) Dasari, R.; Robinson, D. A.; Stevenson, K. J. Ultrasensitive Electroanalytical Tool for Detecting, Sizing, and Evaluating the Catalytic Activity of Platinum Nanoparticles. *J. Am. Chem. Soc.* **2013**, *135*, 570–573.

(28) Zhou, H.; Fan, F. R. F.; Bard, A. J. Observation of Discrete Au Nanoparticle Collisions by Electrocatalytic Amplification Using Pt Ultramicroelectrode Surface Modification. *J. Phys. Chem. Lett.* **2010**, *1*, 2671–2674.

(29) Zhou, M.; Yu, Y.; Hu, K.; Xin, H. L.; Mirkin, M. V. Collisions of Ir Oxide Nanoparticles with Carbon Nanopipettes: Experiments with One Nanoparticle. *Anal. Chem.* **2017**, *89*, 2880–2885.

(30) Choi, Y. D.; Jung, S. Y.; Kim, K. J.; Jung, S. Combined Blip and Staircase Response of Ascorbic Acid-Stabilized Copper Single Nanoparticle Collision by Electrocatalytic Glucose Oxidation. *Chem. Asian. J.* **2016**, *701*, 1338–1342.

(31) Macpherson, J. V; Marcar, S.; Unwin, P. R. Microjet Electrode : A Hydrodynamic Ultramicroelectrode with High Mass-Transfer Rates. *Anal. Chem.* **1994**, *66*, 2175–2179.

(32) Macpherson, J. V; Simjee, N.; Unwin, P. R. Hydrodynamic Ultramicroelectrodes: Kinetic and Analytical Applications. *Electrochim. Acta*. **2001**, *47*, 29–45.

(33) Macpherson, J. V; Beeston, M. A.; Unwin, P. R. Imaging Local Mass-Transfer Rates within an Impinging Jet and Studies of Fast Heterogeneous Electron-Transfer Kinetics Using the Microjet Electrode. *J. Chem. Soc. Faraday Trans.* **1995**, *91*, 899–904.

(34) Bitziou, E.; Rudd, N. C.; Edwards, M. A.; Unwin, P. R. Visualization and Modeling of the Hydrodynamics of an Impinging Microjet. *Anal. Chem.* **2006**, *78*, 1435–1443.

(35) Melville, J. L.; Coles, B. A.; Compton, R. G.; Simjee, N.; Macpherson, J. V.; Unwin, P. R. Hydrodynamics and Mass Transport in Wall Tube and Microjet Electrodes. Simulation and Experiment for Micrometer-Scale Electrodes. *J. Phys. Chem. B.* **2003**, *107*, 379–386.

(36) Jiang, J.; Huang, X.; Wang, L. Effect of Forced Convection on the Collision and Interaction between Nanoparticles and Ultramicroelectrode. *J. Colloid Interface Sci.* **2016**, *467*, 158–164.

(37) Xiao, X.; Fan, F. F.; Zhou, J.; Bard, A. J. Current Transients in Single Nanoparticle Collision Events. *J. Am. Chem. Soc.* **2008**, *130*, 16669–16677.

(38) Woods, R. *Chemisorption at Electrodes: Hydrogen and Oxygen on Noble Metals and Their Alloys in Electroanalytical Chemistry;* Bard, Allen, J., Ed.; Marcel Dekker Inc.: New York, **1976**; Vol. 9, pp 1–144.

(39) Barna, G. G.; Frank, S. N.; Teherani, T. H. A Scan Rate Dependent Determination of Platinum Areas. *J. Electrochem. Soc.* **1982**, *129*, 746.

(40) Zhan, D.; Velmurugan, J.; Mirkin, M. V. Adsorption / Desorption of Hydrogen on Pt Nanoelectrodes: Evidence of Surface Diffusion and Spillover. *J. Am. Chem. Soc.* **2009**, *131*, 14756–14760.

(41) Chen, S.; Kucernak, A. Electrocatalysis under Conditions of High Mass Transport: Investigation of Hydrogen Oxidation on Single Submicron Pt Particles Supported on Carbon. *J. Phys. Chem. B.* **2004**, *108*, 13984–13994.

(42) Oja, S. M.; Zhang, B. Imaging Transient Formation of Diffusion Layers with Fluorescence-Enabled Electrochemical Microscopy. *Anal. Chem.* **2014**, *86*, 12299–12307.

(43) Adams, K. L.; Jena, B. K.; Percival, S. J.; Zhang, B. Highly Sensitive Detection of Exocytotic Dopamine Release Using a Gold-Nanoparticle-Network Microelectrode. *Anal. Chem.* **2011**, *83*, 920–927.

(44) Chen, Q.; Luo, L. Correlation between Gas Bubble Formation and Hydrogen Evolution Reaction Kinetics at Nanoelectrodes. *Langmuir.* **2018**, *34*, 4554–4559.

(45) Scherson, D. A.; Tolmachev, Y. V. Impurity Effects on Oxygen Reduction Electrocatalysis at Platinum Ultramicroelectrodes: A Critical Assessment. *Electrochem. Solid-State Lett.* **2010**, *13*, F1–F2.

(46) Jebaraj, A. J. J.; Georgescu, N. S.; Scherson, D. A. Oxygen and Hydrogen Peroxide Reduction on Polycrystalline Platinum in Acid Electrolytes: Effects of Bromide Adsorption. *J. Phys. Chem. C.* **2016**, *120*, 16090–16099.

(47) Zolfaghari, A.; Villiard, F.; Chayer, M.; Jerkiewicz, G. Hydrogen Adsorption on Pt and Rh Electrodes and Blocking of Adsorption Sites by Chemisorbed Sulfur. *J. Alloys Compd.* **1997**, *254*, 481–487.

(48) Zeng, M.; Li, Y. Recent Advances in Heterogeneous Electrocatalysts for the Hydrogen Evolution Reaction. *J. Mater. Chem. A.* **2015**, *3*, 14942–14962.

(49) Tavares, M. .; Machado, S. A. .; Mazo, L. . Study of Hydrogen Evolution Reaction in Acid Medium on Pt Microelectrodes. *Electrochim. Acta.* **2001**, *46*, 4359–4369.

(50) Robinson, D. A.; Edwards, M. A.; Ren, H.; White, H. S. Effects of Instrumental Filters on Electrochemical Measurement of Single-Nanoparticle Collision Dynamics. *ChemElectroChem.* **2018**, *5*, 1–10.

(51) Oja, S. M.; Robinson, D. A.; Vitti, N. J.; Edwards, M. A.; Liu, Y.; White, H. S.; Zhang, B. Observation of Multipeak Collision Behavior during the Electro-Oxidation of Single Ag Nanoparticles. *J. Am. Chem. Soc.* **2017**, *139*, 708–718.

(52) Robinson, D. A.; Liu, Y.; Edwards, M. A.; Vitti, N. J.; Oja, S. M.; Zhang, B.; White, H. S. Collision Dynamics during the Electrooxidation of Individual Silver Nanoparticles. *J. Am. Chem. Soc.* **2017**, *139*, 16923–16931.

(53) Ustarroz, J.; Kang, M.; Bullions, E.; Unwin, P. R. Impact and Oxidation of Single Silver Nanoparticles at Electrode Surfaces: One Shot versus Multiple Events. *Chem. Sci.* **2017**, *8*, 1841–1853.

(54) Markovic, N. M.; Grgur, B. N.; Ross, P. N. Temperature-Dependent Hydrogen Electrochemistry on Platinum Low-Index Single-Crystal Surfaces in Acid Solutions. *J. Phys. Chem. B.* **1997**, *101*, 5405–5413.

(55) Lukaszewski, M.; Soszko, M.; Czerwiński, A. Electrochemical Methods of Real Surface Area Determination of Noble Metal Electrodes - an Overview. *Int. J. Electrochem. Sci.* **2016**, *11*, 4442–4469.

(56) Trasatti, S.; Petrii, O. A. Real Surface Area Measurements in Electrochemistry. *Pure Appl. Chem.* **1991**, *63*, 711–734.

(57) Feltham, A. M.; Spiro, M. Platinized Platinum Electrodes. *Chem Rev.* **1971**, *71*, 177–193.

(58) Tremblay, M.; Martin, M. H.; Lebouin, C.; Lasia, A.; Guay, D. Determination of the Real Surface Area of Powdered Materials in Cavity Microelectrodes by Electrochemical Impedance Spectroscopy. *Electrochim. Acta.* **2010**, *55*, 6283–6291.

(59) Gira, M. J.; Tkacz, K. P.; Hampton, J. R. Physical and Electrochemical Area Determination of Electrodeposited Ni, Co, and NiCo Thin Films. *Nano Converg.* **2016**, *3*, 1–8.

(60) Truesdale, G. A.; Downing, A. L. Solubility of Oxygen in Water. *Nature*. **1954**, *173*, 1236.

(61) Bard, A. J.; Faulkner, L. J. *Electrochemical Methods: Fundamentals and Applications*, 2nd ed.; Wiley: New York, **2001**.

(62) Cogan, S. F.; Ehrlich, J.; Plante, T. D.; Gingerich, M. D.; Shire, D. B. Contribution of Oxygen Reduction to Charge Injection on Platinum and Sputtered Iridium Oxide Neural Stimulation Electrodes. *IEEE Trans. Biomed. Eng.* **2010**, *57*, 2313–2321.

(63) Srinivas, S. T.; Rao, P. K. Direct Observation of Hydrogen Spillover on Carbon-Supported Platinum and Its Influence on the Hydrogenation of Benzene. *J. Catal.* **1994**, *148*, 470–477.

(64) Prins, R. Hydrogen Spillover. Facts and Fiction. *Chem. Rev.* **2012**, *112*, 2714–2738.

(65) McKelvey, K.; Edwards, M. A.; White, H. S. Resistive Pulse Delivery of Single Nanoparticles to Electrochemical Interfaces. *J. Phys. Chem. Lett.* **2016**, *7*, 3920–3924.

Chapter 3. COLLISION, ADHESION, AND OXIDATION OF SINGLE SILVER NANOPARTICLES ON A POLYSULFIDE-MODIFIED MICROELECTRODE

3.1 INTRODUCTION

Ag nanoparticles (NPs) have been well-studied for many applications including therapeutics, optical sensors, and consumer products.[1,2] Variation in size, shape, and volume can influence their physical properties, including reactivity, and toxicity.[3,4] Accurate size-characterization techniques are therefore necessary for well-controlled experimentation. However, traditional methods such as transmission electron microscopy (TEM) and dynamic light scattering (DLS) struggle to accurately quantify the volume for non-ideal NP geometries, particularly when irregularities or defects are present.[5] Electron tomography may alternatively be used; however, this technique requires long analysis times with expensive instrumentation, thereby making it cost-prohibitive to measure a statistically relevant number of samples for multiple populations.[6] Instead, a rapid and inexpensive electrochemical methodology known as 'nanoparticle collision' has shown great promise toward Ag NP volumetric determination via counting the number of Ag atoms present in each particle.[7]

NP collision electrochemistry represents a broad field studying the reactivities and mechanisms for individual NPs interacting with electrodes.[8,9] Ag NP collision was initially developed by Compton and co-workers in 2011.[10] It relies on the use of an ultramicroelectrode (UME) biased at an anodic potential in dilute electrolyte solution to drive Ag oxidation across single NPs interacting or 'colliding' with the electrode. Individual collisions are recorded as sharp, positive-going amperometric current spikes whose integrated charge quantifies the number of

oxidized Ag atoms.[11] Full particle oxidation provides accurate volumetric sizing, applicable for providing representative bulk measurements or integration within electrochemical sensors.[12]

However, several studies in 2016 demonstrated the incomplete oxidation of Ag NP's over 50 nm in diameter, thereby highlighting the limits of the technique.[13–15] Mechanistic studies utilizing high temporal resolution amperometry revealed a multipeak signal proposed to be from NPs rapidly bouncing across the electrode surface.[13–15] Simulations have suggested that the NP only contacts the UME in rapid nanosecond-scale bursts due to its fast diffusional motion.[16] These studies utilized neutral electrolyte conditions and cited NP diffusion away from the electrode or movement to non-electroactive positions as the principle mechanisms preventing full oxidation.[17]

The long-standing 50 nm oxidation limit was surpassed by Long and co-workers in 2020 by utilizing an adhesive NP-UME mechanism.[18] The authors employed a bare Au electrode in alkaline phosphate solution such that colliding NPs favorably formed Ag oxide *in-situ* which promoted their adhesion. Amperometric peaks with long 20 ms decays were reported due to the slow dissolution of adsorbed Ag oxide. However, their supporting figures show very broad distributions of oxidation efficiencies for 65 nm diameter NPs which suggests that only a portion of the colliding NPs underwent complete oxidation. Similarly broad trailing distributions were obtained in a separate publication from Long and co-workers utilizing the same electrolyte condition for 60 nm Ag NPs.[19]

In the present work, we investigate the influence of Ag NP collision electrochemistry using an Au electrode pre-modified with an adhesive polysulfide layer in thiosulfate electrolyte. Au undergoes a unique surface-adsorbed electrochemical pathway in alkaline sodium thiosulfate that deposits a thin passivating polysulfide film (S^0) across its surface, described in Equation 1.[20]

$$S_2O_3 + H_2O \leftrightarrows S^0 + SO_4^{2-} + 2e^- \quad (1)$$

The film inhibits further thiosulfate oxidation, yet is only estimated to be a few layers thick, thereby resulting in a structure that still permits Ag oxidation via electron tunneling.[20,21]

The impressive strength of Au-thiol bonds has previously been used to create self-assembled monolayers (SAMs) from long-chain organic thiols,[22] as well as to develop biosensors from thiolated biomolecules.[23] Here, absent of any organic linker, the polysulfide layer serves as a dual-facing adhesive surface. Sulfur has strong interactions between both the Au electrode and the colliding Ag NPs,[24] with one study estimating the strength of Ag-S bonds as an impressive 25% of the notoriously strong Au-S bonds.[25] Thus, single Ag NPs which come in contact with the electrode surface will stick to the adhesive polysulfide film while undergoing electro-oxidation.

Our results suggest that the polysulfide layer directly reacts with Ag NPs to form Ag_2S, thus improving the rate of oxidation over diffusion-controlled systems. Despite the high insolubility of Ag_2S,[26] the use of bulk sodium thiosulfate as a Lewis base vastly increase the solubility of silver salts via formation of a metal complex ($K_f = 1.7 \times 10^{13}$ for $Ag(S_2O_3)_2^{3-}$). In a direct comparison with control studies, we find up to a 25x increase in collision frequency, 3x increase in peak amplitude, and more accurate quantitation for 60 nm Ag NPs. Volumetric measurements are compared between 30, 40, 60, 80, and 100 nm populations sized using NP collision data and TEM. By acknowledging that TEM overestimates quasi-spherical NP volumetric measurements, as explained in detail later, our results demonstrate the possibility of full NP oxidation up to 100 nm diameter. Mechanistic implications are further discussed to explain the manner in which this simple methodology so dramatically improves the electron transfer behavior of colliding Ag NPs.

3.2 Experimental Section

3.2.1 *Chemicals*

All chemicals were used as received from the manufacturer and include sodium thiosulfate pentahydrate ($Na_2S_2O_3 \cdot 5H_2O$, 100%, Fisher Chemical), sodium hydroxide (NaOH, 98.5%, J.T. Baker), potassium chloride (KCl, 100%, Fisher Chemical), ferrocenemethanol (FcMeOH, 97%, Sigma Aldrich), and sodium citrate dihydrate (100%, J.T. Baker). Commercial Ag nanoparticles with 30, 40, 60, 80, and 100 nm diameters stored in 2 mM trisodium citrate were purchased from Nanocomposix (San Diego, CA). Solutions were prepared with nanopure water purified to a resistivity of 18.2 MΩ cm^{-1} (Barnstead Nanopure system, Thermo Scientific).

3.2.2 *Electrode Preparation*

The 25-μm diameter Au disc UMEs were fabricated as previously reported.[14] Electrodes were screened for ideal voltammetric behavior using cyclic voltammetry in 1 mM FcMeOH and 100 mM KCl. UMEs were freshly polished with fine sandpaper and rinsed with excess DI water prior to all experiments. Ag/AgCl quasi-reference electrodes were prepared by immersing Ag wire (99.99% Alfa Aesar) in bleach for at least 1 hour. All collision experiments were performed with freshly chlorided and coiled wires.

3.2.3 *Instrumentation*

Chronoamperometric NP collision traces were collected using a low-noise current amplifier with an internal low-pass filter of 10 kHz (Axopatch 200B, Molecular Devices) and digitized with high temporal resolution at a sampling rate of 100 kHz (DigiData 1440b). Amperometric measurements were recorded within two home-built faraday cages located on a

vibration isolation table. Each cage was externally grounded and closed. The internal faraday cage rested on thick 6" foam padding to further isolate vibrations due to movement in the surrounding area. Amperometric traces were recorded with Axoscope 11.1 software and analyzed using a custom Python script as described in Appendix 3.1.

Cyclic voltammograms (CVs) were recorded using a LabVIEW program created in-house. Potential was swept with an external function generator (EG&G Parc Model 175) and high sensitivity current was measured with a Chem-Clamp current amplifier (Dagan Corporation). CVs were recorded within a grounded and closed home-built faraday cage resting on top of thick foam padding.

3.2.4 *Single Nanoparticle Collision Experiments*

NP collision experiments were performed in 5 mL volumes for each reported electrolyte condition. The 25 μm Au UME and Ag/AgCl quasi-reference electrodes were dipped in the electrolyte solution and leads applying +600 mV were connected while recording the amperometric current. In the presence of thiosulfate, the initial current response either produced a stable baseline or immediately overloaded due to thiosulfate oxidation and subsequent thiol modification, as shown in Figure 3.2b. The duration of current overload was used to estimate the reproducibility of the modified thiol layer. It was experimentally found that switching the potential from 600 mV to 0 V for 30 seconds and back to 600 mV produced a relatively consistent overload duration of 4-5 minutes. Following the potential pulse and observation of a steady baseline near 0 pA, 300 μL of stock Ag NP's were injected and mixed in the solution. The resulting diluted Ag NP concentrations for each NP size are displayed in Appendix 3.2.

Control experiments performed in thiosulfate but without the thiol modification were recorded from traces where anodic current was not observed upon initial potential application.

Control experiments without thiosulfate were performed with the same potential pulse procedure, except the overloading current spike was not observed.

The solution condition of 10 mM $Na_2S_2O_3$ 10 mM NaOH was selected following parameter optimization to both avoid NP aggregation and facilitate ease of recording. A more detailed discussion is included in Appendix 3.3.

We note that all reported electrolyte solutions contained 120 μM citrate due to the presence of 2 mM citrate within the injected NP aliquot. The solutions used for cyclic voltammetry in Figure 3.1b and Appendix 3.4 were spiked with the same citrate concentration to maintain consistency.

3.2.5 *Nanoparticle Characterization*

TEM was performed using a FEI Technai G2 F20 TEM operating at 200 kV with a single tilt sample holder and Gatan Ultrascan CCD camera. The 30, 40, 60, 80, and 100 nm Ag NP's were each dropcast onto separate carbon-coated copper TEM grids (Electron Microscopy Sciences). The TEM images were analyzed with the 2-D projection method, outlined in Appendix 3.5, to provide an estimated equivalent spherical diameter distribution for NP's of each sample.

3.3 Results and Discussion

3.3.1 *Thiosulfate Electrochemistry and the Polysulfide Passivation Process*

The electrochemistry of alkaline thiosulfate on Au undergoes multiple reaction pathways depending on applied potential. Previous literature utilizing surface enhanced Raman scattering spectroscopy (SERS) has revealed the composition of surface adsorbed species under these various conditions.[27,28] Two reaction pathways are of significant interest to the present study. First, the Au electrode undergoes leaching with the thiosulfate between 0 and 0.1 V vs. Ag/AgCl, thereby promoting its own dissolution.[27] A monolayer of Au sulfide begins to form after long exposure,

where a fractional coverage of 0.35 was reported after 18 minutes at 0.1 V in 100 mM $Na_2S_2O_3$.[27] Second, as the potential is increased beyond 0.45 V, thiosulfate oxidation occurs at the Au electrode and produces a thin film of adsorbed S-S bonds existing as cyclo-octa sulfur (S_8) or polysulfide (Equation 1).[20] The polysulfide film passivates the Au electrode and inhibits continued leaching or thiosulfate oxidation.[29]

We represent the passivation process schematically in Figure 3.1a and qualitatively reproduce the cyclic voltammetric results in Figure 3.1b for our thiosulfate NP collision condition. After scanning the potential from -0.2 V to 0.7 V to -0.2 V, we observed that the leaching current at 0.1 V is almost negligible. The thiosulfate oxidation wave dominates the trace and peaks at 0.36 V with 34 nA and is followed by the expected rapid current decay indicative of electrode passivation with polysulfide. On the reverse scan, reduction of the film begins at -0.2V.

The sulfide film has been well-studied and has a set of known conditions required for its formation and stability. For example, the film's generation and electrode passivation is unique to Au, and specifically does not occur on other commonly used electrode materials including glassy carbon, Ag, and Pt. Further, its formation via the thiosulfate pathway requires alkaline conditions to avoid the acidic decomposition of thiosulfate in solution.[30] Once generated, the film is relatively stable at potentials ranging from +0.8 V to -0.2 V vs. Ag/AgCl where its own reduction begins to occur, as shown in Figure 3.1b.[31]

Previous literature suggests that the application of potentials above 0.45 V vs. Ag/AgCl would invoke thiosulfate oxidation and subsequent electrode passivation. In our amperometric experiments, thiosulfate oxidation was readily evident by the immediate overloading of the background current. The overloaded signal would occur for a few minutes before rapidly decaying back to ~ 0 pA, indicative of electrode passivation. However, occasionally initialization of the

potential at +0.6 V in 10 mM $Na_2S_2O_3$ 10 mM NaOH solution did not generate an anodic current. This phenomenon was also observed in cyclic voltammetry where potential onset at +0.3 V scanning positively to +0.7 V sometimes produced a flat signal. Only upon cycling back down through 0 V was this oxidation wave induced (Appendix 3.4). To overcome this inconsistency in our amperometric recordings and generate a reproducible polysulfide film, we applied a single potential pulse between +0.6 V to 0 V to +0.6 V prior to our NP collision experiments. This modification process generated a consistent overloading background current that decayed back to ~ 0 pA after 4-5 minutes.

It remains unclear as to why sweeping the potential through 0 V is required to consistently generate the passivating film. We speculate that formation of Au-sulfide nucleation zones may better anchor the film to the electrode surface, yet this would not explain the absence of anodic current. It may also be possible that freshly exposed Au following leaching may remove oxide impurities and be more reactive. Further studies with correlated spectroscopy would be required to better understand this behavior.

3.3.2 *Effects of the Polysulfide Modification on Ag NP Collision.*

In Figure 3.2 we demonstrate the qualitative effects of employing the polysulfide passivation layer on the Ag NP collision results. The trace was recorded in 10 mM $Na_2S_2O_3$ 10 mM NaOH with 19 pM diffuse 60 nm diameter Ag NPs. The first 22 minutes (Figure 3.2a) were recorded without the sulfide layer present, evidenced by the absence of anodic overloading current prior to NP injection; here we observed small infrequent peaks. At 22 minutes (Figure 3.2b) the potential was pulsed to 0 V for 30 seconds and back to 600 mV to invoke the polysulfide modification, evidenced by the current overloading for 5 minutes. With the polysulfide layer present, the NP collision signal was dramatically changed as shown in Figure 3.2c. We observed

large rapid peaks with a 9x increase in average collision frequency and 2.5x increase in average amplitude.

Closer inspection of the non-sulfide peaks reveals single collision events with 3x longer durations which indicate slower electron transfer kinetics. However, the absence of multipeaks suggests NP adhesion, possibly bound to interfacial layers of adsorbed thiosulfate[20] or sparse coverage of sulfurous thiosulfate decomposition products.[31] Herein, we propose two related interfacial mechanisms that help to explain the disparate Ag NP collision results with and without the polysulfide layer present.

One explanation for taller, faster peaks in the polysulfide-modified condition is that stronger NP adsorption achieved through a greater number of Ag-S bonds leads to improved electrical connection and faster electron transfer kinetics. Wang and co-workers recently found that "poor electrical contact" between nano-objects and electrodes can either hinder or eliminate electrochemical activity on the object.[32,33] The 9x increase in collision frequency also suggests more effective NP-UME interactions with sulfide present. Despite the increase, the theoretical diffusion-limited collision rate is still 12x higher than measured, suggesting that many collisions were undetected.

A second related mechanism indicates that colliding Ag NPs can directly react with the polysulfide film to form Ag_2S. The preconcentrated sulfide serves as a precursor toward the stable oxidation product, Ag_2S, as described in Equation 2.

$$2Ag + S^0 \leftrightarrows Ag_2S\ (s) \qquad (2)$$

The solid Ag_2S layer formed at the contact position can then react with the bulk thiosulfate to form $Ag(S_2O_3)^{2-}$ as a soluble species to enable improved dissolution, following Equation 3.

$$Ag_2S\ (s) + 4S_2O_3^{2-} \leftrightarrows 2Ag(S_2O_3)_2^{3-} + S^{2-} \quad (3)$$

Recent work by Robinson et al. studied the formation of Ag_2S on colliding Ag NPs within solutions of dilute alkaline HS^-.[26] The high insolubility of Ag_2S (pK_{sp} ~ 53.5) resulted in encapsulation of the core Ag and formed either core@shell Ag@Ag_2S NPs or void-containing Ag/Ag_2S NPs, thereby preventing full oxidation. In our experiments, the polysulfide layer serves to preconcentrate sulfide at the electrode surface to where it can take part in the Ag_2S transformation. Further, the presence of sodium thiosulfate as a Lewis base vastly increased the solubility of generated Ag_2S by a factor equivalent to its formation constant ($K_f = 1.7\times10^{13}$) which may eliminate the precipitated encapsulation effect described by Robinson et al. Our results of increased peak amplitude with polysulfide present could then be explained by the faster reaction of Ag with preconcentrated sulfide, relative to the diffusion-limited arrival of electrolyte in the non-polysulfide condition.

Figure 3.3 introduces results from two more control conditions that were selected based on their importance to previous Ag NP collision literature. "KCl Control" was collected with 20 mM KCl and is meant to be representative of more classical Ag NP conditions which almost exclusively used neutral single-electrolyte systems.[13–15,34] "Alkaline KCl" was collected with 10 mM KCl 10 mM NaOH in a similar manner to Long and co-worker's work using alkaline phosphate to generate Ag-oxide and promote NP adhesion through strong Au - Ag-oxide contacts.[18,19] Despite our choice to use chloride instead of phosphate, we still observed similar long peak decay events (~10 ms) in

Figure 3.3b and Appendix 3.10 which are suggestive of Ag-oxide formation and slow dissolution. Figure 3.3a shows representative traces of the first 10 minutes under each reported condition with 19 pM 60 nm Ag NPs, while Figure 3.3b shows representative peaks following baseline adjustment. Averaged collision frequencies and peak amplitudes are shown in Figures 3.3c and 3.3d, respectively.

As shown in Figure 3.3c, the thiosulfate with sulfide condition produces the highest collision frequency overall, with a collision rate 25.5x higher than the non-adhesive neutral control. The polysulfide adhesion layer also produces ~ 3.5x higher collision rate than the Ag-oxide adhesive mechanism described by Long and co-workers. Despite both conditions using an adhesive mechanism, we believe this result occurs because the Ag-oxide mechanism depends on the *in-situ* formation of the adhesion layer between the NP and UME. It is possible that some collisions do not form sufficient Ag-oxide to promote adhesion, whereas the adhesion layer is always present in the sulfide condition.

Secondly, we saw that alkaline KCl condition has a 3.3x higher collision frequency than thiosulfate without sulfide, despite maintaining the same NaOH concentration. This observation can be explained by considering the Lewis base identity of thiosulfate. The solubility of Ag oxide is significantly increased in its presence, where the equilibrium constant K (calculated by multiplying K_{sp} x K_f) of Ag-oxide in alkaline thiosulfate is 3.2×10^{5} (compared to the value of 1.9×10^{-8} in water[35]). More complete dissolution of Ag-oxide eliminates its adhesive contacts and lowers the rate of detected collisions for the alkaline thiosulfate condition in the absence of the sulfide adhesion layer.

Figure 3.3d compares the average peak amplitude for all data collected under the respective solution conditions. The peak amplitude is indicative of the flux of transferred electrons and is

correlated with the rate of electrochemical oxidation. We find that both thiosulfate-containing electrolyte conditions produces the highest peak amplitudes. This phenomenon is again due to the extreme solubility of Ag-thiosulfate oxidation products accommodating the massive influx of Ag^+ in the solution volume surrounding the NP. The basic KCl condition produced the lowest amplitude peaks due to the dominant formation of Ag-oxide which reportedly undergoes slow dissolution.

3.3.3 *Effects on Oxidation Efficiency from the Au-Sulfide Modified Electrode.*

We next investigated the influence of the sulfide adhesion layer on the integrated charge for each NP collision event. With Equation 4, the charge (Q) is used to estimate the radius, r, of an equivalent spherical particle.[10] Here, n = 1 electron, A_r is the atomic mass of Ag (107.87 g mol^{-1}), F is the Faraday constant (96 485 C mol^{-1}), and ρ is the density of silver (10.49 g cm^{-3}).

$$r = \left(\frac{3A_rQ}{4\pi nF\rho}\right)^{1/3} \qquad (4)$$

In Figure 3.4, we show the distributions of equivalent spherical NP diameters calculated with 60 nm Ag NP collision data using the same four control conditions as Figure 3.3. Each distribution was fit with a Gaussian function using the maximum likelihood estimate (MLE), where the mean of the fit is labeled on each respective plot.

We find that the Au-sulfide condition produces the largest estimated diameter of 54.3 nm compared to 51.8 nm for the alkaline KCl control, 48.9 nm for the non-sulfide thiosulfate, and 39.1 nm for the neutral KCl solution. Results suggest that larger oxidation efficiencies are obtained for conditions that better promote NP adhesion. This idea is consistent with initial multipeak papers

which cited diffusion of the NP away from the electrode as the main mechanism for incomplete oxidation.[13–15] Longer residence times on the electrode surface allow for ongoing dissolution of generated Ag salts and continued Ag oxidation.

One interesting observation from Figure 3.4 is that the distribution of oxidation efficiencies for the alkaline KCl condition is bimodal. These trailing results toward smaller diameters are consistent with previous literature for 60 and 65 nm Ag NP's in alkaline phosphate, though have not been directly discussed.[18,19] Here, the larger half of the bimodal distribution is centered at 55.1 nm, yielding results similar to those using the adhesive Au-sulfide condition. However, the smaller half of the distribution is centered at 33.6 nm and is more similar to the non-adhesive neutral KCl control condition. Given that oxidation efficiency is related to adhesive strength, these smaller events may result from collisions that fail to form sufficient Ag-oxide *in-situ* to promote adhesion, thereby resulting in quick incomplete events. Nonetheless, the existence of the second distribution centered at 33.6 nm pulls the MLE Gaussian fit lower to an overall average of 51.8 nm and a less accurate quantitative result.

In Figure 3.5, we investigate particle sizing results for 30, 40, 60, 80, and 100 nm Ag NPs using the Au-polysulfide oxidative collision method compared with TEM. We chose to plot data in terms of probability density fit with the kernel density estimate (KDE) to better show the distribution shape rather than forcing a symmetrical Gaussian fit. When comparing the maximum density values of each population, we observe identical equivalent spherical diameters for 30 nm Ag NPs with more significant deviations for larger particle sizes.

Previous Ag NP collision literature has treated TEM as an accurate volumetric reference to determine whether full NP oxidation had occurred.[18] However, researchers should be cautious when making this comparison. The process of volumetric sizing with TEM via the 2D projection

method quantifies the area of a 2D NP slice and uses the measured value to calculate the radius of an equivalent sphere, as described in Appendix 3.5. Thus, only perfect spheres produce perfectly accurate volumetric measurements.

An important study by Attota et al. explored the error of the 2D projection method by simulating 3D NP models of known volume with different degrees of surface roughness and non-sphericity.[36] They found that rough, faceted, and oblong NP geometries can have their volume overestimated by up to 18% using the same 2D projection method applied in TEM data analysis. Note that a constant percent overestimation leads to larger numerical differences for increased NP size. While this reference was published in 2016, we emphasize its importance since previous Ag NP collision papers have treated TEM volumetric sizing as ground truth and expressed the desire to exactly match these results. This quest is unproductive for large (>50 nm) quasi-spherical Ag NPs since the application of TEM with the 2D projection method will consistently overestimate the equivalent spherical diameter. A more realistic strategy would be to compare the percent difference between TEM and NP collision to ensure that it is within an appropriate error margin.

Indeed, our TEM results in Figure 3.6 and Appendix 3.6 confirm the presence of such faceted and oblong particles, especially for sizes greater than 40 nm diameter. The percent error between the maximum density values for our equivalent spherical diameters derived using NP collisions and TEM in Figure 3.5 exist as 5.1%, 11.3%, 10.4%, and 7.6% for the 40, 60, 80, and 100 nm Ag NP populations, respectively. Since these values are well within the 18% volumetric error margin of the 2D projection method, it remains possible that full particle oxidation is occurring. However, given that the error margin is so large, the use of additional analytical techniques could help to validate this result. One strategy would be to obtain a more accurate volumetric reference using a method such as electron tomography,[5,37] but such measurements

would be prohibitively expensive. Alternatively, correlated imaging strategies may enable observation of the physical processes which occur subsequent to each oxidative spike.[38,39]

Lastly, we observed that our 80 and 100 nm Ag NP collision results in Figure 3.5a show trailing distributions toward smaller particle sizes, indicative of incomplete oxidation. We believe the NPs in the trailing population are still adhered to the sulfide layer, due to the long durations of the events. For example, 100 nm events with less than 65 nm equivalent diameters had mean durations of 8.6 ms. One proposed mechanism for this process is that large Ag NPs may consume the local polysulfide adhesion layer and convert it to soluble Ag_2S with the aid of bulk thiosulfate. Eliminating the adhesive contact may then detach the NP and prevent further oxidation. Since the trailing peaks only account for a small percentage of the total number of events, the variable thickness of the polysulfide film could account for this inconsistent behavior. Further investigation with correlated imaging would better validate the mechanism that complicates the complete oxidation of large Ag NP sizes.

3.4 CONCLUSION

In this work we functionalized an Au electrode with a polysulfide film and investigated the manner in which this surface modification affected the detection of oxidative Ag NP electrochemical collisions. The film served both as an adhesive surface for colliding Ag NPs and as a pre-concentrated source of sulfide which facilitates the production of Ag_2S from oxidized Ag. Rapid NP dissolution was promoted by the presence of bulk sodium thiosulfate which served as a Lewis base to vastly improve the solubility of Ag_2S and Ag^+. Preliminary results with 60 nm Ag NPs suggest the presence of sulfide with thiosulfate resulted in a 25x increase in collision frequency, 3x increase in peak amplitude, and more complete oxidation. We further applied this methodology toward quantitative volumetric detection of quasi-spherical 30, 40, 60, 80, and 100

nm Ag NP populations and found reasonable evidence that full oxidation occurred for all NP sizes. However, we emphasize that the use of quasi-spherical NPs leads to an over-estimation of TEM equivalent spherical diameters, an artifact of TEM data analysis that is often overlooked in this field. Despite full oxidation being predominantly observed for 80 and 100 nm Ag NPs, we propose that consumption of the local polysulfide layer led to trailing distributions of estimated particle size. We believe that the use of a non-consumable adhesive layer applied to the electrode surface may resolve this issue and lead to more uniform and quantitative sizing for large Ag NPs. Lastly, we expect the observed NP adhesive properties of polysulfide to benefit other NP collision systems via promotion of more effective NP-UME electrical contact.

3.5 FIGURES

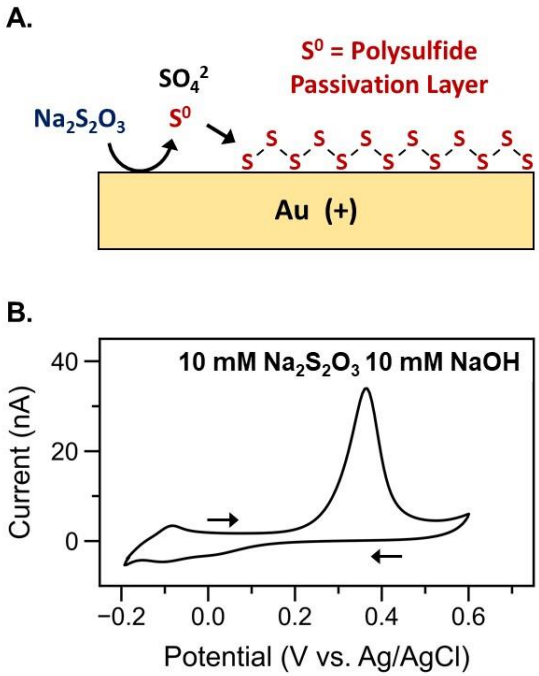

Figure 3.1. Surface Modification of Au Electrode with Polysulfide.

(A) A qualitative representation of the mechanism described in Equation 1, where the oxidation of alkaline thiosulfate results in the formation of a polysulfide passivation layer across the Au electrode surface. **(B)** A cyclic voltammogram in 10 mM $Na_2S_2O_3$ 10 mM NaOH swept from -0.2 V to 0.6 V to -0.2 V at 20 mV/s vs. Ag/AgCl. The large oxidation wave at 0.35V is due to thiosulfate oxidation. The rapid decline in current at 0.45 V is due to the passivation of the UME with the polysulfide layer, preventing further thiosulfate oxidation.

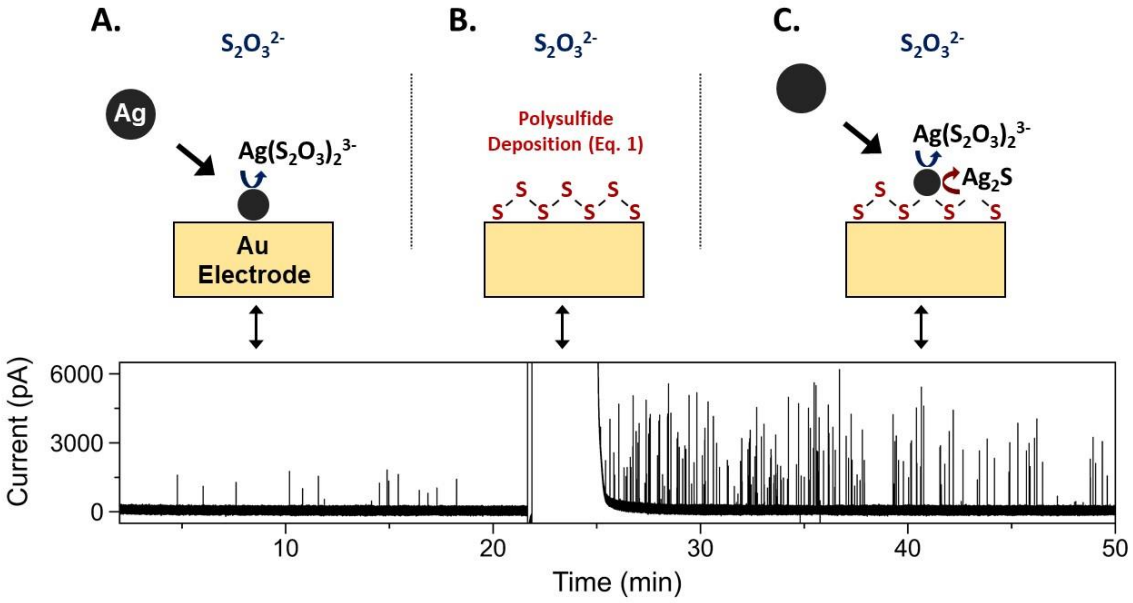

Figure 3.2. Correlated Mechanism and Amperometric Trace for Polysulfide Ag NP Collisions.

The entire trace above was recorded in 10 mM $Na_2S_2O_3$ 10 mM NaOH with 60 nm diameter Ag NPs at 19 pM. (A) For the first 22 minutes, particles collide onto a bare Au UME, forming $Ag(S_2O_3)_2^{3-}$ as a stable product. (B) Polysulfide is deposited onto the Au UME with application of a single potential pulse, as outlined in the text. Overloading current is from $Na_2S_2O_3$ oxidation and polysulfide deposition, as described in Equation 1. (C) A stable baseline is achieved following polysulfide passivation. The sulfide adheres colliding NPs and can directly react to form Ag_2S.

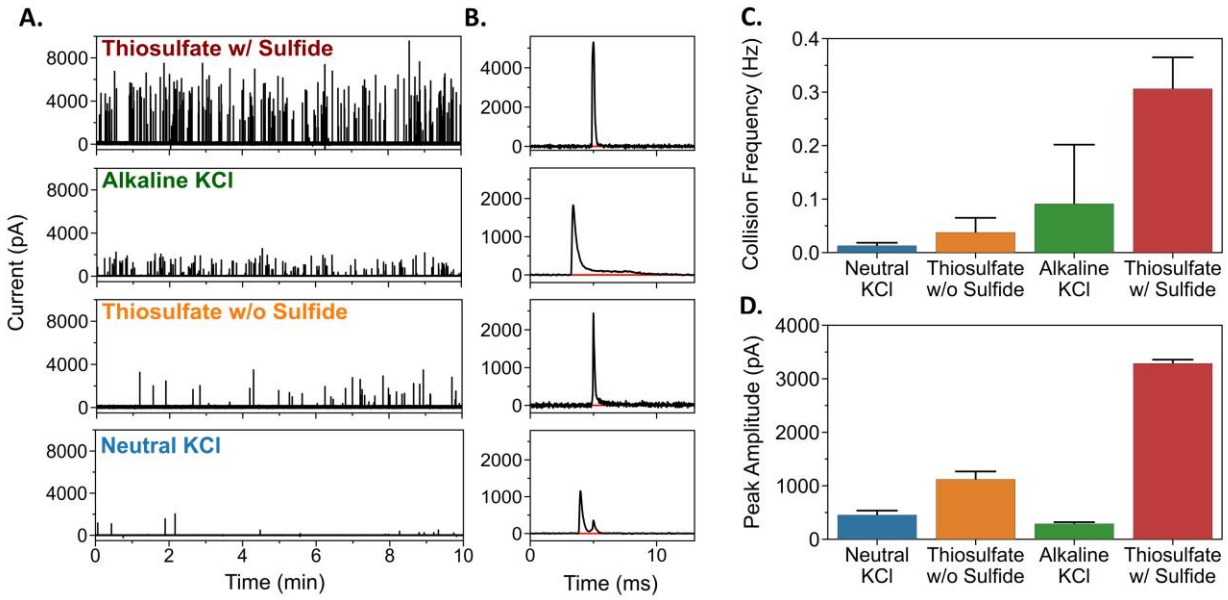

Figure 3.3. Comparison of Peak Amplitude and Collision Frequency for Four Control Conditions.

(A) Raw Ag NP Collision traces recorded immediately after injecting Ag NP's. Each trace is recorded with an identical 19 pM Ag NP concentration. Clear differences in collision frequency and peak amplitude are observed. (B) Representative peaks under each condition, following baseline adjustment. A horizontal red line is drawn at 0 pA to clearly show where each peak deviates from the baseline, such as for the trailing tail in the Alkaline KCl condition. Further examples of individual peaks are shown in Appendix 3.8-3.11. Note that the y-axis on the "Thiosulfate w/ Thiol" plot is scaled 2 times that of the others. (C) The average collision frequency quantified for the first 10 minutes of three traces under each reported condition. The first 10 minutes were selected to avoid influence of particle aggregation. (D) The average peak amplitudes for all quantified data. The error bars shown in C, D are for 1 standard deviation above the mean. Specific experimental conditions include: "Thiosulfate w/ Sulfide": 10 mM $Na_2S_2O_3$ 10 mM NaOH on a sulfide-modified Au UME (n = 1943); "Alkaline KCl": 10 mM KCl 10 mM NaOH on a bare Au UME (n = 619); "Thiosulfate w/o Sulfide": 10 mM $Na_2S_2O_3$ 10 mM NaOH on a bare Au UME (n= 143); "Neutral KCl": 20 mM KCl on a bare Au UME (n = 183).

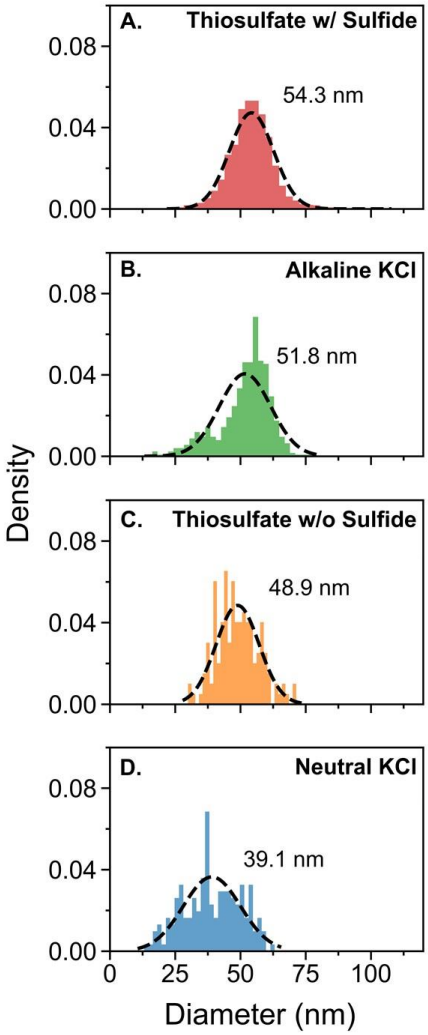

Figure 3.4. Sulfide-Modified Au UME Increases Oxidation Efficiency Relative to Controls.

The equivalent spherical diameter of 60 nm Ag NP's were calculated using the integrated charge and Equation 4 under various Ag NP electrolyte conditions. Specific experimental conditions include: (A) 10 mM $Na_2S_2O_3$ 10 mM NaOH on a sulfide-modified Au UME (n = 1943); (B) 10 mM KCl 10 mM NaOH on a bare Au UME (n = 619); (C) 10 mM $Na_2S_2O_3$ 10 mM NaOH on a bare Au UME (n = 143); (D) 20 mM KCl on a bare Au UME (n = 183). Each distribution was fit using a Gaussian Maximum Likelihood Estimation (MLE), including all data. The values reported on each plot are the mean of the Gaussian fit.

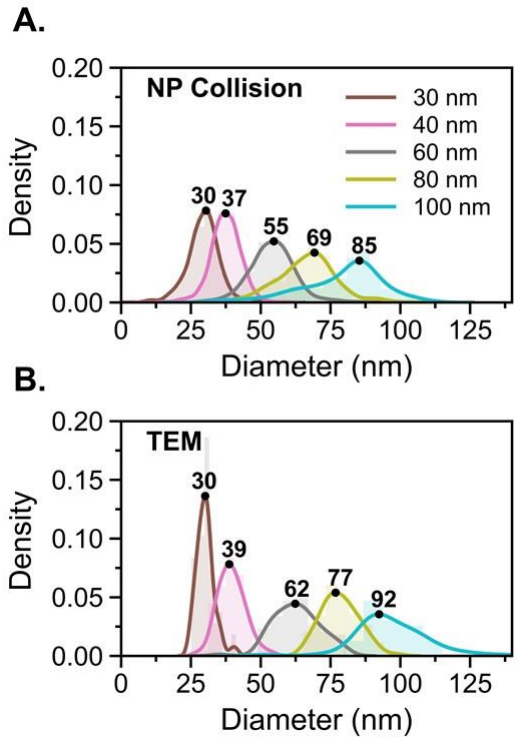

Figure 3.5. Quantitation of Ag NP Diameter for NP Collision vs. TEM.

(A) The sulfide-modified Au UME condition (10 mM $Na_2S_2O_3$ 10 mM NaOH) was used to quantify equivalent spherical diameter for Ag Collision data for NP's with diameters 30, 40, 60, 80, 100 nm using the integrated charge and Equation 4. (n = 722, 1498, 1943, 786, 557 for 30, 40, 60, 80, 100 nm Ag NP collision data, respectively). (B) Equivalent spherical diameters of Ag NP's were estimated using the 2D projection method on TEM data, as described in Appendix 3.5. (n = 67, 63, 85, 83, 66 for 30, 40, 60, 80, 100 nm TEM data, respectively.) We chose to plot the KDE of each distribution to clearly show the leading and trailing tails of each population, rather than forcing a symmetrical Gaussian fit. The maximum point of each KDE distribution is labeled. Example representative NP collision traces for each population are shown in Appendix 3.7.

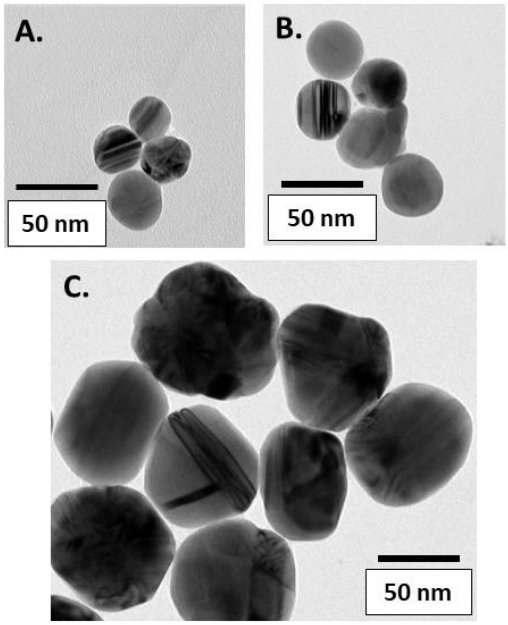

Figure 3.6. Representative TEM Images of Quasi-Spherical Ag NP Sample Populations.

Samples include 30 nm (A), 40 nm (B), and 80 nm (C) populations, as purchased from the commerical supplier. Irregularity in the form of facets and non-sphericity appears to increase with particle size. Images are scaled to the same scale bar length to better compare particle geometry. Additional representative TEM images for other NP sizes are shown in Appendix 3.6.

Appendix 3.1

Python Program for Data Analysis

The accurate quantitation of integrated charge to calculate the equivalent spherical diameter for each Ag NP collision peak is dependent on selecting an accurate baseline. Methods utilizing manual baseline selection risk introducing systematic errors or selection bias towards anticipated results. We instead designed a custom Python script that programmatically adjusts the baseline to zero and extracts peak parameters including amplitude, duration, and area under the curve (integrated charge).

The script assumes a flat, elevated baseline containing positive-going peaks. We first used 3rd order polynomial curve-fitting to adjust the baseline to approximately zero on 30-second sections of the trace. The index of each peak max were then identified, and more rigorous baseline adjustment was performed with linear curve-fitting. Here, 500 points 10 ms before the peak were averaged, and separately 500 points 50 ms after the peak were averaged (where each point is recorded every 10 μs). The resulting 2 averages were linearly fit and adjusted to zero, thus ensuring a precisely zero baseline. Results were then checked by manual inspection and clear examples of non-zero baselines were rejected. All peaks with heights exceeding 3x the peak-to-peak noise of the trace were quantified.

Appendix 3.2

Stock and Diluted NP Concentrations

All NP collision experiments were prepared by adding 300 µL of stock Ag NPs to the 5 mL total volume. We provide each stock and diluted Ag NP concentration in the table below.

NP Diameter (nm)	Stock NP Concentration (Particles/mL)	Diluted NP Concentration (pM)
30	1.60×10^{11}	159.40
40	5.70×10^{10}	56.80
60	1.90×10^{10}	18.90
80	1.10×10^{10}	7.57
100	7.60×10^{9}	4.28

Appendix 3.3

Optimization of Alkaline Thiosulfate NP Collision Condition

The polysulfide-modified thiosulfate condition used in the main text contained 10 mM $Na_2S_2O_3$ 10 mM NaOH in the bulk solution. We selected this condition by systematically varying both the $Na_2S_2O_3$ and NaOH concentrations. Representative traces and respective data analyses are shown below.

The use of less than 10 mM $Na_2S_2O_3$ consistently delayed the onset of collision events by over 5 minutes. See the 6 mM $Na_2S_2O_3$ 10 mM NaOH trace below as a representative example. However, use of more than 10 mM $Na_2S_2O_3$ significantly increased the rate of aggregation, obscuring the single particle collision results. See the rapid decrease in collision frequency in the 15 mM $Na_2S_2O_3$ 10 mM NaOH trace and broadening of the calculated diameter distribution for evidence.

We wanted to keep the pH of the solution above the pKa of thiosulfate (11.35) to promote better complexation with Ag^+. However, increasing the NaOH concentration above 10 mM led to noticeable aggregation, evidenced in decrease in collision frequency in the 10 mM $Na_2S_2O_3$ 20 mM NaOH trace, and broadening of the calculated diameter distribution below. Thus, the selected 10 mM $Na_2S_2O_3$ 10 mM NaOH provided the best tradeoff by maintaining the appropriate pH and avoiding significant aggregation within a 30-minute recording period.

All traces below were recorded using 19 pM 60 nm Ag NP's, and with the polysulfide-pretreatment pulse methodology prepared in their respective solutions. For the distributions, n = 654, 1943, and 337, for the 6 mM, 10 mM, 15 mM $Na_2S_2O_3$ in 10 mM NaOH, and n = 413 for the

10 mM $Na_2S_2O_3$ 20 mM NaOH. We chose to plot the KDE instead of a gaussian fit to better show the broadened distribution shapes.

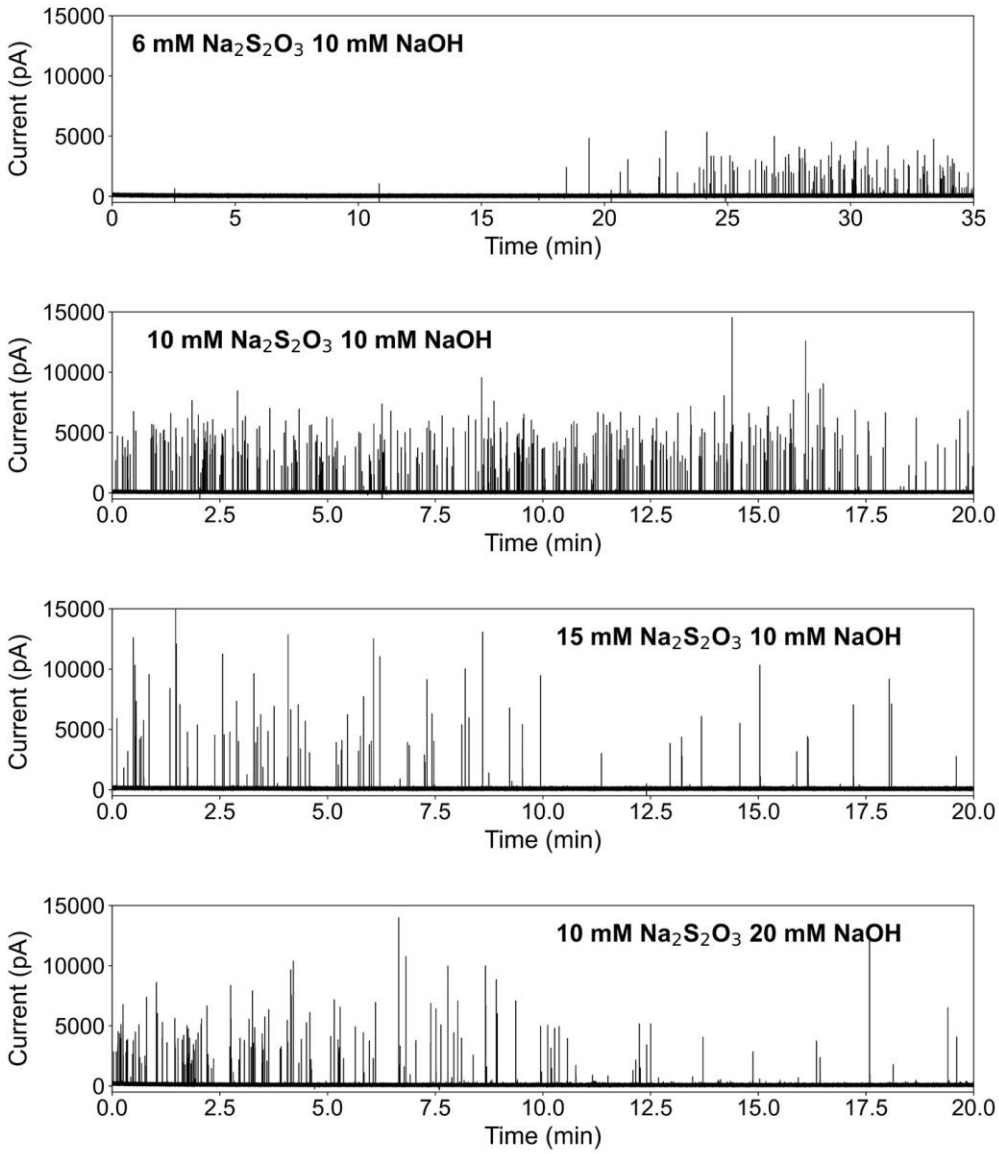

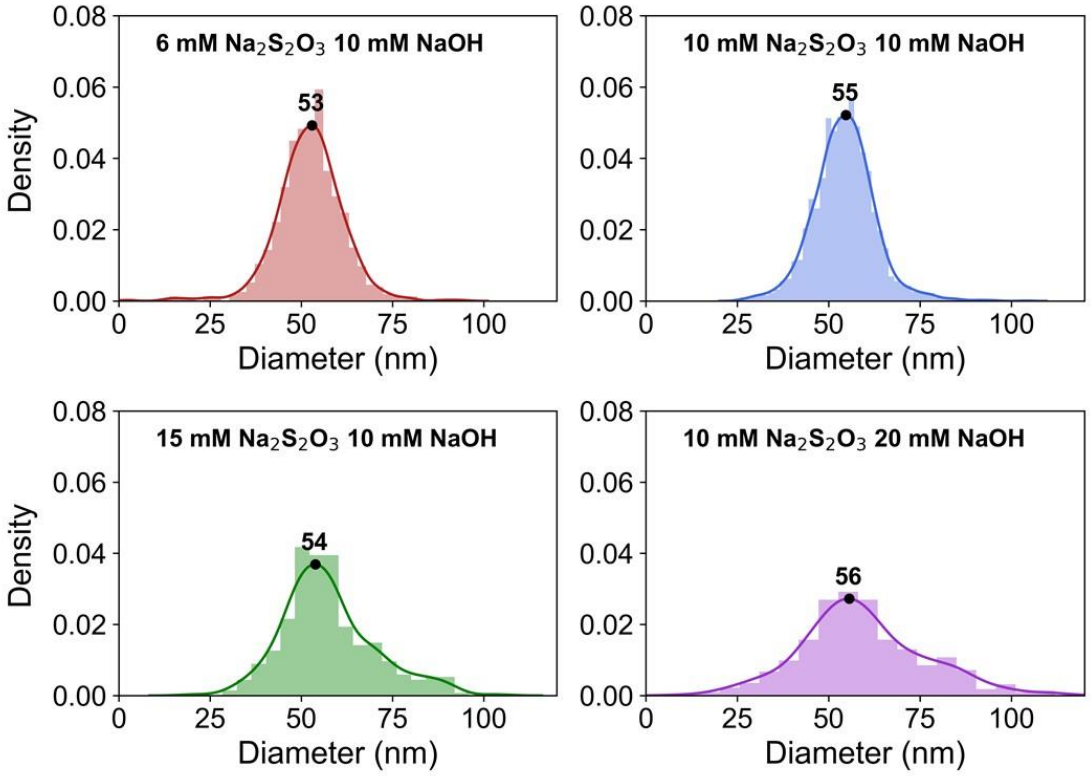
6 mM $Na_2S_2O_3$ 10 mM NaOH
53
10 mM $Na_2S_2O_3$ 10 mM NaOH
55
15 mM $Na_2S_2O_3$ 10 mM NaOH
54
10 mM $Na_2S_2O_3$ 20 mM NaOH
56
Density
Diameter (nm)
0.00
0.02
0.04
0.06
0.08
0
25
50
75
100

Appendix 3.4

Cyclic Voltammetry in Alkaline Thiosulfate

(A.) A cyclic voltammogram sweeping from -0.2 V to 0.6 V to -0.2 V whereby thiosulfate oxidation occurs at ~ 0.35 V followed by electrode passivation. Reduction of the film occurs at -0.2 V, which promotes identical voltammetry dynamics on the subsequent cycles. (B.) If the CV is instead only scanned to a minimum of 0 V, then the large thiosulfate oxidation wave becomes smaller on each successive scan, indicative of electrode passivation.

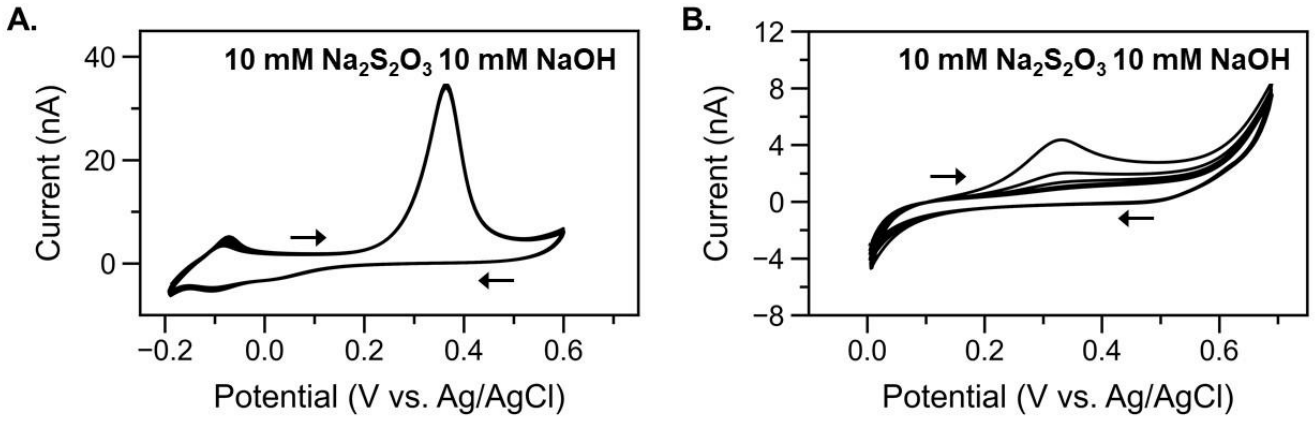

Appendix 3.5

NP Volume Estimation using 2D Projection Method with TEM Data

Here we show the process of using the 2D projection method to analyze TEM data for an 80 nm Ag NP sample. The original image (A) is thresholded using ImageJ in (B), and the area of each object is calculated in (C). The measured area is used to calculate the radius of the equivalent sphere.

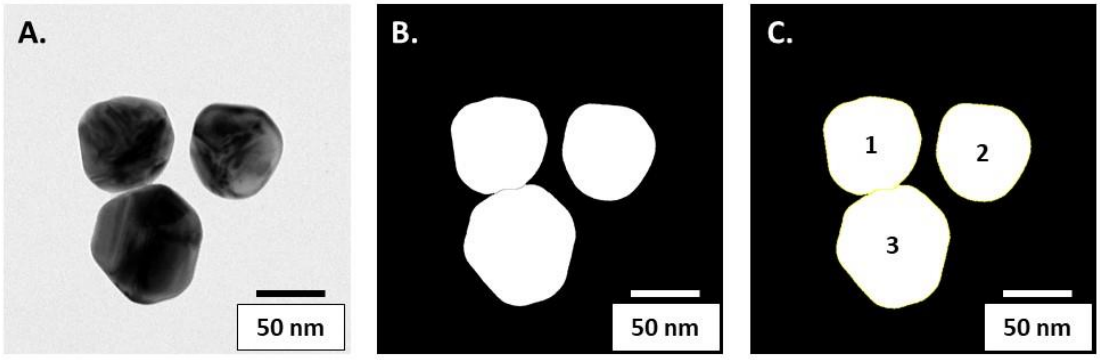

NP #	Measured Area (nm^2)	Equivalent Spherical Radius (nm)	Equivalent Diameter (nm)
1	4043	35.9	71.8
2	3836	35.1	70.2
3	5538	42	84.0

Appendix 3.6

Representative TEM Images for Ag NPs

Images are provided for 30, 40, 60, 80, and 100 nm Ag NP's for A-E, respectively. Images were sized with equivalent scale bars to better illustrate quasi-sphericity of larger NPs.

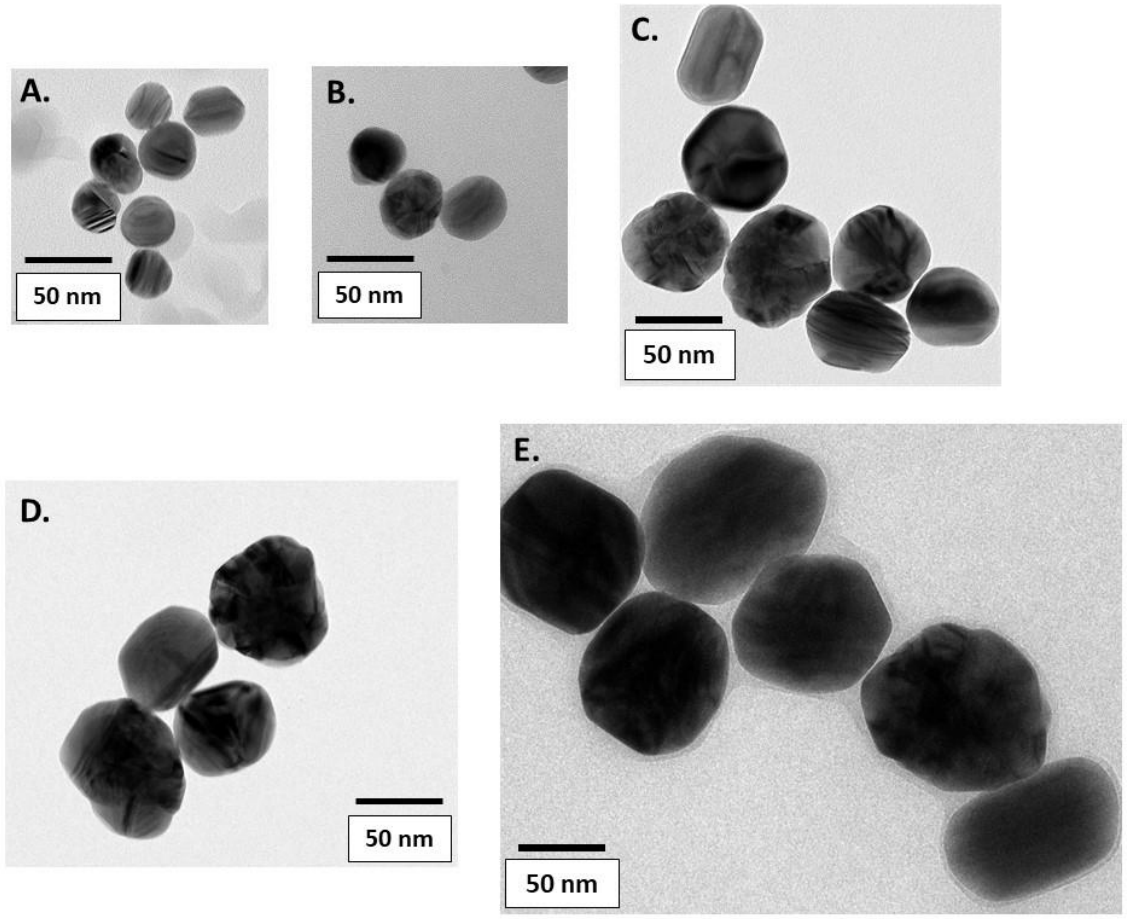

Appendix 3.7

Representative NP Collision Traces for 30, 40, 60, 80, 100 nm Ag NPs

Traces were recorded using the polysulfide-modified Au electrode in 10 mM $Na_2S_2O_3$ 10 mM NaOH with the same diluted NP concentrations as displayed in Appendix 3.2. The equivalent diameter distributions are summarized in Figure 3.5.

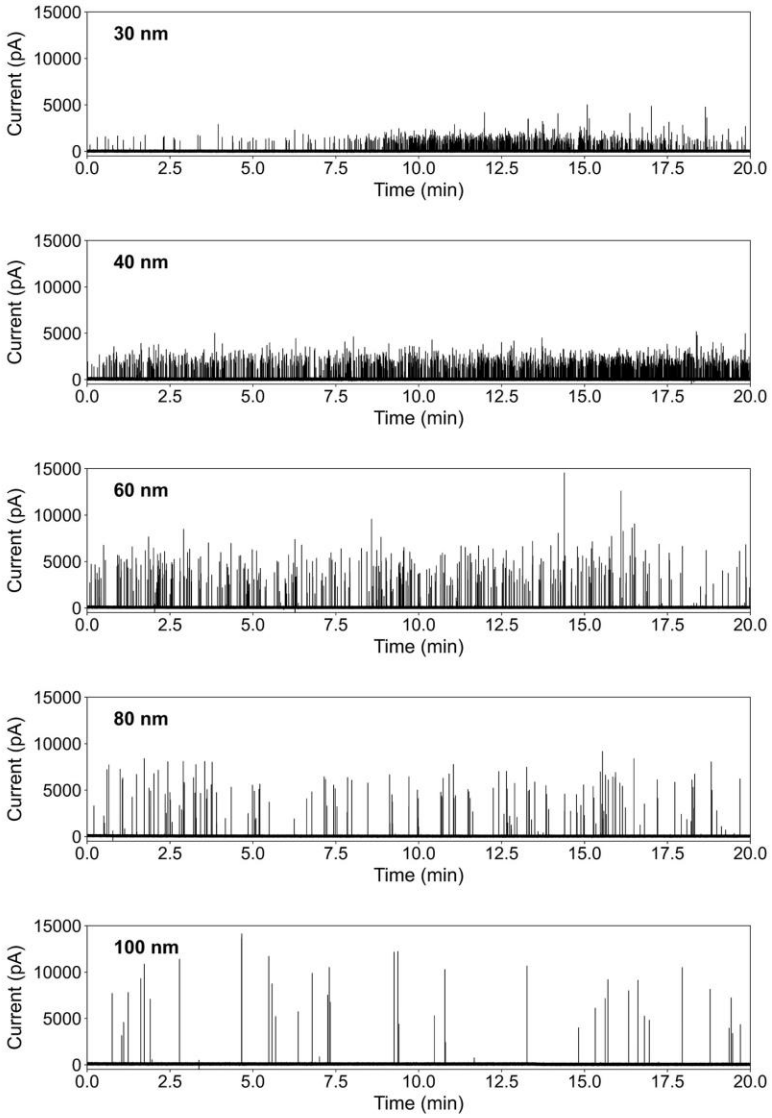

Appendix 3.8

Representative NP Collision Events for 10 mM $Na_2S_2O_3$ 10 mM NaOH with Polysulfide

Note that the y-axis scaling is 2 times that of the axes shown in Appendix 3.9-3.11.

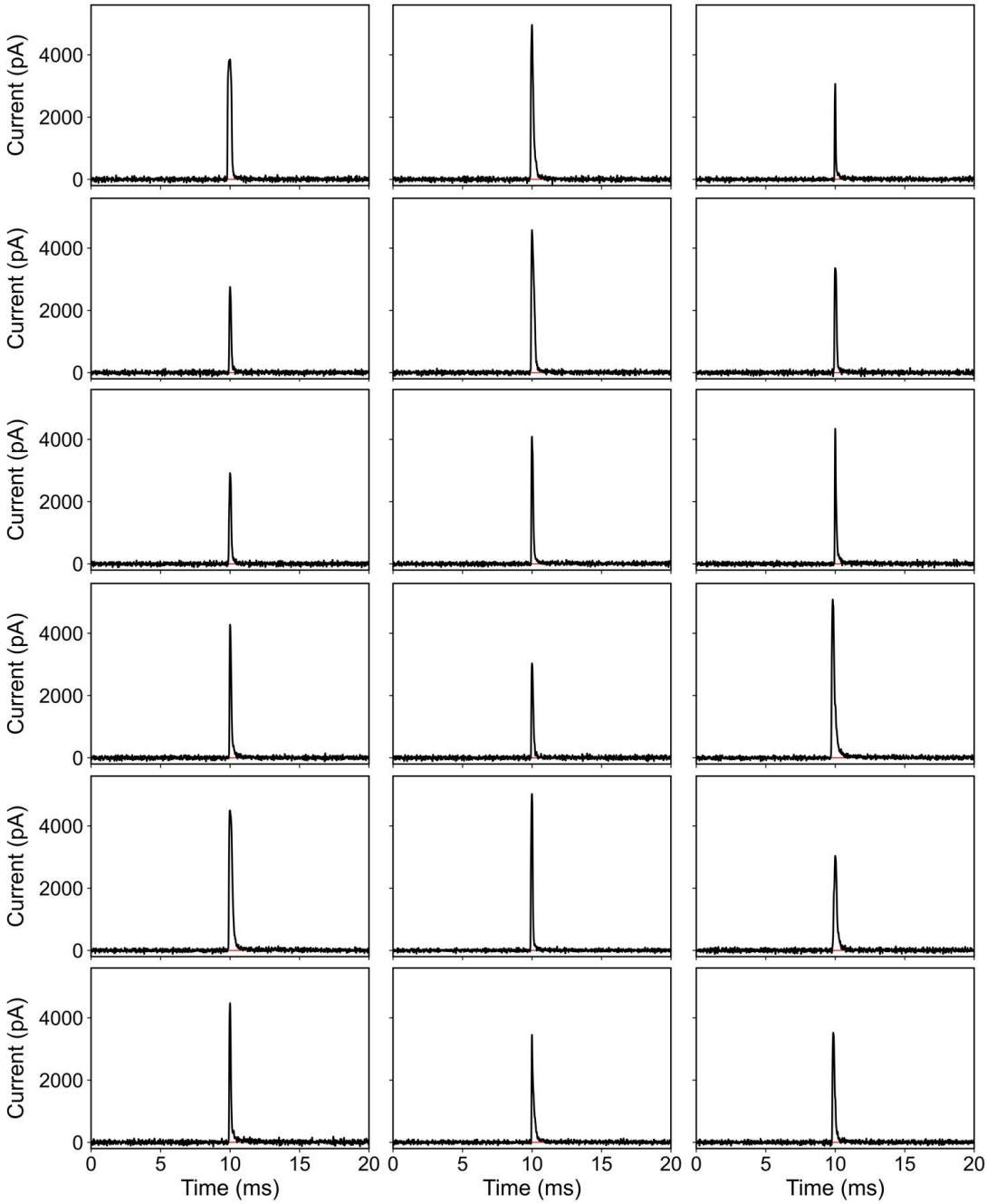

Appendix 3.9

Representative NP Collision Events for 10 mM $Na_2S_2O_3$ 10 mM NaOH without Polysulfide

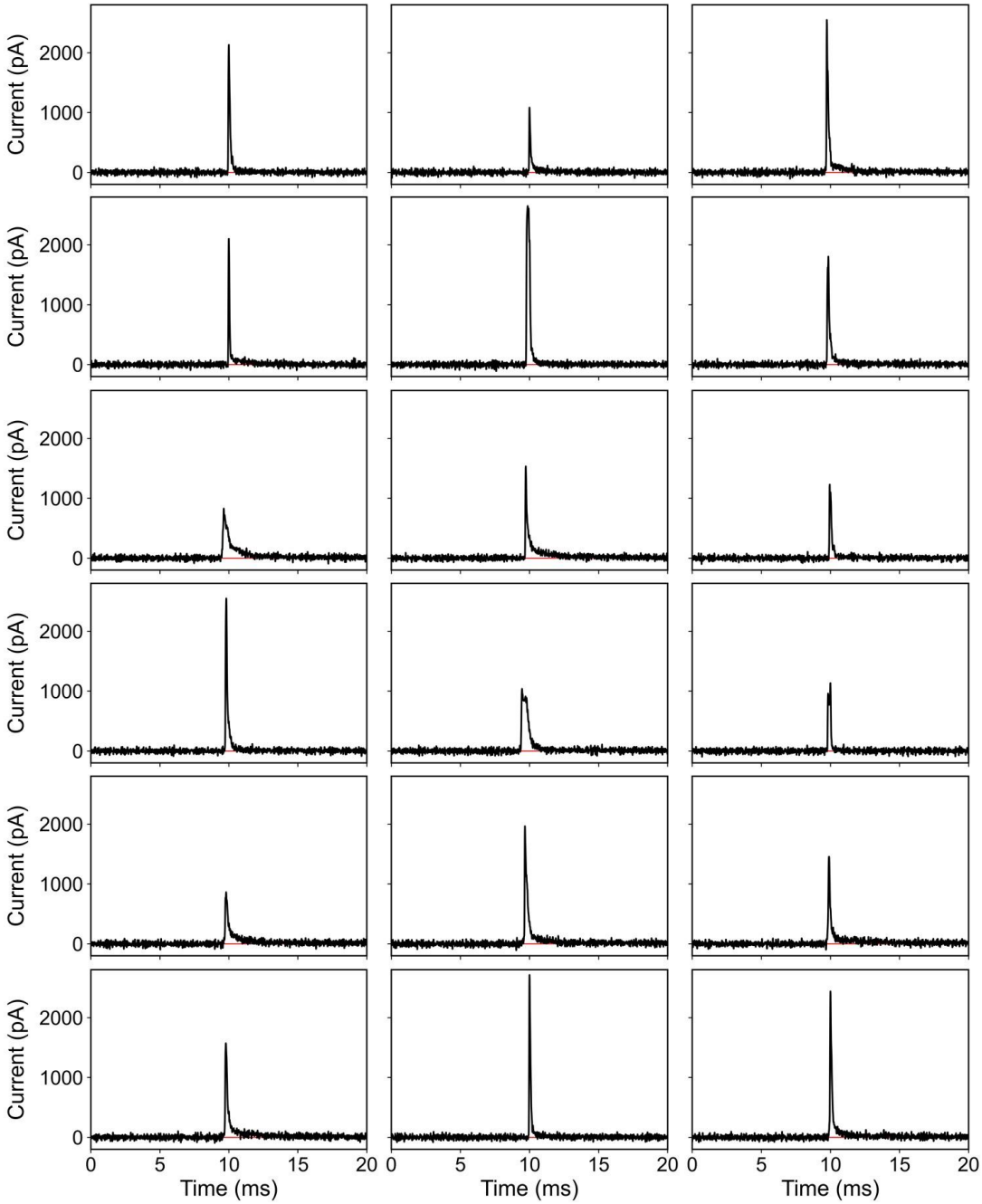

Appendix 3.10

Representative NP Collision Events for 10 mM KCl 10 mM NaOH

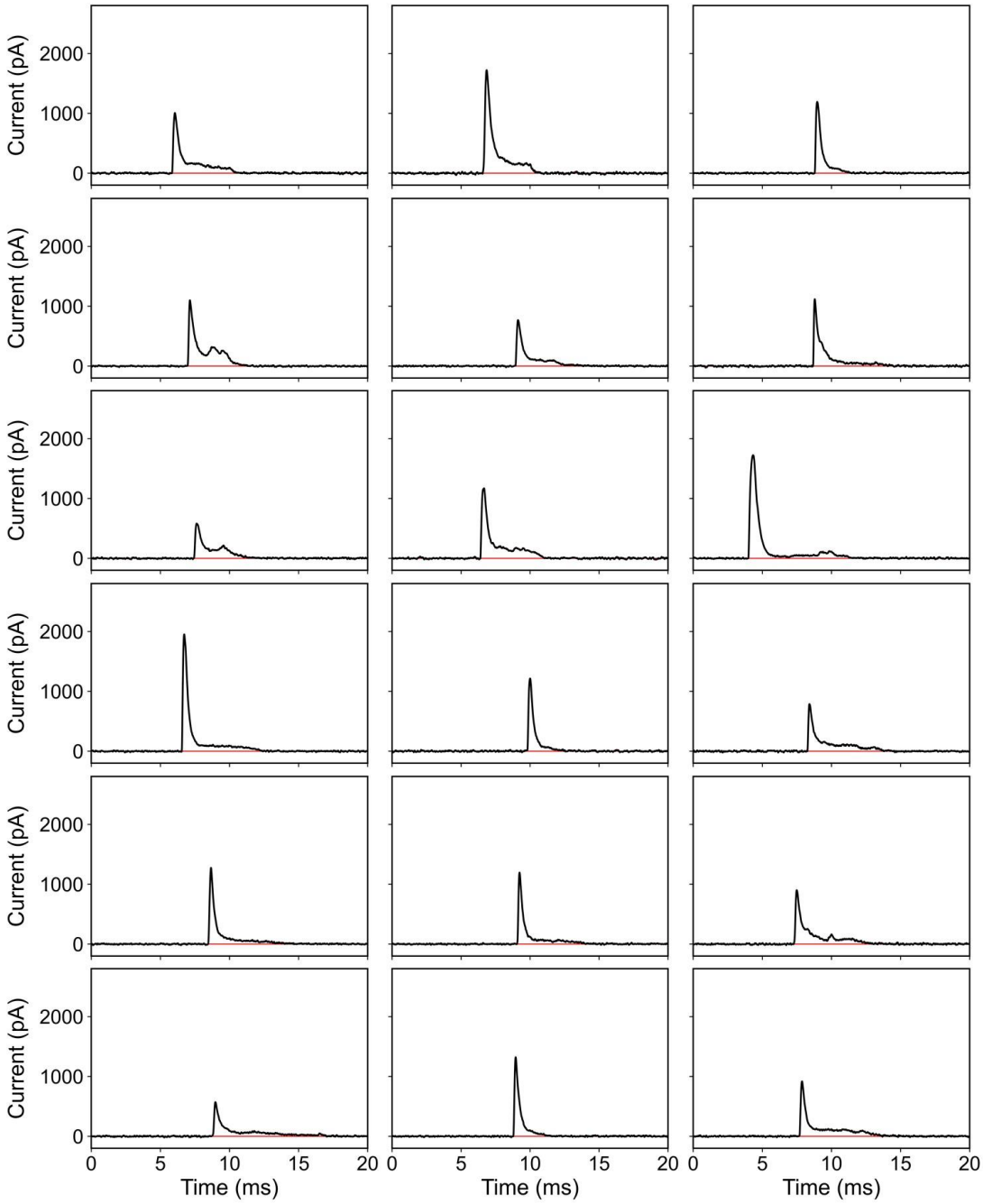

Appendix 3.11

Representative NP Collision Events for 20 mM KCl

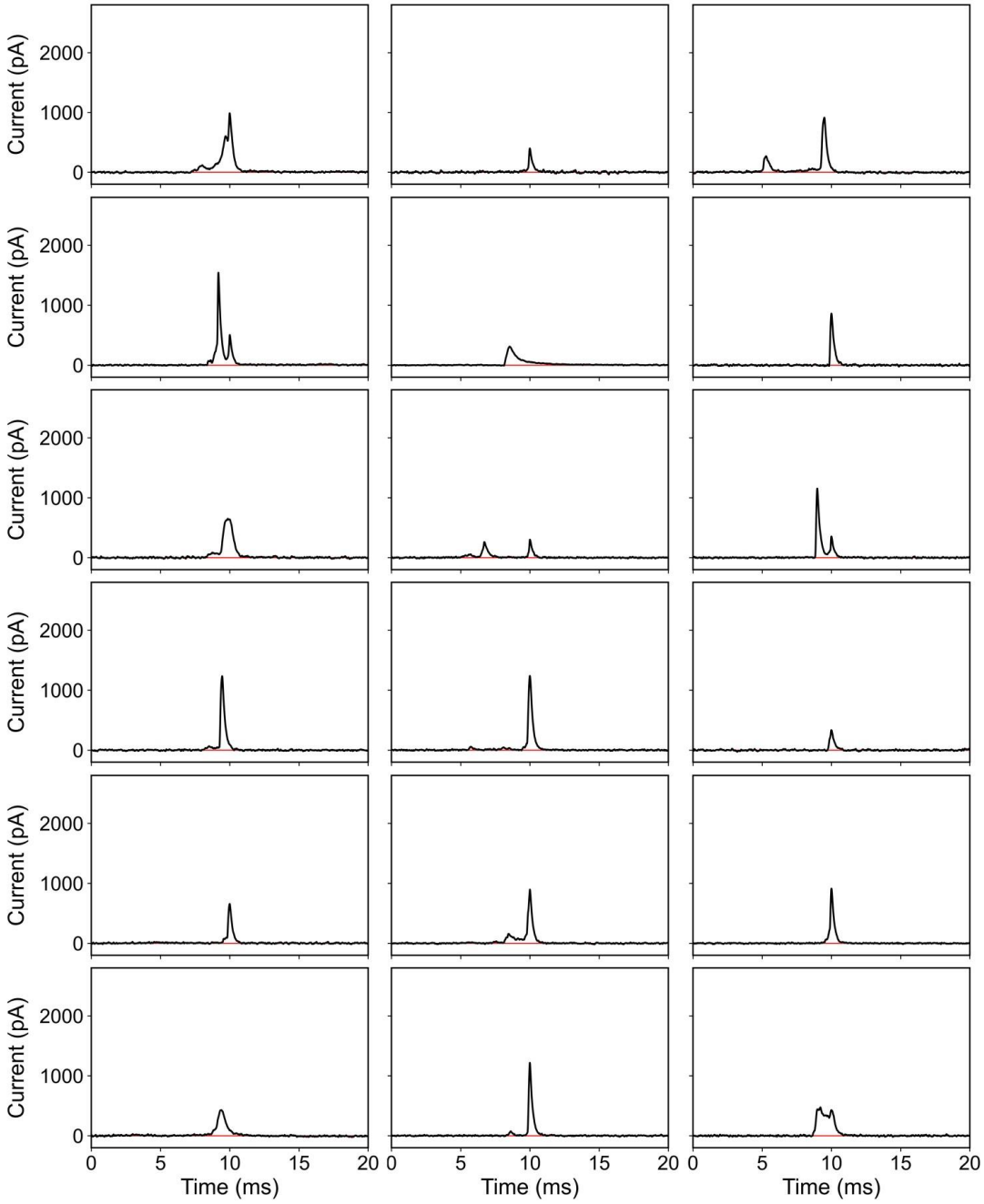

3.6 REFERENCES

(1) Zhang, X. F.; Liu, Z. G.; Shen, W.; Gurunathan, S. Silver Nanoparticles: Synthesis, Characterization, Properties, Applications, and Therapeutic Approaches. *Int. J. Mol. Sci.* **2016**, *17*, 1534.

(2) Iravani, S.; Korbekandi, H.; Mirmohammadi, S. V; Zolfaghari, B. Synthesis of Silver Nanoparticles: Chemical, Physical and Biological Methods. *Res. Pharm. Sci.* **2014**, *9*, 385–406.

(3) Albanese, A.; Tang, P. S.; Chan, W. C. W. The Effect of Nanoparticle Size, Shape, and Surface Chemistry on Biological Systems. *Annu. Rev. Biomed. Eng.* **2012**, *14*, 1–16.

(4) Nel, A.; Xia, T.; Mädler, L.; Li, N. Toxic Potential of Materials at the Nanolevel. *Science (80-.).* **2006**, *311*, 622–627.

(5) Little, C. A.; Batchelor-Mcauley, C.; Young, N. P.; Compton, R. G. Shape and Size of Non-Spherical Silver Nanoparticles: Implications for Calculating Nanoparticle Number Concentrations. *Nanoscale* **2018**, *10*, 15943–15947.

(6) Albrecht, W.; Bals, S. Fast Electron Tomography for Nanomaterials. *J. Phys. Chem. C* **2020**, *124*, 27276–27286.

(7) Defnet, P. A.; Anderson, T. J.; Zhang, B. Stochastic Collision Electrochemistry of Single Silver Nanoparticles. *Curr. Opin. Electrochem.* **2020**, *22*, 129–135.

(8) Goines, S.; Dick, J. E. Review—Electrochemistry's Potential to Reach the Ultimate Sensitivity in Measurement Science. *J. Electrochem. Soc.* **2020**, *167* (3), 037505.

(9) Patrice, F. T.; Qiu, K.; Ying, Y.; Long, Y. Single Nanoparticle Electrochemistry. *Annu. Rev. Anal. Chem.* **2019**, *12*, 347–370.

(10) Zhou, Y. G.; Rees, N. V.; Compton, R. G. The Electrochemical Detection and Characterization of Silver Nanoparticles in Aqueous Solution. *Angew. Chemie - Int. Ed.* **2011**, *50*, 4219–4221.

(11) Sokolov, S. V.; Eloul, S.; Katelhon, E.; Batchelor-Mcauley, C.; Compton, R. G. Electrode – Particle Impacts : A Users Guide. *Phys. Chem. Chem. Phys.* **2017**, *19*, 28–43.

(12) Karimi, A.; Hayat, A.; Andreescu, S. Biomolecular Detection at SsDNA-Conjugated Nanoparticles by Nano-Impact Electrochemistry. *Biosens. Bioelectron.* **2017**, *87*, 501–507.

(13) Ma, W.; Ma, H.; Chen, J. F.; Peng, Y. Y.; Yang, Z. Y.; Wang, H. F.; Ying, Y. L.; Tian, H.; Long, Y. T. Tracking Motion Trajectories of Individual Nanoparticles Using Time-Resolved Current Traces. *Chem. Sci.* **2017**, *8* (3), 1854–1861.

(14) Oja, S. M.; Robinson, D. A.; Vitti, N. J.; Edwards, M. A.; Liu, Y.; White, H. S.; Zhang, B. Observation of Multipeak Collision Behavior during the Electro-Oxidation of Single Ag Nanoparticles. *J. Am. Chem. Soc.* **2017**, *139*, 708–718.

(15) Ustarroz, J.; Kang, M.; Bullions, E.; Unwin, P. R. Impact and Oxidation of Single Silver Nanoparticles at Electrode Surfaces: One Shot versus Multiple Events. *Chem. Sci.* **2017**, *8* (3), 1841–1853.

(16) Robinson, D. A.; Liu, Y.; Edwards, M. A.; Vitti, N. J.; Oja, S. M.; Zhang, B.; White, H. S. Collision Dynamics During the Electrooxidation of Individual Silver Nanoparticles. *J. Am. Chem. Soc.* **2017**, *139*, 16923–16931.

(17) Sun, L.; Wang, W.; Chen, H. Y. Dynamic Nanoparticle-Substrate Contacts Regulate Multi-Peak Behavior of Single Silver Nanoparticle Collisions. *ChemElectroChem* **2018**, *5*, 2995–2999.

(18) Ma, H.; Chen, J. F.; Wang, H. F.; Hu, P. J.; Ma, W.; Long, Y. T. Exploring Dynamic Interactions of Single Nanoparticles at Interfaces for Surface-Confined Electrochemical Behavior and Size Measurement. *Nat. Commun.* **2020**, *11*, 1–9.

(19) Hafez, M. E.; Ma, H.; Peng, Y.; Ma, W.; Long, Y. Correlated Anodic–Cathodic Nanocollision Events Reveal Redox Behaviors of Single Silver Nanoparticles. *J. Phys. Chem. Lett.* **2019**, *10*, 3276–3281.

(20) Zelinsky, A. G. RDE Study of Thiosulfate Oxidation on Gold. *J. Electroanal. Chem.* **2014**, *735*, 111–114.

(21) Krause, K. J.; Adly, N.; Yakushenko, A.; Schnitker, J.; Mayer, D.; Offenhäusser, A.; Wolfrum, B. Influence of Self-Assembled Alkanethiol Monolayers on Stochastic Amperometric On-Chip Detection of Silver Nanoparticles. *Anal. Chem.* **2016**, *88* (7), 3632–3637.

(22) Vericat, C.; Vela, M. E.; Benitez, G.; Carro, P.; Salvarezza, R. C. Self-Assembled Monolayers of Thiols and Dithiols on Gold: New Challenges for a Well-Known System. *Chem. Soc. Rev.* **2010**, *39* (5), 1805–1834.

(23) Chaki, N. K.; Vijayamohanan, K. Self-Assembled Monolayers as a Tunable Platform for Biosensor Applications. *Biosens. Bioelectron.* **2002**, *17* (1–2), 1–12.

(24) Bell, R. A.; Kramer, J. R. Structural Chemistry and Geochemistry of Silver-Sulfur Compounds: Critical Review. *Environ. Toxicol. Chem.* **1999**, *18* (1), 9–22.

(25) Pakiari, A. H.; Jamshidi, Z. Nature and Strength of MS Bonds (M = Au, Ag, and Cu) in Binary Alloy Gold Clusters. *J. Phys. Chem. A* **2010**, *114* (34), 9212–9221.

(26) Robinson, D. A.; White, H. S. Electrochemical Synthesis of Individual Core@Shell and Hollow Ag/Ag2S Nanoparticles. *Nano Lett.* **2019**, *19* (8), 5612–5619.

(27) Woods, R.; Hope, G. A.; Watling, K. M.; Jeffrey, M. I. A Spectroelectrochemical Study of Surface Species Formed in the Gold/Thiosulfate System. *J. Electrochem. Soc.* **2006**, *153* (7), D105.

(28) Gao, X.; Zhang, Y.; Weaver, M. J. Adsorption and Electrooxidative Pathways for Sulfide on Gold As Probed by Real-Time Surface-Enhanced Raman Spectroscopy. *Langmuir* **1992**, *8*, 668–672.

(29) Zelinsky, A. G. Anode Current on Gold in Mixed Thiosulfate-Sulfite Electrolytes. *Electrochim. Acta* **2015**, *154*, 315–320.

(30) Lay, M. D.; Varazo, K.; Stickney, J. L. Formation of Sulfur Atomic Layers on Gold from Aqueous Solutions of Sulfide and Thiosulfate: Studies Using EC-STM, UHV-EC, and TLEC. *Langmuir* **2003**, *19* (20), 8416–8427.

(31) Pedraza, A. M.; Villegas, I.; Freund, P. L.; Chornik, B. Electro-Oxidation of Thiosulphate Ion on Gold. Study by Means of Cyclic Voltammetry and Auger Electron Spectroscopy. *J. Electroanal. Chem.* **1988**, *250* (2), 443–449.

(32) Jiang, W.; Wei, W.; Yuan, T.; Liu, S.; Niu, B.; Wang, H.; Wang, W. Tracking the Optical Mass Centroid of Single Electroactive Nanoparticles Reveals the Electrochemically Inactive Zone. *Chem. Sci.* **2021**.

(33) Wei, W.; Yuan, T.; Jiang, W.; Gao, J.; Chen, H.-Y.; Wang, W. Accessing the Electrochemical Activity of Single Nanoparticles by Eliminating the Heterogeneous Electrical Contacts. *J. Am. Chem. Soc.* **2020**, *142*, 14307–14313.

(34) Ngamchuea, K.; Clark, R. O. D.; Sokolov, S. V; Young, N. P.; Batchelor-Mcauley, C.; Compton, R. G. Single Oxidative Collision Events of Silver Nanoparticles : Understanding the Rate-Determining Chemistry. *Chem. Eur. J.* **2017**, *23*, 16085–16096.

(35) Sauls, F. C. A Simple Determination of the Ag2O Solubility Product by Potentiometric Determinations of Both Ag^+ and OH^-. *J. Chem. Educ.* **2013**, *90* (9), 1212–1214.

(36) Attota, R. K.; Liu, E. C. Volume Determination of Irregularly-Shaped Quasi-Spherical Nanoparticles. *Anal. Bioanal. Chem.* **2016**, *408* (28), 7897–7903.

(37) Van Doren, E. A. F.; De Temmerman, P. J. R. H.; Francisco, M. A. D.; Mast, J. Determination of the Volume-Specific Surface Area by Using Transmission Electron Tomography for Characterization and Definition of Nanomaterials. *J. Nanobiotechnology* **2011**, *9* (1), 17.

(38) Patel, A. N.; Martinez-marrades, A.; Brasiliense, V.; Koshelev, D.; Besbes, M.; Kuszelewicz, R.; Combellas, C.; Tessier, G.; Kanoufi, F. Deciphering the Elementary Steps of Transport-Reaction Processes at Individual Ag Nanoparticles by 3D Superlocalization Microscopy. *Nano Lett.* **2015**, *15*, 6454–6463.

(39) Sundaresan, V.; Monaghan, J. W.; Willets, K. A. Monitoring Simultaneous Electrochemical Reactions with Single Particle Imaging. *ChemElectroChem* **2018**, *5*, 3052–3058.

Chapter 4. DETECTION OF TRANSIENT NANOPARTICLE COLLISION USING ELECTROCHEMILUMINESCENCE ON A CLOSED-BIPOLAR MICROELECTRODE*

4.1 INTRODUCTION

Bipolar electrochemistry has been extensively studied over the past decade with diverse applications in topics including sensor development[1,2], electrocatalyst screening[3,4], asymmetric materials fabrication[5,6], fundamental studies[7–11], and many others.[12–14] A conventional open bipolar electrochemical cell contains a conductive material, i.e., a bipolar electrode (BPE), immersed in an ionic solution, where potential is wirelessly driven to couple complementary redox half reactions at opposite electrode poles. If a given half-reaction generates light, such as in electrogenerated chemiluminescence (ECL) or redox-mediated fluorescence, then the electrochemical dynamics of the complementary half reaction can be optically monitored.[15–23]

A closed bipolar electrode (c-BPE), on the other hand, connects two separate solutions with its two poles. Massive parallel arrays containing tens to hundreds of thousands c-BPEs can be used and simultaneously monitored using ECL or fluorescence.[24–28] Their utilization has become a unique strategy for monitoring large-scale heterogeneous electron-transfer events. When redox-generated light is used to measure the faradaic response, each electrode in a large array serves as an equivalent optical pixel for wide-scale spatial resolution of electrochemical processes. Reported applications include catalytic screening,[27,29] and detection of cancer biomarkers.[30]

Despite excellent progress, a key c-BPE application missing from literature is in use of optical detection to image transient electrochemical events. Our group has been particularly interested in developing large arrays of c-BPEs to optically monitor very fast and transient redox

---

* This chapter is adapted with permission from:
Defnet, P. A.; Zhang, B. Detection of Transient Nanoparticle Collision Events Using Electrochemiluminescence on a Closed Bipolar Microelectrode. *ChemElectroChem* **2020**, *7*, 252–259. Copyright (2020) Wiley.

events, such as release of neurotransmitter molecules from single cells as a tool for fundamental biological study.[27] While neurotransmitter release has traditionally been measured from biological species using single microelectrode probes, or with directly-connected arrays with small electrode counts,[31] the closed-bipolar array imaging methodology would instead allow the capacity to measure from thousands of parallelized electrodes simultaneously given the wireless design and optical readout. However, the optical measurement of these transient processes is a challenging analytical task because an average dopamine release event from chromaffin cells can last from 20-200 ms and give 1.19 ± 0.08 pC in transferred charge when measured using a carbon-fiber microelectrode (CFE).[32] The resolution of fast redox events is challenged by the small amount of charge generated in the faradaic process, which translates to a very small number of photons to be expected from the other pole of the same BPE if ECL is used as the optical readout mechanism. Moreover, although one can use fast frame rates to more accurately resolve a peak, the number of photons one can collect in each fame would also proportionally decrease leading to difficulties in resolving the signal from the noise.

As a first step toward imaging transient neurochemical signals on large arrays, we therefore sought to use a well-characterized c-BPE system to explore the optical detection of transient electrochemical events. We used a pair of CFEs connected in series as our c-BPE system to measure transient collisions of Pt nanoparticles. A small potential bias was applied across the BPE such as the nanoparticle collision event can be electrocatalytically amplified by the hydrogen evolution reaction (HER), which is coupled to the anodic ECL reactions of $Ru(bpy)_3^{2+}$/2-(dibutylamino)ethanol (DBAE). To better control nanoparticle delivery onto the CFE surface in an acidic solution, we used our group's previously developed pressure-driven microjet collision system.[33] A highly-reproducible two-part transient signal was obtained for each particle collision

event according to the known two-step HER mechanism.[33] The signal consisted of a short current spike (<150 μs wide) due to ultrafast hydrogen adsorption on Pt, followed by a ~400 ms current decay due to HER and particle deactivation. The use of an ECL process on the anodic pole allowed us to collect an optical signal for each collision.[34] Correlated amperometric (*i*-*t*) and ECL (*count*-*t*) traces were compared to determine the quantitative accuracy of the transient optical recording. Evaluating the correlation of ECL and amperometric signals was necessary since only the optical response is detectable from individual electrodes when the methodology is applied across a wireless closed-bipolar array.

To the best of our knowledge, this is the first time that nanoparticle collision has been used in a bipolar electrochemistry system to characterize its imaging performance for transient redox processes. Previous BPE-based imaging applications have mainly focused on long-timescale and steady-state measurements.[24,26,30] Although ECL and fluorescence have been used to study nanoparticle collision, light was not generated across a closed-bipolar electrode. Instead, the optical signal was produced directly from the particle itself. For example, Ma et al. have studied the collisions of ECL-active $Ru(bpy)_3^{2+}$-doped silica nanoparticles generating ECL signal upon electrode collision;[35] and our group has studied collision of silver nanoparticles in a Pt nanocell by measuring fluorescent signal from the silver nanoclusters produced during collision.[36]

The success of this work demonstrates the capacity to study many exciting applications for the wide-field imaging of transient redox processes while using massive arrays of closed-bipolar electrodes. Examples include the monitoring of neurotransmitter release from single cells or brain slices, as well as massively parallelized single nanoparticle collision or single vesicle redox quantification.

4.2 Experimental Section

4.2.1 *Chemicals*

Tris(2,2'-bipyridyl)dichlororuthenium(II) hexahydrate $Ru(bpy)_3^{2+}$, 2-(dibutylamino) ethanol (DBAE, 99%), perchloric acid ($HClO_4$, 70%), and ferrocenemethanol (FcMeOH, 97%) were purchased from Sigma-Aldrich. Sodium perchlorate monohydrate ($NaClO_4 \cdot H_2O$, >99%), and potassium chloride (KCl, >99%) were purchased from Fluka. Citrated-capped Pt nanoparticles with diameter 70 ± 4 nm dispersed in 4 mM sodium citrate were purchased from NanoComposix. All chemicals were used as received from their manufacturers. Solutions were prepared with 18.2 MΩ cm^{-1} deionized water obtained from a Barnstead NANOpure water purification system (Thermo Scientific). The ECL solution consisted of 25 mM $Ru(bpy)_3^{2+}$, 20 mM DBAE, and 100 mM pH 7.4 phosphate buffer. The microjet collision bulk acid solution consisted of 100 mM $HClO_4$ and 100 mM $NaClO_4$.

4.2.2 *Electrode Fabrication*

The carbon fiber electrodes used for Pt nanoparticle microjet collision experiments were fabricated according to a procedure previously reported by our group.[33] A single 5 μm diameter carbon fiber (Besfight G40-800) was aspirated into a borosilicate glass capillary tube (1.2 mm O.D./0.69 mm I.D., Sutter). A Sutter P-97 micropipette puller with a 3.0 mm square box filament (2.0 mm wide; Sutter, FB320B) was used to pull the capillary into 2 separate tips. The following 1-line program was used: heat = ramp+10, pull = 150, velocity = 75, time = 250. Excess carbon fiber protruding from the tip was trimmed with a stainless-steel surgical scalpel. The tips were dipped in epoxy (Epo-Tek 301) for 10 minutes, placed in an 80° C oven for 2 hours, and then placed in a 150° C oven for 2 hours to ensure full curing. A 250 μm diameter tungsten wire was

dipped in silver paste epoxy (Dupont), and used to make contact to the posterior carbon fiber inside the capillary. Epoxy (Hysol 0151) was used to secure the tungsten wire to the end of the capillary. Electrode tips were beveled at a 45° angle using a home-built microelectrode beveller.

The ECL reporting electrodes were fabricated by sealing a 5 μm carbon fiber in glass using a heating coil, like previously reported fabrication schemes for Au microelectrodes.[37] A single 5 μm diameter carbon fiber (Besfight G40-800) was aspirated into a borosilicate glass capillary tube (1.2 mm O.D./0.69 mm I.D., Sutter). One end of the capillary was sealed shut using a Bunsen burner. A vacuum line was connected to the open end of the tube, and the fiber was sealed using of a heating coil. Care was taken to avoid bubble formation around the fiber. The 5 μm disk was exposed by sanding with P60 and P-220 grade sandpaper. A 250 μm diameter tungsten wire was dipped in silver paste epoxy (Dupont), and used to make contact to the posterior carbon fiber inside the capillary. Epoxy (Hysol 0151) was used to secure the tungsten wire to the end of the capillary.

The 50 μm Pt ultramicroelectrode (UME) was fabricated for use in Figure 4.2 according to an almost identical procedure as the glass-sealed ECL reporting electrode. The only variations included the use of a 50 μm Pt wire instead of the 5 μm carbon fiber and by sealing it inside a larger borosilicate glass capillary tube (1.5 mm O.D./0.86 mm I.D., Sutter).

All electrodes were characterized using cyclic voltammetry in 1 mM FcMeOH and 100 mM KCl. A fresh electrode surface was exposed prior to every experiment by beveling the microjet electrodes and sanding the carbon-fiber and Pt electrodes with P220 grade sandpaper.

4.2.3 *Micropipette Fabrication*

Glass micropipettes approximately 5 μm in diameter were used to inject nanoparticles in the microjet collision system. Micropipettes were prepared by pulling borosilicate glass capillary tubes (1.0 mm O.D./0.5 mm I.D., with filament; Sutter, BF100-50-10) on a P-97 micropipette

puller using a 3.0 mm square box filament (2.0 mm wide; Sutter, FB320B). The following two-line program was used: heat = ramp value, pull = 0, velocity = 30, time = 250; heat = ramp + 10, pull = 70, velocity = 30, time =250. A stainless-steel surgical scalpel blade was used to cut the pipette orifice to the desired size. Orifice diameters were estimated using a microscope eyepiece ruler.

4.2.4 *ECL Measurements of Nanoparticle Collision*

Two inverted microscopes (Olympus IX70, and Olympus IX71) were positioned side by side on a vibration isolation table and inside of a grounded faraday cage. One microscope (IX71) was used to align the microjet collision experiment, and the other (IX70) was used to collect the generated ECL signal. See Figure 4.1 for a diagram of the experiment. The closed bipolar electrode was formed by electrically connecting the microjet and ECL working electrodes in their separate solutions with an insulated Cu wire.

4.2.5 *Microjet Collision Setup*

The microjet setup was identical to our procedure previously reported.[33] A glass micropipette was back-filled with stock 70 nm Pt NP solution and connected to a Femtojet microinjector (Eppendorf). Its position was controlled with an analog micro-positioner. A separate micro-positioner was used to control the movement of the 5 μm beveled carbon fiber detecting electrode. The pipette orifice and electrode tip were submerged in bulk acid solution (100 mM $HClO_4$ and 100 mM $NaClO_4$) and positioned directly opposite each other while using a 20x (0.4 NA Olympus LCPlanFl) objective. An approximate 10 μm distance was maintained for consistent data collection. The microjet pressure was held at a constant 0.2 psi to maintain a steady collision

frequency. The carbon fiber electrode was biased at a potential in the steady-state region of the HER. Non-bipolar experiments used -850 mV, and bipolar experiments used -1600 mV.

4.2.6 *ECL Setup*

The ECL reporting electrode was submerged in a reservoir of pH 7.4, 50 mM phosphate buffer solution containing 25 mM $Ru(bpy)_3^{2+}$, 20 mM DBAE and was positioned above a glass coverslip using a MP-225 micromanipulator (Sutter Instrument Co.). The optical bipolar ECL signal was collected using a 40x (1.15 NA Uapo-340) water-immersion objective and recorded using an Andor iXon 897E EMCCD camera cooled to -80° C. The pre-amplifier gain was set to 5.1x, the electron multiplier (EM) gain was set to 300, the readout rate was 10 MHz at 14-bit, and the vertical pixel shift speed was set to 0.3 µs. A 24×24 pixel window in isolated crop mode was used to obtain fast exposure times with minimal time between frames. Exposure times, (frame rates) of 0.0002542 s (3786.4 Hz), 0.0004942 s (1932.7 Hz), 0.0009942 s (995.92 Hz), 0.0050042 s (199.44 Hz), 0.0099942 s (99.959 Hz), 0.0499942 s (19.998 Hz), and 0.0999942 s (9.9996 Hz) were used. Andor SOLIS software was used to record all imaging data. Andor SOLIS and ImageJ were used for image processing. All graphs in the manuscript were created using Origin 2019b.

4.2.7 *Electrochemical Recordings*

Potential was applied across all investigated systems using a ChemClamp potentiostat (Dagan Corporation) with an N=1 headstage connected to two Ag/AgCl reference electrodes placed in each solution. The same device also measured the current while sampling at 100 kHz using a 1322A digitizer (Axon Instruments) and filtering at 10 kHz using a hardware low-pass Bessel filter. *I-t* data were recorded using Axoscope 10.0 software (Molecular Devices) and

analyzed in Clampfit 10.7 (Molecular Devices) software. A digital trigger in Axoscope 10.0 was used to ensure that the electrochemical and optical recording started at the same time.

4.2.8 *Curve Fitting*

The decay curves were fit in Figures 4.3g and 4.5g using a weighted exponential function with the following formula:

$$f(t) = K_0(\sum_{i=1}^{n} f_i e^{-K_i t}) + C$$

Where n= 1, K_0 is a scaling factor, f_i is the amplitude of the exponential function, K_i is the inverse of the exponential time constant, t is each time point, and C is an off-set accounting for a non-zero baseline.

Curves were fit starting directly after the hydrogen adsorption spike until they decayed back to the baseline. Correlation values >97% were obtained. The fitting parameters were averaged across 25 events per curve to obtain each averaged trace.

4.2.9 *Nanoparticle Characterization*

The 70 nm Pt nanoparticles were characterized using transmission electron microscopy (TEM) imaging performed on a FEI Technai G2 F20 operating at 200 kV with a single tilt sample holder. The TEM sample was prepared by drop-casting the 70 nm Pt nanoparticles onto carbon-coated Formvar copper TEM grids (Ted Pella, Inc.). Results are shown in Figure 4.11.

4.3 Results and Discussion

4.3.1 *Description of the ECL Imaging System*

We adopted our group's previously reported microjet collision scheme to produce highly reproducible nanoparticle collision events with tunable signal magnitude.[33] By this mechanism, Pt nanoparticles were housed in a glass micropipette, ejected under pressure-driven flow through a highly concentrated bulk solution, and onto a detecting CFE positioned several microns away (as shown in Figure 4.1). Due to the particle's short transit time in the bulk redox solution (from <1 ms to a few ms), particle aggregation is largely avoided, leading to a reproducible HER current signal while using concentrated bulk acid conditions. This contrasts the classical diffusion-limited methods whereby aggregation is observed for citrate-capped nanoparticles in ionic concentrations higher than ~20 mM or a lower pH than 3.13 (pK_a of the citrate capping ligand).[38] By increasing the bulk acid concentration in the microjet system, we correspondingly increase the magnitude of the electrocatalytically amplified signal to generate a more easily detectable transient event consisting of a sharp current spike and a transient current decay. The durations of the ultrafast spike and transient decay are quantified in Figures 4.6 and 4.3g, respectively. The two-part collision signal is desirable since it allows us to investigate two transient events of different durations per collision in the bipolar imaging experiments described herein.

The nanoparticle collision events were coupled to anodic ECL on another CFE electrode, which is connected to the detection CFE to enable correlated optical recording. We selected the $Ru(bpy)_3^{2+}$/2-(dibutylamino)ethanol (DBAE) ECL pair due to reports of comparable sensitivity compared to the traditional $Ru(bpy)_3^{2+}$/tripropylamine (TPrA) system.[34] The ECL sensitivity was further enhanced by increasing the $Ru(bpy)_3^{2+}$ concentration, as shown in Figure 4.7. The curve

appears to asymptotically approach a maximum sensitivity limit, and therefore we used the maximum concentration which was tested (25 mM) for our experiments.

4.3.2 *Electrochemical Characterization of Nanoparticle Collision Events*

We began by determining the appropriate driving potential to apply in our bipolar ECL imaging experiment. Figure 4.2 shows a bipolar CV between a 50 μm diameter Pt ultramicroelectrode (UME) undergoing the HER and a 5 μm CFE as the anodic ECL reporting pole. The Pt UME served as a stable substitute for the transient Pt nanoparticle collision response. Results indicate that the HER current signal reaches a plateau when the applied voltage was below -1.5 V. We therefore chose -1.6 V to ensure we were safely inside the HER steady state diffusion-limited region during the bipolar particle collision experiments.

Figure 4.2 also suggests that the anodic ECL reporting pole is limiting the overall faradaic current passed across the bipolar system, evidenced by the small (40 nA) steady state current. By using a known equation[39] to calculate the predicted steady state limiting current across a 50 μm Pt disk electrode in 25 mM $HClO_4$, we would instead expect 2.24 μA. Here, the overall faradaic current is most significantly limited by the small size of the 5 μm CFE. In the bipolar collision imaging experiment, however, the limiting pole becomes the CFE electrode used for the ECL recordings due to a lower bulk redox concentration, despite differences in electrode size.

Figure 4.3 compares the amperometric nanoparticle collision events recorded in the bipolar setup (in blue), and the non-bipolar, two-electrode setup (in black). The apparatus used in the non-bipolar, two-electrode measurements maintains a similar microjet setup, although simply applies potential between a CFE and a Ag/AgCl reference electrode. Figures 4.3a and 4.3b show representative amperometric traces for the non-bipolar and bipolar collision experiments, respectively. Both setups resulted in clear recording of fast nanoparticle collision events although

the electric noise in the bipolar recording was higher than the two-electrode setup. This higher noise is likely due to the presence of two additional electrode/solution interfaces in a bipolar recording and the increased double layer capacitance and stray capacitance from the electrical wires connecting the two microelectrode poles. The use of two microscopes in the same Faraday cage may have also contributed to the increased noise. Nevertheless, the overall shapes of the nanoparticle collision events are quite similar in both recordings indicating that the use of a bipolar electrode does not significantly alter the amperometric response. To further study the difference between the bipolar and non-bipolar events, we examine each electrochemical process separately, distinguishing between the ultrafast hydrogen adsorption spike and the slower current decay for hydrogen evolution.

An example hydrogen adsorption spike is visible in the insets of Figures 4.3c and 4.3d, which display a single event for the non-bipolar and bipolar peaks, respectively. Initial examination reveals that the ultrafast spike appears smaller in magnitude for the bipolar recording. This observation is confirmed in Figures 4.3e and 4.3f, which quantify the charge for the hydrogen adsorption spike for 150 collisions to be 403 ± 90 fC for bipolar events and 504 ± 133 fC for non-bipolar events. The H-adsorption charge measured in the bipolar recording is ~20% smaller than that in the conventional two-electrode setup, which leads us to believe that the anodic ECL reporting pole is somewhat limiting the amount of current that can pass across the bipolar electrode. We further support this claim by examining Figure 4.3f, which shows that the bipolar charge distribution has a smaller standard deviation than the non-bipolar events. It would make sense that the bipolar events approach a maximum charge, which is likely limited by the diffusion of anodic ECL reagent at the reporting pole.

If we instead examine the hydrogen evolution decay event, preliminary traces in Figures 4.3a, b, c, and d suggest that the bipolar event is narrower in shape. Figure 4.3g confirms this observation by plotting the average fitted decay curve from 25 events of each type. Figure 4.3g shows that bipolar events decay faster and transfer less charge (smaller area under curve) than their non-bipolar counterparts. These results further confirm that the anodic ECL pole is indeed limiting the charge passed through the bipolar system.

The minor deviation observed between the non-bipolar and bipolar events does not impact the quality of the study, since the overall purpose was to investigate the correlation between the optically recorded transient nanoparticle events and the simultaneously recorded electrochemical signal. Rather, it is more important that the bipolar event still maintains the same two-part peak shape consisting of a fast H-adsorption spike and a broader current decay, thereby enabling the study of two types of transient events of different duration per collision from the ECL response. This makes it so that when we investigate the ECL responses, we can still study two transient events of different durations per collision. If in future studies it becomes critical for the bipolar peaks to match with those of the non-bipolar system, then the particle collision pole should be rendered limiting by increasing the redox concentration in the reporting pole.[40]

4.3.3 *Correlating ECL and Amperometric Signals*

In Figure 4.4 we demonstrate our success in utilizing ECL to detect fast collision events of single Pt nanoparticles. Figure 4.4a shows nanoparticle collision events simultaneously recorded by counting the total photon signal from the ECL reporting pole (red, *count-t*) and by recording the amperometric current signal (blue, *i-t*). The *current* trace was used to evaluate the accuracy of the correlated optical signal. The results are promising since a measurable optical signal is detected that mirrors that fast-rise, slow-decay shape of the amperometric peak. In Figure 4.4b we show the

optical images of the reporting pole recorded during a nanoparticle collision event. A distinct difference in ECL intensity is observed between the peak and baseline, indicating that one can use closed bipolar ECL to detect these rapid nanoparticle collision events.

However, we observe some significant temporal differences between the ECL and current signals as we examine correlated ECL and amperometric signals individually (Figure 4.4c). The <150 μs H-adsorption spike is absent in the ECL signal, while the 400 ms hydrogen evolution decay is broadened to more than 600 ms. Figure 4.4c was recorded using a 100 ms exposure time (ET), where the ET can be approximated by 1/FR (FR = frame rate) and is the amount of time that photons are collected per camera frame. The lower temporal resolution is understood given the slow 10 Hz sampling rate relative to the duration of each transient event. However, increasing the optical sampling rate to achieve better temporal resolution complicates the optical measurement by introducing sensitivity restrictions.

The challenge of obtaining equivalent temporal resolution is due to the known mechanistic differences between ECL and current measurements. The faradaic current measured at each time point corresponds to the rate of the redox reaction on the electrode. Therefore, a change in the sampling rate would not change the current magnitude. The ECL signal, however, measures the number of photons collected on the CCD camera in a given exposure time. Because the exposure time is inversely related to the sampling rate, an increase in the sampling rate will thus cause less photons to reach the detector. Therefore, the optical sensitivity (photons/frame) is significantly affected by the frame rate and will decrease when the frame rate is increased. For example, if a constant optical signal is sampled at both 10 Hz and 10 kHz, the 10 kHz signal will collect 1000X less photons in each frame. The use of high optical sampling rates is therefore challenged by this sensitivity restraint.

In Figure 4.5 we explore the impact of the exposure time on the quality of the ECL signal. Figure 4.5a and 4.5b show 30 second traces of simultaneously recorded ECL (red) and amperometric (blue) signals using 5 ms exposure time and 500 μs exposure time, respectively. Additional correlated traces are seen in Figure 4.8 using other exposure times. We observe that a smaller ET predictably decreases the signal-to-noise ratio of the optical trace, as is quantitatively shown in Figure 4.5e. We also show that the relative number of photons per event linearly decreases with smaller ET's by plotting the integrated ECL peaks vs. ET in Figure 4.5f.

In Figure 4.5c, and 4.5d we examine individual correlated peaks to explore the temporal resolution of the ECL nanoparticle collision signal. We observe that the ultrafast (<150 μs) H-adsorption spike is absent from all ECL recordings, even under the fastest 500 μs ET condition used in this study. Our sensitivity restrictions prevented us from sampling faster, evidenced by the inability to resolve any ECL signal at 250 μs exposure time. The lack of resolution can be understood given that a <150 μs spike would be averaged with 350 μs of ECL background to produce a single point above the baseline. We would instead like to employ a 30 μs ET to obtain approximately 5 points per spike. Given that our fastest resolvable ET was at 500 μs, we would require an approximate 17-fold increase in ECL sensitivity to record at this desired rate. Enhancement of ECL sensitivity may be achieved by further increasing the $Ru(bpy)_3^{2+}$ concentration as shown in Figure 4.7, although with expected diminishing returns. Interestingly, specific electrode modifications such as the growth of mesoporous silica,[4142] or adsorption of catalytic nanoparticles encapsulated by amine-terminated dendrimers[43] have also shown significant ECL sensitivity enhancements in literature. We believe the adoption of these strategies would offer the best likelihood of achieving the required sensitivity to resolve such ultrafast events using closed-bipolar ECL.

Figure 4.5g examines slower current decay in hydrogen evolution. We plot the average exponential decay curves fit to 25 ECL signals per ET condition. The bipolar amperometric decay curve from Figure 4.3g is also overlaid for comparison. We compare the decay time of the ECL signal for each overlaid curve relative to the bipolar current signal. Decreasing the exposure time produces a more narrow and accurate decay curve, where 5, 1, and 0.5 ms conditions produce accurate results. The 5 ms condition would best maximize optical sensitivity and still maintain accurate temporal resolution. We confirmed this result by overlaying the correlated traces of Figures 4.5a-d in Figure 4.10 to further show that the ECL decay for 5 ms and 0.5 ms ET matches the amperometric response remarkably well. We therefore demonstrate that use of closed bipolar ECL recording can accurately resolve transient HER current in nanoparticle collision events.

4.4 CONCLUSION

In summary, we have used ECL as an effective optical recording strategy for measuring transient nanoparticle collision events. The use of a closed bipolar electrode allows us to convert the transient amperometric current signal on a detection pole into a luminescence signal on the reporting pole. Despite the challenges in recording the initial ultrafast H-adsorption signal, ECL can be useful in measuring the subsequent ~400 ms transient HER signal on single 70 nm Pt nanoparticles. It is expected that one can use ECL to record such <1 ms ultrafast events by further enhancing the sensitivity of ECL processes. Our study suggests that ECL can be an effective means for imaging transient redox processes when used on large arrays of closed bipolar electrodes.

4.5 FIGURES

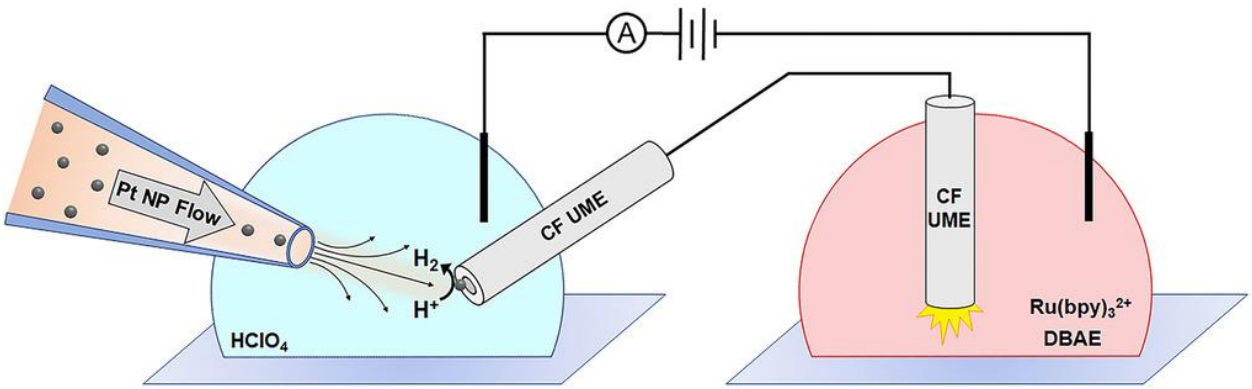

Figure 4.1. Schematic of the Closed-Bipolar NP Collision – ECL Setup.

A diagram of the experiment coupling Pt nanoparticle collisions to anodic ECL across a closed-bipolar electrode. The coverslips imply that both the microjet collision and reporting ECL halves were supported on separate inverted microscopes. A picture of the experimental setup is shown in Figure 4.12.

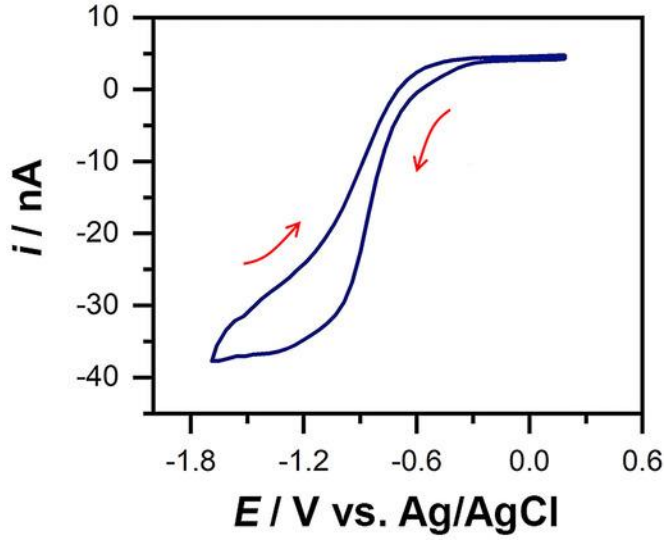

Figure 4.2. Bipolar Cyclic Voltammogram of Pt-Catalyzed HER Coupled to ECL.

A bipolar cyclic voltammogram (CV) recorded using a 50 µm Pt UME in 25 mM $HClO_4$ and 20 mM $NaClO_4$ coupled to a 5 µm CFE in 25 mM $Ru(bpy)_3^{2+}$, 20 mM DBAE, and 50 mM phosphate buffer (pH = 7.4). The CV was recorded at 100 mV/s using two Ag/AgCl quasi-reference electrodes (QREs) as driving electrodes. The arrows indicate the forward and backward scan.

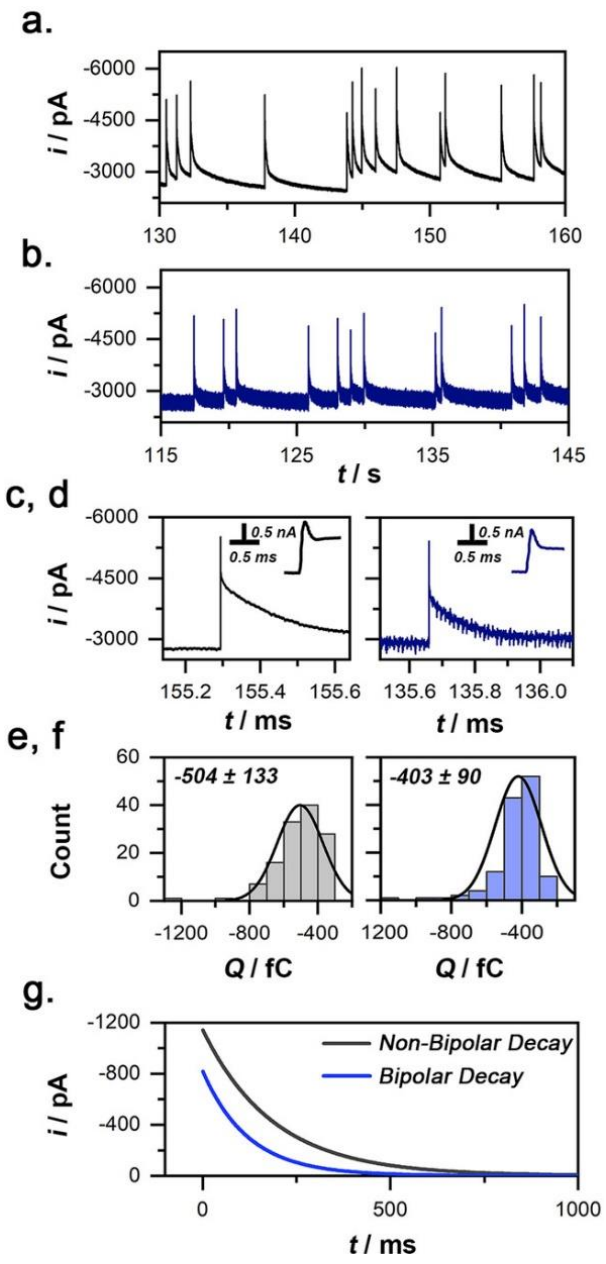

Figure 4.3. Analysis of Bipolar and Non-Bipolar Amperometric NP Collisions.

Bipolar data is shown in blue, and non-bipolar data is shown in grey. 2a and 2b show amperometric traces over a 30 second period. 2c and 2d examine single peaks, while highlighting the presence of the hydrogen adsorption spike in their insets. 2e and 2f quantify the charge (fC) of the hydrogen adsorption spike across 150 events each. 2g plots the average of 25 exponential decay curves fit to the electrochemical data. See the experimental section for fitting details.

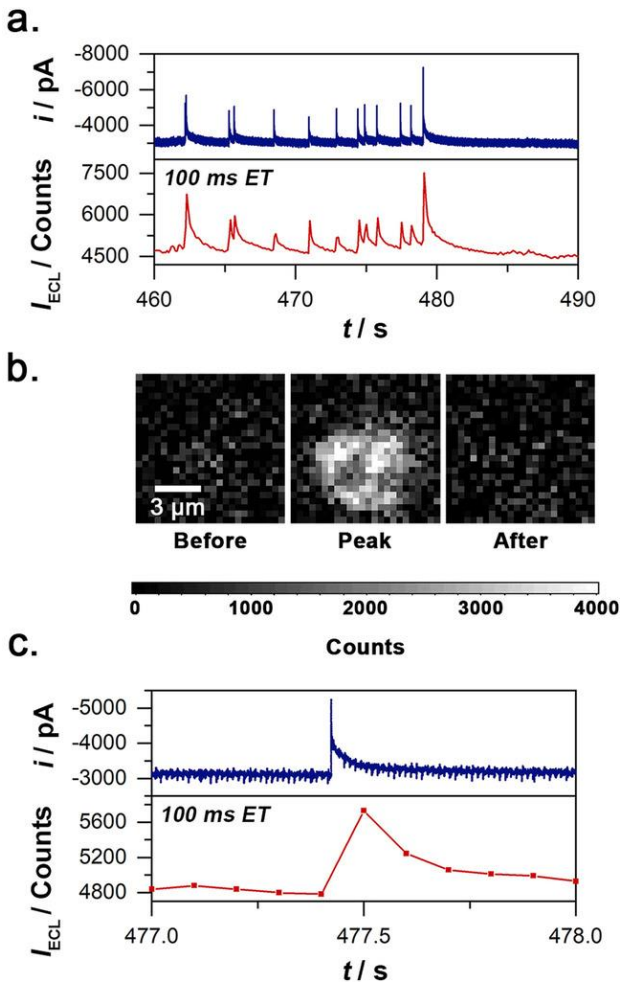

Figure 4.4. Correlated Amperometric and Optical Bipolar ECL NP Collisions.

Correlated amperometric (blue) and optical (red) recordings of nanoparticle collision events. 3a shows a correlated 30-second-long trace recorded using a 100 ms optical exposure time. 3b shows the recorded ECL images of the reporting CFE electrode before, during, and after returning the baseline of the single event shown in 3c. The optical frames were background corrected. 3c examines a single correlated event using the 100 ms exposure time.

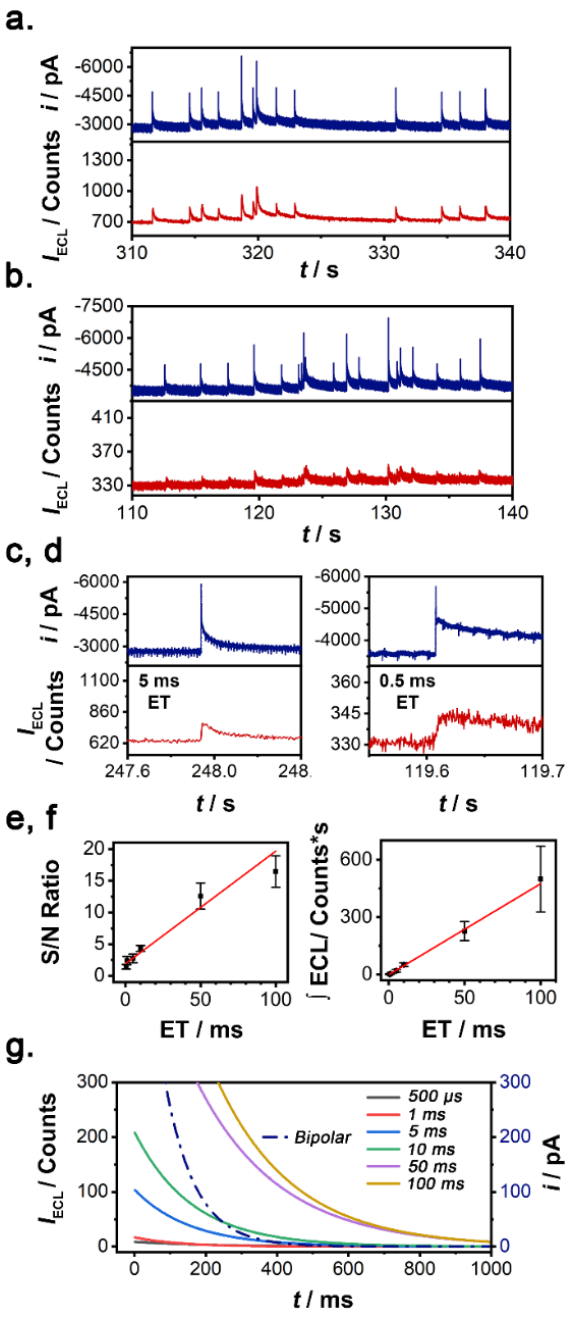

Figure 4.5. The Effect of Varied Optical Exposure Time on Bipolar ECL NP Collisions.

4a and 4b show 30-second traces correlating bipolar amperometric (blue) and ECL (red) signals using 5 ms Exposure Time (ET) and 0.5 ms ET, respectively. 4c and 4d examine single correlated events for 5 ms ET and 0.5 ms ET. 4e plots the signal-to-noise ratio vs. ET, found from measuring 25 peaks at each condition. 4f plots the area of the integrated ECL peak vs. ET to determine the relative number of photons per event. 4g plots the average of 25 exponential decay curves fit to the optical ECL data for varied ET's. The bipolar amperometric peak from 2g is overlaid on 4g. See the experimental section for fitting details.

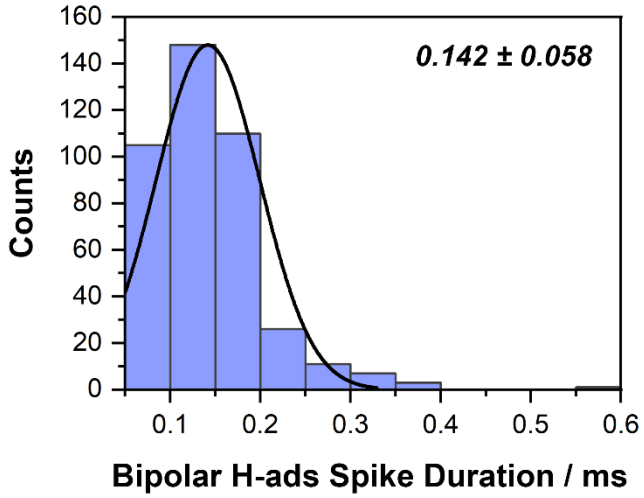

Figure 4.6. Average Duration of the Measured Bipolar Hydrogen Adsorption Spike.

The hydrogen adsorption spike duration was quantified across 150 electrochemical events. The average ± standard deviation was found to be 0.142 ± 0.058 ms. The average spike duration is quoted as being approximately 150 µs throughout the manuscript.

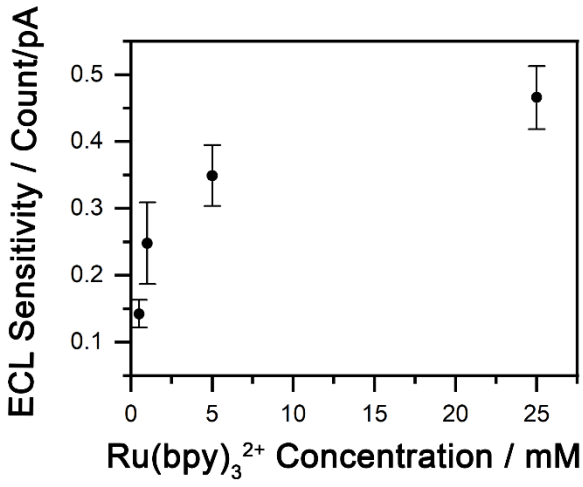

Figure 4.7. ECL Sensitivity vs. $Ru(bpy)_3^{2+}$ Concentration.

Correlated ECL-CV's were collected using a simple 2-electrode setup consisting of a glass-sealed carbon fiber electrode immersed in each $Ru(bpy)_3^{2+}$ concentration with 20 mM DBAE and 50 mM pH 7.4 phosphate buffer and a Ag/AgCl reference wire. A 10 ms exposure time was used. The ECL counts and corresponding current (pA) were used at identical potentials upon reaching the steady-state region of the CV. Each condition was performed in triplicate.

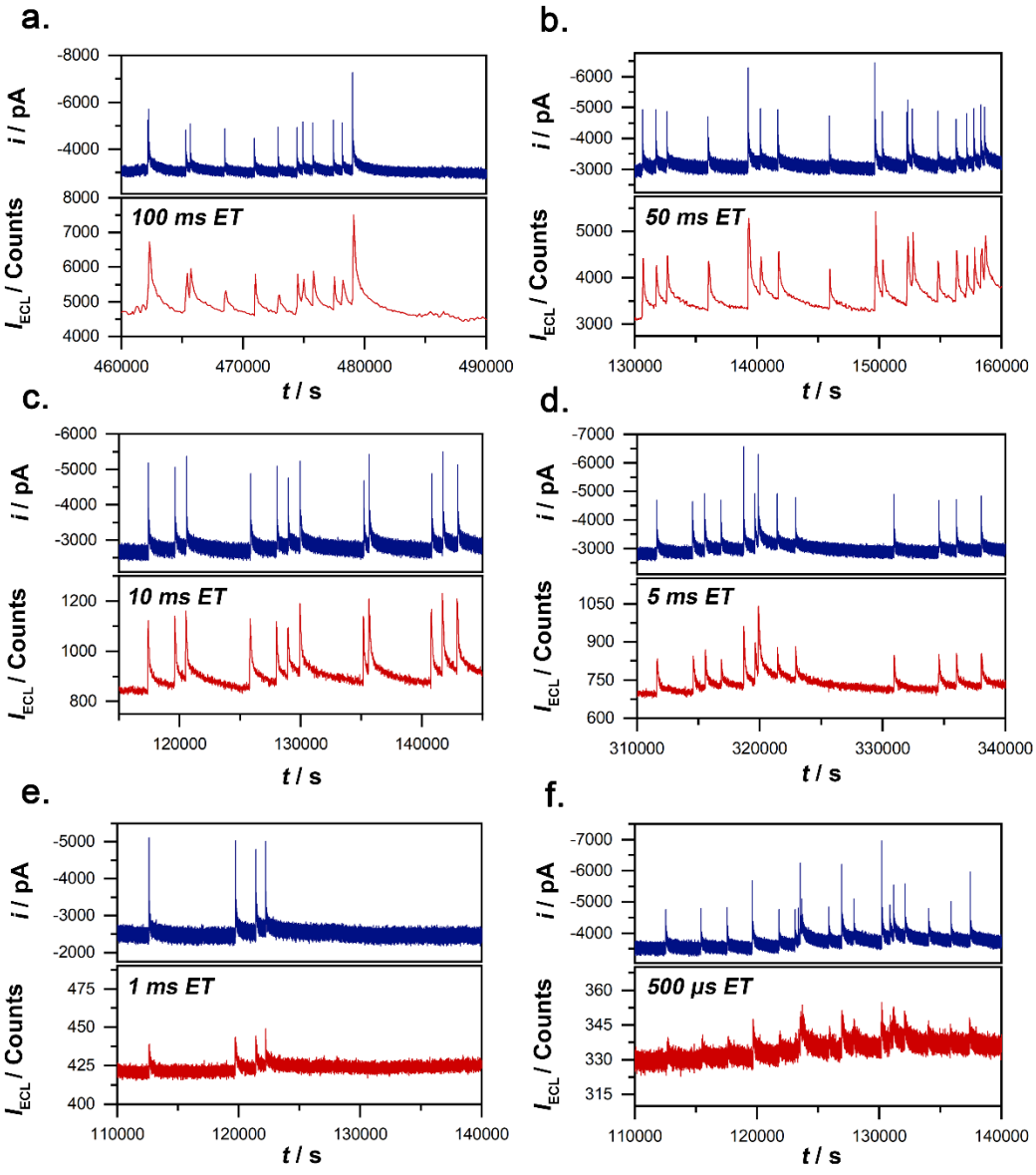

Figure 4.8. Correlated Bipolar Electrochemical (i-t) and Optical (Count-t) Traces.

Each trace is 30 seconds in duration with the following optical exposure times: a = 100 ms, b = 50 ms, c = 10 ms, d = 5 ms, e = 1 ms, f = 500 µs. The blue curves show bipolar electrochemical data, and the red curves show correlated bipolar ECL data.

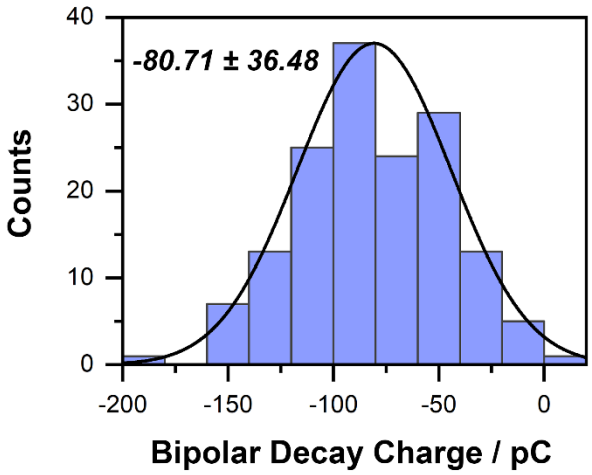

Figure 4.9. Average Charge of Transient Decay for Bipolar Hydrogen Evolution.

The hydrogen evolution decay charge was quantified for 150 bipolar electrochemical events. The average ± standard deviation was found to be -80.71 ± 36.48 pC.

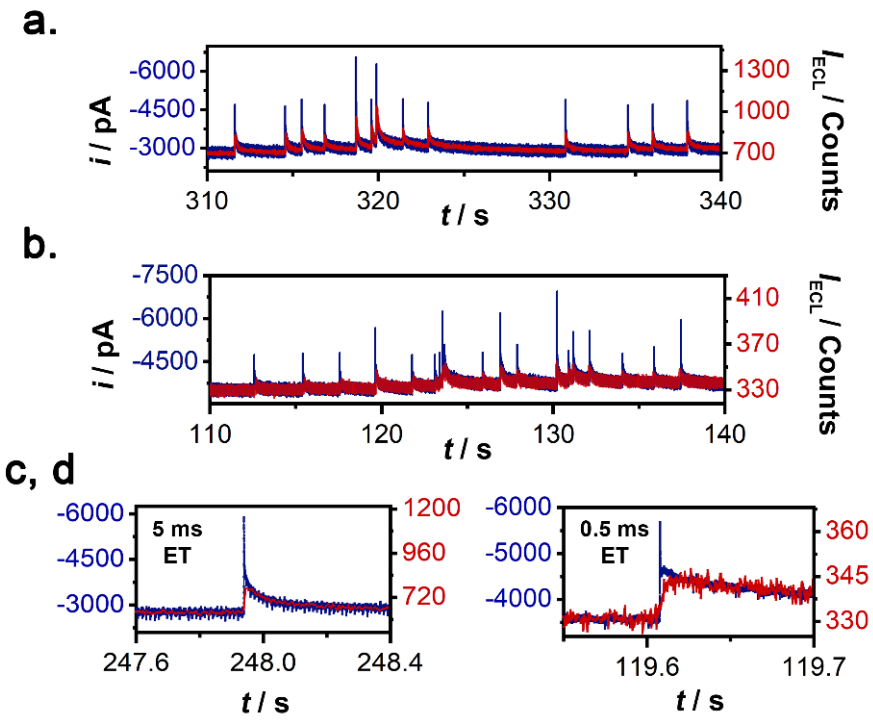

Figure 4.10. Demonstration of the Optical Resolution of Hydrogen Evolution.

We directly overlaid Figure 4.4a-d to demonstrate the accurate correlation of the ECL signal for resolving the hydrogen evolution decay process. Figure 4.10a and 4.10c use 5 ms exposure time, while 4.10b and 4.10d use 0.5 ms exposure time. The amperometric traces are in blue, and the ECL traces are in red.

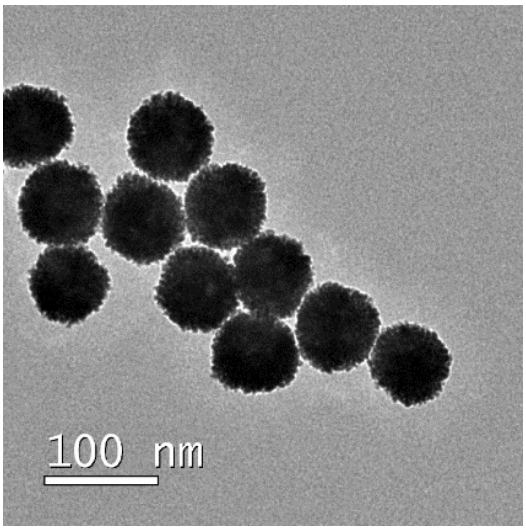

Figure 4.11. Characterization of 70 nm Pt Nanoparticles using TEM.

A high-resolution transmission electron microscope (TEM) image of the 70 nm Pt nanoparticles used in the nanoparticle collision experiments.

Figure 4.12. Photo of Experimental Setup for Correlated NP Collisions.

Two inverted microscopes were setup side-by-side for the bipolar NP collision experiment. The left microscope performed microjet Pt NP collisions, while the right microscope recorded optical ECL signal from a microelectrode. A long alligator clip connected both working electrodes.

4.6 REFERENCES

(1) Chang, B.-Y.; Chow, K.-F.; Crooks, J. A.; Mavre, F.; Crooks, R. M. Two-Channel Microelectrochemical Bipolar Electrode Sensor Array. *Analyst.* **2012**, *137*, 2827–2833.

(2) Wu, M.-S.; Yuan, D.-J.; Xu, J.-J.; Chen, H.-Y. Sensitive Electrochemiluminescence Biosensor Based on Au-ITO Hybrid Bipolar Electrode Amplification System for Cell Surface Protein Detection. *Anal. Chem*. **2013**, *85*, 11960–11965.

(3) Fosdick, S. E.; Crooks, R. M. Bipolar Electrodes for Rapid Screening of Electrocatalysts. *J. Am. Chem. Soc*. **2011**, *134*, 863–866.

(4) Fosdick, S. E.; Berglund, S. P.; Mullins, C. B.; Crooks, R. M. Parallel Screening of Electrocatalyst Candidates Using Bipolar Electrochemistry. *Anal. Chem*. **2013**, *85*, 2493–2499.

(5) Logent, G.; Roche, J.; Kuhn, A. True Bulk Synthesis of Janus Objects by Bipolar Electrochemistry. *Adv. Mater*. **2012**, *24*, 5111–5116.

(6) Bradley, J.-C.; Ma, Z. Contactless Electrodeposition of Palladium Catalysts. *Angew. Chem. Int. Ed.* **1999**, *38* (11), 1663–1666.

(7) Cox, J. T.; Guerrette, J. P.; Zhang, B. Steady-State Voltammetry of a Microelectrode in a Closed Bipolar Cell. *Anal. Chem.* **2012**, *84* (20), 8797–8804.

(8) Kostiuchenko, Z. A.; Zhang, B.; Lemay, S. G. Stochastic Charge Fluctuations in Bipolar Electrodes. *J. Phys. Chem. C*. **2016**, *120*, 22777–22783.

(9) Guerrette, J. P.; Oja, S. M.; Zhang, B. Coupled Electrochemical Reactions at Bipolar Microelectrodes and Nanoelectrodes. *Anal. Chem*. **2012**, *84*, 1609–1616.

(10) Plana, D.; Jones, F. G. E.; Dryfe, R. A. W. The Voltammetric Response of Bipolar Cells: Reversible Electron Transfer. *J. Electroanal. Chem*. **2010**, *646*, 107–113.

(11) Fosdick, S. E.; Crooks, J. A.; Chang, B.-Y.; Crooks, R. M. Two-Dimensional Bipolar Electrochemistry. *J. Am. Chem. Soc.* **2010**, *132*, 9226–9227.

(12) Fosdick, S. E.; Knust, K. N.; Scida, K.; Crooks, R. M. Bipolar Electrochemistry. *Agnew. Chem. Int. Ed.* **2013**, *52*, 10438–10456.

(13) Chow, K.-F.; Chang, B.-Y.; Zaccheo, B. A.; Mavre, F.; Crooks, R. M. A Sensing Platform Based on Electrodissolution of a Ag Bipolar Electrode. *J. Am. Chem. Soc.* **2010**, *132*, 9228–9229.

(14) Loget, G.; Zigah, D.; Bouffier, L.; Sojic, N.; Kuhn, A. Bipolar Electrochemistry: From Materials Science to Motion and Beyond. *Acc. Chem. Res.* **2013**, *46* (11), 2513–2523.

(15) Zhang, J.-D.; Lu, L.; Zhu, X.-F.; Zhang, L.-J.; Yun, S.; Duanmu, C.-S.; He, L. Direct Observation of Oxidation Reaction via Closed Bipolar Electrode-Anodic Electrochemiluminescence Protocol: Structural Property and Sensing Applications. *ACS Sensors.* **2018**, *3*, 2351–2358.

(16) Bouffier, L.; Arbault, S.; Kuhn, A.; Sojic, N. Generation of Electrochemiluminescence at Bipolar Electrodes: Concepts and Applications. *Anal Bioanal Chem.* **2016**, *408*, 7003–7011.

(17) Chow, K.-F.; Mavre, F.; Crooks, J. A.; Chang, B.-Y.; Crooks, R. M. A Large-Scale, Wireless Electrochemical Bipolar Electrode Microarray. *J. Am. Chem. Soc.* **2009**, *131*, 8364–8365.

(18) Oja, S. M.; Guerrette, J. P.; David, M. R.; Zhang, B. Fluorescence-Enabled Electrochemical Microscopy with Dihydroresorufin as a Fluorogenic Indicator. *Anal. Chem.* **2014**, *86*, 6040–6048.

(19) Oja, S. M.; Zhang, B. Electrogenerated Chemiluminescence Reporting on Closed Bipolar Microelectrodes and the Influence of Electrode Size. *ChemElectroChem.* **2016**, *3*, 457–464.

(20) Bouffier, L.; Doneux, T.; Goudeau, B.; Kuhn, A. Imaging Redox Activity at Bipolar Electrodes by Indirect Fluorescence Modulation. *Anal. Chem.* **2014**, *86*, 3708–3711.

(21) Liu, H.; Zhou, X.; Liu, W.; Yang, X.; Xing, D. Paper-Based Bipolar Electrode Electrochemiluminescence Switch for Label-Free and Sensitive Genetic Detection of Pathogenic Bacteria. *Anal. Chem.* **2016**, *88*, 10191–10197.

(22) Wu, M.-S.; Liu, Z.; Xu, J.-J.; Chen, H.-Y. Highly Specific Electrochemiluminescence Detection of Cancer Cells with a Closed Bipolar Electrode. *ChemElectroChem.* **2016**, *3*, 429–435.

(23) Bouffier, L.; Manojlovic, D.; Kuhn, A.; Sojic, N. Advances in Bipolar Electrochemiluminescence for the Detection of Biorelevant Molecular Targets. *Curr. Opin. Electrochem.* **2019**, *16*, 28–34.

(24) Zhai, Q.; Zhang, X.; Han, Y.; Zhai, J.; Li, J.; Wang, E. A Nanoscale Multichannel Closed Bipolar Electrode Array for Electrochemiluminescence Sensing Platform. *Anal. Chem.* **2016**, *88*, 945–951.

(25) Xu, W.; Ma, C.; Bohn, P. W. Coupling of Independent Electrochemical Reactions and Fluorescence at Closed Bipolar Interdigitated Electrode Arrays. *ChemElectroChem.* **2016**, *3*, 422–428.

(26) Oja, S. M.; Zhang, B. Imaging Transient Formation of Diffusion Layers with Fluorescence-Enabled Electrochemical Microscopy. *Anal. Chem.* **2014**, *86* (24), 12299–12307.

(27) Guerrette, J. P.; Percival, S. J.; Zhang, B. Fluorescence Coupling for Direct Imaging of Electrocatalytic Heterogeneity. *J. Am. Chem. Soc.* **2013**, *135* (2), 855–861.

(28) Borchers, J. S.; Riusech, O.; Rasmussen, E.; Anand, R. K. Visual Voltammogram at an Array of Closed Bipolar Electrodes in a Ladder Configuration. *J. Anal. Test.* **2019**, *3*, 150–159.

(29) Lin, X.; Zheng, L.; Gao, G.; Chi, Y.; Chen, G. Electrochemiluminescence Imaging-Based High-Throughput Screening Platform for Electrocatalysts Used in Fuel Cells. *Anal. Chem.* **2012**, *84*, 7700–7707.

(30) Wu, M.-S.; Liu, Z.; Shi, H.; Chen, H.-Y.; Xu, J.-J. Visual Electrochemiluminescence Detection of Cancer Biomarkers on a Closed Bipolar Electrode Array Chip. *Anal. Chem.* **2015**, *87*, 530–537.

(31) Liu, X.; Tong, Y.; Fang, P. Trends in Analytical Chemistry Recent Development in Amperometric Measurements of Vesicular Exocytosis. *Trends Anal. Chem.* **2019**, *113*, 13–24.

(32) Wightman, R. M.; Jankowski, J. A.; Kennedy, R. T.; Kawagoe, K. T.; Schroeder, T. J.; Leszczyszyn, D. J.; Near, J. A.; Diliberto, E. J.; Viveros, O. H. Temporally Resolved Catecholamine Spikes Correspond to Single Vesicle Release from Individual Chromaffin Cells. *Proc. Natl. Acad. Sci.* **1991**, *88*, 10754–10758.

(33) Defnet, P. A.; Han, C.; Zhang, B. Temporally-Resolved Ultrafast Hydrogen Adsorption and Evolution on Single Platinum Nanoparticles. *Anal. Chem.* **2019**, *91*, 4023–4030.

(34) Liu, X.; Shi, L.; Niu, W.; Li, H.; Xu, G. Environmentally Friendly and Highly Sensitive Ruthenium(II) Tris(2,2′-Bipyridyl) Electrochemiluminescent System Using 2-(Dibutylamino)Ethanol as Co-Reactant. *Angew. Chemie - Int. Ed.* **2007**, *46*, 421–424.

(35) Ma, C.; Wu, W.; Li, L.; Wu, S.; Zhang, J.; Chen, Z.; Zhu, J.-J. Dynamically Imaging Collision Electrochemistry of Single Electrochemiluminescence Nano-Emitters. *Chem. Sci.* **2018**, *9*, 6167–6175.

(36) Hao, R.; Fan, Y.; Zhang, B. Imaging Dynamic Collision and Oxidation of Single Silver Nanoparticles at the Electrode/Solution Interface. *J. Am. Chem. Soc.* **2017**, *139*, 12274–12282.

(37) Oja, S. M.; Robinson, D. A.; Vitti, N. J.; Edwards, M. A.; Liu, Y.; White, H. S.; Zhang, B. Observation of Multipeak Collision Behavior during the Electro-Oxidation of Single Ag Nanoparticles. *J. Am. Chem. Soc.* **2016**, *139* (2), 708–718.

(38) Xiang, Z. P.; Deng, H. Q.; Peljo, P.; Fu, Z. Y.; Wang, S. L.; Mandler, D.; Sun, G. Q.; Liang, Z. X. Electrochemical Dynamics of a Single Platinum Nanoparticle Collision Event for the Hydrogen Evolution Reaction. *Angew. Chemie - Int. Ed.* **2018**, *57*, 3464–3468.

(39) Bard, A. J.; Faulkner, L. R.; Leddy, J.; Zoski, C. G. Electrochemical Methods: Fundamentals and Applications; Wiley: New York, **1980**.

(40) Cox, J. T.; Guerrette, J. P.; Zhang, B. Steady-State Voltammetry of a Microelectrode in a Closed Bipolar Cell. *Anal. Chem.* **2012**, *84*, 8797–8804.

(41) Zhou, Z.; Guo, W.; Xu, L.; Yang, Q.; Su, B. Two Orders-of-Magnitude Enhancement in the Electrochemiluminescence of $Ru(bpy)_3^{2+}$ by Vertically Ordered Silica Mesochannels. *Anal. Chim. Acta*. **2015**, *886*, 48–55.

(42) Guo, W.; Lin, X.; Yan, F.; Su, B. Vertically Ordered Silica Mesochannel Modified Bipolar Electrode for Electrochemiluminescence Imaging Analysis. *ChemElectroChem*. **2016**, *3*, 480–486.

(43) Kim, Y.; Kim, J. Modification of Indium Tin Oxide with Dendrimer-Encapsulated Nanoparticles to Provide Enhanced Stable Electrochemiluminescence of $Ru(bpy)_3^{2+}$/Tripropylamine While Preserving Optical Transparency of Indium Tin Oxide for Sensitive Electrochemiluminescence-Based Analyses. *Anal. Chem.* **2014**, *86*, 1654–1660.

Chapter 5. EXPLORATION OF TWO CATHODIC LIGHT GENERATION SYSTEMS FOR BIPOLAR SILVER NANOPARTICLE DETECTION

5.1 INTRODUCTION

Closed-bipolar electrochemical imaging (c-BPI) has shown great promise toward the micro- or nanoscale spatial mapping of electrochemical redox environments. As discussed in Chapter 1, this technique relies on the coupling of two complementary half-reactions across opposite poles of a bipolar electrode. By utilizing a light-generation process at a single pole, the light intensity can serve as the reporting mechanism indicative of electrochemical activity. Thus, electrochemical sensing can be extended to arrays containing thousands of wireless bipolar electrodes, all while utilizing a microscope camera as a single recording channel.[1]

A long-term lab goal established in 2012 has been to extend the c-BPI platform to map *in-vitro* oxidative neurotransmitter release during exocytosis from single dopaminergic cells and brain slices. Exocytosis is a key process that facilitates chemical communication among neuronal networks in the brain. Significant efforts in the literature have been devoted to better understanding its physical mechanism due to its direct impact on neurodegenerative disorders such as Parkinson's disease.[2,3] The application of closed-bipolar imaging with densely packed nanoelectrode arrays could allow for high spatial resolution mapping of exocytotic release sites for fundamental studies regarding neurotransmission dynamics.

Classical exocytosis electrochemical measurements were pioneered by Mark Wightman with use of single cell amperometry in the 1990's.[4–7] In this technique a single electrode is placed at the cellular interface and to stimulate neurotransmitter release via exposure to a high potassium

salt solution. Detected signals appear as dozens of temporally resolved peaks, where each peak represents a single vesicle fusing with the cell wall and expunging its contents into extracellular space to be detected at the electrode surface. The classic amperometric method has been used to discover different features of the release mechanism, such as quantitative estimates of vesicular neurotransmitter content,[8] and incomplete vesicular fusion under certain conditions.[9] However, the classical technique cannot provide spatial information indicating where the release occurs across the biological medium, which instead would require the application of multiple electrodes.

Indeed, other labs have developed multi-channel electrochemical methods in pursuit of the same goal of spatially resolving exocytotic release. Early efforts used a brute-force methodology of simply placing more ultramicroelectrodes across the cell surface. Each required its own manipulator and current amplifier and involved a very technical and cumbersome setup.[10] Efforts then progressed into using multi-barreled electrodes, thus requiring a single manipulator; however, authors have only reported a maximum of seven electrode-arrays which, still require significant technical prowess to fabricate.[11] The advent of directly-wired micro-fabricated arrays allowed for massive scalability and parallelization of electrode designs, with initial reports monitoring with up to 36 electrodes,[12,13,14] and more modern reports monitoring with upwards of 4096.[15,16,17] The modern arrays utilize CMOS technology with current amplifiers fabricated onto the chip itself, providing extreme sensitivity and temporal resolution. For example, Ham and co-workers demonstrated a 4096-electrode device with ~10 μm diameter electrodes and 20 μm pitch that allow for the spatial mapping of neuronal action potentials.[15]

Arguably similar fundamental studies can be performed with both the microelectrode and CMOS arrays to what was originally proposed with c-BPI. However, an important advantage for our methodology is the ability to employ nanoelectrode arrays with more densely packed

structures, only limited by the need for thin insulating membranes separating each electrode. For example, a recent paper from Xia and co-workers demonstrated the fabrication of nanoelectrode arrays from gold electrodeposition in anodized aluminum oxide membranes, leading to 200 nm diameter electrodes with 450 nm pitch.[18] Such work far surpasses the electrode density attainable with CMOS technology, providing even higher spatial resolution.

However, the real challenge of exocytotic c-BPI is in identifying a cathodic light-generating system with enough sensitivity to detect the small and fast vesicular release events. Table 5.1 summarizes the average peak charge and duration of amperometric exocytosis for various biological systems. A natural analytical progression would be to start with easier detection targets, such as with chromaffin cells (1190 fC, 200 ms)[19] and progress towards smaller, faster events, until reaching the human neuronal thresholds (3.3 fC, 0.09 ms).[20] Yet it is important to remember that the optical sensitivity in c-BPI is impacted by both the amount of charge transferred, and optical frame rate as demonstrated in Chapter 4.[21] Thus, the approach toward neuronal detection requires multinomial sensitivity improvements.

The strategy employed to address this analytical challenge was to first identify a cathodic light generating system that can detect an oxidative transient of any size. Once a baseline is established, sequential improvements can be made to achieve the series of analytical targets. Ag nanoparticle (NP) collisions were used as the source of transient oxidative charge during this optimization process (as introduced in Chapter 3). Their integrated charge matches quite well with the proposed biological targets (as illustrated in Figure 5.1) yet they are far cheaper and easier to handle during experimentation. The present work describes unpublished progress highlighting two distinct cathodic light generation mechanisms, as well as critical factors that influence their applicability toward c-BPI.

5.2 EXPERIMENTAL

5.2.1 *Chemicals*

All chemicals were used as received from their manufacturer, including resazurin (Rz, 99.9%, Sigma Aldrich), monobasic potassium phosphate (KH_2PO_4, 99.8%, Fisher Chemical), dibasic potassium phosphate (K_2HPO_4, 99.9%, J.T. Baker), potassium nitrate (KNO_3, 99%, Sigma-Aldrich), perchloric acid ($HClO_4$, 70%, Sigma-Aldrich), sodium perchlorate monohydrate ($NaClO_4 \cdot H_2O$, >99%, Fluka), sodium sulfite (Na_2SO_3, 99%, Sigma Aldrich), D-(+)-glucose (Glucose, 98%, Sigma Aldrich), acetonitrile (AcN, 99%, Sigma-Aldrich), tetrabuytlammonium hexafluorophoshate ($TBAPF_6$, 98%, Sigma Aldrich), ammonium persulfate ($(NH_4)_2S_2O_8$, APS, ≥98.0%, Sigma Aldrich), tris(2,2'-bipyridyl)dichlororuthenium(II) hexahydrate ($Ru(bpy)_3^{2+}$, 99%, Sigma-Aldrich), 2-(dibutylamino)ethanol (DBAE, 99%, Sigma-Aldrich), ferrocenemethanol (FcMeOH, 97%, Sigma-Aldrich), and potassium chloride (KCl, 99%, J.T. Baker). Citrate-capped Ag nanoparticles with diameter 60 ± 7 nm dispersed in 2 mM sodium citrate and citrate-capped Pt nanoparticles with 30 nm ± 3nm dispersed in 2 mM sodium citrate were both purchased from NanoComposix (San Diego, CA). Solutions were prepared with nanopure water purified to a resistivity of 18.2 MΩ cm^{-1} (Barnstead Nanopure system, Thermo Scientific).

5.2.2 *Electrode Fabrication*

The 25 µm Au UMEs used for Ag NP collisions and the 5 µm carbon fiber electrodes (CFEs) were both fabricated according to a procedure previously reported by our group.[22] A single wire (25 µm Au or 5 µm carbon fiber) was aspirated into a borosilicate glass capillary tube (1.2 mm O.D./0.69 mm I.D., Sutter). One end of the capillary was sealed shut using a Bunsen burner. A vacuum line was connected to the open end of the tube and the fiber was sealed using a heating

coil. Care was taken to avoid bubble formation around the wire. The electrode disk was exposed by sanding with P-60 and P-220 grade sandpaper. A 250 µm diameter tungsten wire was dipped in Ag paste epoxy (Dupont) and used to make contact to the posterior carbon fiber inside the capillary. Epoxy (Hysol 0151) was used to secure the tungsten wire to the end of the capillary.

All electrodes were characterized using cyclic voltammetry in 1 mM FcMeOH and 100 mM KCl. A fresh electrode surface was exposed prior to every experiment by polishing with P-220 grade sandpaper.

5.2.3 *Imaging Setup*

Resazurin, dihydroresorufin, and cathodic ECL experiments employed the same optical imaging setup. The reporting electrode was submerged in a reservoir of the respective light-generating solution and was positioned above a glass coverslip using a MP-225 micromanipulator (Sutter Instrument Co.) The electrode disc was put into focus using an Olympus Ix70 inverted microscope. The optical signal was collected using a 40x (1.15 NA Uapo-340) water-immersion objective and recorded using an Andor iXon 897E EMCCD camera cooled to -80° C. The pre-amplifier gain was set to 5.1x, the readout rate was 10 MHz at 14-bit, and the vertical pixel shift speed was set to 0.3 µs. The electron multiplier (EM) gain is set to 300 and optical exposure time was 30 ms unless otherwise noted. Andor SOLIS software was used to record all imaging data. Andor SOLIS and ImageJ were used for image processing.

5.2.4 *Electrochemical Recordings*

Correlated optical-electrochemical CVs were driven utilizing a ChemClamp potentiostat/current amplifier (Dagan Corporation) with a headstage (N=1 for resazurin and dihydroresorufin, and N=0.01 for cathodic ECL) connected to two Ag/AgCl reference electrodes

placed in each of the separated bipolar solutions. Electrochemical CVs were recorded using a custom LabVIEW program which also contained a digital trigger to initiate the potential sweep and optical recording simultaneously.

Correlated bipolar Ag NP collisions used the same current amplifier while sampling at 100 kHz with a 1322A digitizer (Axon Instruments) and filtering at 10 kHz using a hardware low-pass Bessel filter. *I-t* data was recorded using Axoscope 10.0 software (Molecular Devices) and analyzed in Clampfit 10.7 (Molecular Devices) software.

All experiments were performed inside a grounded faraday cage positioned on top of a vibration-isolation table.

5.3 Results and Discussion

5.3.1 *Resazurin*

Resazurin is a weakly fluorescent redox-active dye ($\Phi = 0.11$) that can be electrochemically reduced to the strongly fluorescent species, resorufin ($\Phi = 0.75$), as shown in Figure 5.2.[23] Diffuse resazurin was classically employed as the light-generation pole for imaging long time-scale oxidative processes with carbon fiber bundled arrays in our lab's early c-BPI papers.[1] Given its previous success, it became a natural first choice for a reporter species when approaching the present exocytosis c-BPI project.

Figure 5.3 shows an optical cyclic voltammogram of resazurin reduction on a directly connected (non-bipolar) carbon fiber electrode sealed in glass. The onset potential for light generation begins at ~ -350 mV. A large optical signal of at least ~2500 counts is produced upon application of between -1000 mV to -1600 mV, indicative of a wide and stable potential window for light generation.

In the following experiments, resazurin reduction was coupled to Ag NP oxidative collisions across a single bipolar microelectrode to test its capacity for detecting transient oxidative events. Equation 1 is used to calculate the theoretical driving potential across the bipolar electrode, where E_{anode} is the driving potential on the anodic pole, and $E_{cathode}$ is the driving potential on the cathodic pole of the bipolar electrode.[24]

$$E_{bipolar} = E_{anode} - E_{cathode} \quad (1)$$

Given that resazurin reduction occurs at ~ -400 V vs. Ag/AgCl, and Ag NP oxidation occurs between +400 mV and +700 mV vs. Ag/AgCl as found from work in Chapter 3, we would expect at least 800 mV to be required for this bipolar process. However, the application of more potential is safe given the stability of both half-reactions at higher overpotentials.

Figure 5.4 shows an experimental diagram for the coupled optical bipolar collisions. The Ag NP pole was housed in a beaker adjacent to the microscope stage, while the resazurin pole is kept directly in focus using an inverted microscope and EM-CCD camera. An Au UME was used for Ag NP collisions because of its superior performance for the reaction, and a carbon fiber UME was used on the light-generation pole to better mimic the pyrolytic carbon array material utilized in Chapter 6. Incident Ag NP collisions produce oxidative charge that is compensated by equivalent resazurin reduction at the opposite pole. Both reactions are necessary to observe any correlated amperometric signal via circuit completion. Thus, the collision event is converted to the optical output across the bipolar electrode.

Preliminary results for optical bipolar Ag NP collisions are shown in Figure 5.5 along with its correlated amperometric trace. Many correlated peaks were measured, but the single peak

displayed in Figure 5.5 was selected since it had the largest integrated charge with 6000 fC measured over 50 ms. Despite the large electrochemical signal, the corresponding optical signal was not detected. Note that the steady decrease in optical counts is due to photobleaching of resazurin's weak fluorescent background. Additional experiments were performed in the present experimental configuration, such as by varying the resazurin concentration from 50 – 500 µM and varying the exposure time from 20 ms to 50 ms; however, the correlated optical signal was absent in all cases.

Control experiments were undertaken to explore this negative result. Purely electrochemical bipolar Ag NP collisions were performed using the identical setup shown in Figure 5.4 except without the correlated optical response. We wanted to determine if different conditions on the light-generating pole could produce stronger electrochemical coupling as evidenced by larger peaks. However, a stunning result came from a negative control experiment. Nearly identical bipolar Ag NP collision peaks were recorded for reporting poles either containing resazurin and phosphate buffer (PB) or just PB (shown in Figure 5.6). We had previously assumed that correlated bipolar peaks were a direct result of only resazurin reduction, accepting all transferred electrons. In contrast, this result clearly showed that a second reduction process is occurring that may be diluting the optical signal due to electrons being transferred to a non-light generating process.

Continued investigation revealed that the mystery electron acceptor on the reporting pole was due to dissolved oxygen. Room temperature aqueous solutions contain 250 µM dissolved O_2, which is a large amount relative to the mere 50 µM resazurin used.[25] Figure 5.7 shows the electrochemical response for bipolar Ag NP collisions coupled to PB in the presence of the oxygen scavenger Na_2SO_3. Chemical removal of O_2 on the reporting pole eliminates the coupled Ag NP bipolar signal. Results can be nearly reproduced by bubbling PB with nitrogen for 1 hour, although

some small peaks still remained. It has been previously reported that gaseous purging does not remove all O_2 from solution, which helps to explain this result.[26]

Results suggested that removal of O_2 may improve the optical signal of resazurin. Initial optical experiments were undertaken utilizing the oxygen scavenger Na_2SO_3 as described above. However, it was found that Na_2SO_3 chemically reduces resazurin to resorufin even without applied potential. Instead, an airtight chamber was constructed as shown in Figure 5.8. Here, the UME and Ag/AgCl reference electrodes were inserted through a rubber septum atop a miniature side-arm flask. The UME was long enough to be viewed through the bottom of the flask and still remain in focus using an inverted microscope. Nitrogen was continuously bubbled into the side-arm and out the rubber septum through an inserted needle.

In Figure 5.9, a constant potential of -700 mV was applied across a directly connected (non-bipolar) electrode in resazurin solution. Figure 5.9a,b shows how the signal-to-noise ratio changes without and with N_2 purging, respectively. A clear improvement is observed following O_2 removal. The same airtight light-generation pole was then used for correlated optical bipolar Ag NP collisions. Figure 5.10 shows an example correlated trace. Even still, the N_2 purged resazurin did not produce enough optical signal for single peaks to be resolvable, despite the largest peak in Figure 5.10 containing 21650 fC over 200 ms.

5.3.2 *Exploring the Limits of Resazurin using Dihydroresorufin*

In thinking about the failure of resazurin to achieve a biologically useful sensitivity for bipolar transient events, it was proposed that the weakly fluorescent background may be the limiting factor. We chose to explore this idea with use of dihydroresorufin (PH_2), which has 0 fluorescent background and can be electrochemically oxidized to resorufin following the reaction scheme in Figure 5.2.[23] Given that oxidation must occur for fluorescence generation, PH_2 is not a

viable reporting species for biological detection. We instead viewed the results as the best possible outcome for diffuse resazurin detection if the fluorescent background could be removed.

The bipolar detection scheme is shown in Figure 5.11, whereby diffuse Pt NPs catalyze the hydrogen evolution reaction (HER) upon electrode collision and are couple to PH_2 oxidation to generate fluorescent resorufin on the reporting pole. The PH_2 solution contains excess glucose to chemically reduce resorufin back to PH_2, thereby serving as a fluorescent "turn-off" mechanism.[23] Correlated optical-electrochemical traces are shown in Figure 5.12. A near-perfect mirrored optical trace is produced with broadened peak decays. The broad optical decays are likely due to the combination of this "turn-off" effect and photobleaching.

The success of PH_2 provides hope for the future of this technology. The smallest detectable amperometric event for PH_2 has been identified as 240 fC over 10 ms, occurring at the ~80-second time marker in Figure 5.12. This minimum charge threshold meets the requirements for chromaffin cell exocytosis detection, and suggests that successful biological detection may be possible if an equivalent zero-background reduction pathway is identified for resorufin generation. However, there remains no clear path towards identifying such a species in literature.

Future work may alternatively employ more advanced optical techniques to reduce the high fluorescent background of resazurin. All optical measurements reported herein were collected on an inverted fluorescent microscope with a thick >100 μm layer of diffuse resazurin between the coverslip and reporting electrode surface. Minimizing the thickness may reduce the optical background, thus improving the signal-to-noise ratio. Alternative imaging setups, such as with total internal reflectance fluorescence (TIRF) microscopy may also prove advantageous.[27] TIRF inherently provides high sensitivity and low background measurements which would undoubtedly improve current limits of detection.

5.3.3 *Cathodic ECL*

We next examine cathodic ECL as an alternative light generation mechanism for the detection of transient bipolar oxidative species. Given the success of anodic ECL in Chapters 4 and 6, one may assume that cathodic ECL would be equivalently applicable. However, there are irreparable shortcomings for its use in c-BPI that will be described herein.

Cathodic ECL proceeds through a multistep radical mechanism requiring a luminophore ($Ru(bpy)_3^{2+}$) and a co-reactant.[28] The selected co-reactant needs to generate a strong oxidizing agent upon electrochemical reduction which will react with the reduced $Ru(bpy)_3^{2+}$ species to form an unstable radical that emits a single photon upon relaxation.[29] While identified co-reactants include $S_2O_8^{2-}$,[29] glutathione,[30] and H_2O_2,[31] the work herein utilized $S_2O_8^{2-}$ due to the extensive previous literature supporting its use. The multistep radical light-generation mechanism between $Ru(bpy)_3^{2+}$ and $S_2O_8^{2-}$ is shown below.[29]

$$Ru(bpy)_3^{2+} + e^- \rightarrow Ru(bpy)_3^{+} \quad (2)$$

$$Ru(bpy)_3^{+} + S_2O_8^{2-} \rightarrow Ru(bpy)_3^{2+} + SO_4^{-\cdot} + SO_4^{2-} \quad (3)$$

$$Ru(bpy)_3^{+} + SO_4^{-\cdot} \rightarrow Ru(bpy)_3^{2+*} + SO_4^{2-} \quad (4)$$

$$Ru(bpy)_3^{2+*} \rightarrow Ru(bpy)_3^{2+} + h\nu \quad (5)$$

The light intensity of cathodic ECL has been reported as 6-7 times the strength of anodic ECL.[28] Such results are initially promising towards our application requiring high sensitivity. However, cathodic ECL also requires 12-14 times more electrons transferred than anodic ECL to produce this more intense signal. Thus, the ECL efficiency (# photons generated / electron

transferred) is estimated as 0.025, exactly one half of that for anodic ECL (0.05).[28] The sensitivity is therefore expected to be 2x lower.

Cathodic ECL requires a precise balance between luminophore and co-reactant since $Ru(bpy)_3^{2+*}$ is quenched by $S_2O_8^{2-}$.[29] Conditions were previously optimized by White et al., which found the most intense light generation results from a combination of 1 mM $Ru(bpy)_3^{2+}$ and 18 mM $S_2O_8^{2-}$.[29] We also found that the freshness of $S_2O_8^{2-}$ is an important parameter in obtaining intense light-generation. Figure 5.13 includes ECL-CV's for the optimized condition, utilizing either fresh $S_2O_8^{2-}$ or 1 year-old $S_2O_8^{2-}$. Results show over a 99% decrease in signal intensity for the older chemical, emphasizing how the age of $S_2O_8^{2-}$ is a critical factor.

The unavoidable shortcomings of cathodic ECL become readily apparent by studying the correlated optical-electrochemical CV, as shown in Figure 5.14. The response is quite complex. Initial signs of light generation occur around -1450 mV whereby both the $Ru(bpy)_3^{2+}$ and co-reactant are reduced simultaneously. The optical intensity reaches a max value at -1580 mV and only extends to -1635 mV before decreasing in intensity; this process is correlated with the deposition of long conductive wires on the UME surface, as shown in Figure 5.14c, d. Although not shown in Figure 5.14, sweeping the potential below -1900 mV leads to the vigorous generation of H_2 bubbles from the reduction of water in the 1:1 H_2O:AcN solvent.

The most significant limiting factor with cathodic ECL is the small potential window in which maximum light generation occurs. While it is true that Equation 1 can predict the driving potential required to couple two half reactions across a bipolar system, there remain inconsistencies with this in practice. Of particular importance is an observation from the work performed in Chapter 6. When recording a correlated ECL-CV with a massive array of bipolar electrodes, we observed that the onset potential can vary up to 50 mV to drive the same reaction

to its neighboring electrodes.[32] It is therefore much preferred to utilize a stable imaging system wherein the application of much higher overpotential is allowed such as for resazurin reduction, (as shown in Figure 5.3) or anodic ECL. For example, Figure 5.15 includes a correlated ECL-CV for the anodic ECL system utilized in Chapters 4 and 6 which demonstrates the stable potential window extends for at least 600 mV following the initial maximum intensity at 1050 mV.

The small potential window for maximum light generation in cathodic ECL is likely due to the overlapping microwire formation at the electrode surface. Controlled experiments revealed this process is due to $Ru(bpy)_3^{2+}$ electrodeposition. The removal of $Ru(bpy)_3^{2+}$ from the environment disrupts the optimized ratio of $Ru(bpy)_3^{2+}$ to co-reactant and leads to a significant reduction in light output. As a result, the dozens of attempts in utilizing cathodic ECL for the detection of bipolar Ag NP collisions have failed.

It may be possible to extend the active potential window by utilizing an alternative luminophore with an electrodeposition potential lower than that of $Ru(bpy)_3^{2+}$. However, most alternative luminophores have lower ECL efficiencies than that of $Ru(bpy)_3^{2+}$ which further complicates the selection process.[28]

5.4 Conclusion

This chapter investigated the applications of diffuse resazurin and cathodic ECL for their use in cathodic c-BPI toward the detection of transient Ag NP collisions. Unfortunately, both methods failed to provide successful results. Cathodic ECL is limited by its small light generation potential window, preventing easy extension to a c-BPI configuration. Of particular interest is the failure of resazurin due to its high optical background. It is presumed that some resorufin fluorophores are generated from the correlated Ag NP collisions. Thus, there remains hope that an alternative imaging strategy may be employed to reduce the optical background of resazurin,

thereby allowing the collision signal to be detected. Such work is under active investigation from current members of our lab.

5.5 FIGURES

Table 5.1. Average Peak Charge and Duration for Biological Exocytosis Targets.

	Charge (fC)	Half Width (ms)
Chromaffin Cells[19]	1190 ± 90	20 - 200
PC12 Cells[33]	23.4 ± 1.86	1.96 ± 0.13
Neurons[20]	3.33 ± 0.32	0.092 ± 0.06

Figure 5.1. Comparison of Ag NP Peak Charge to Biological Targets.

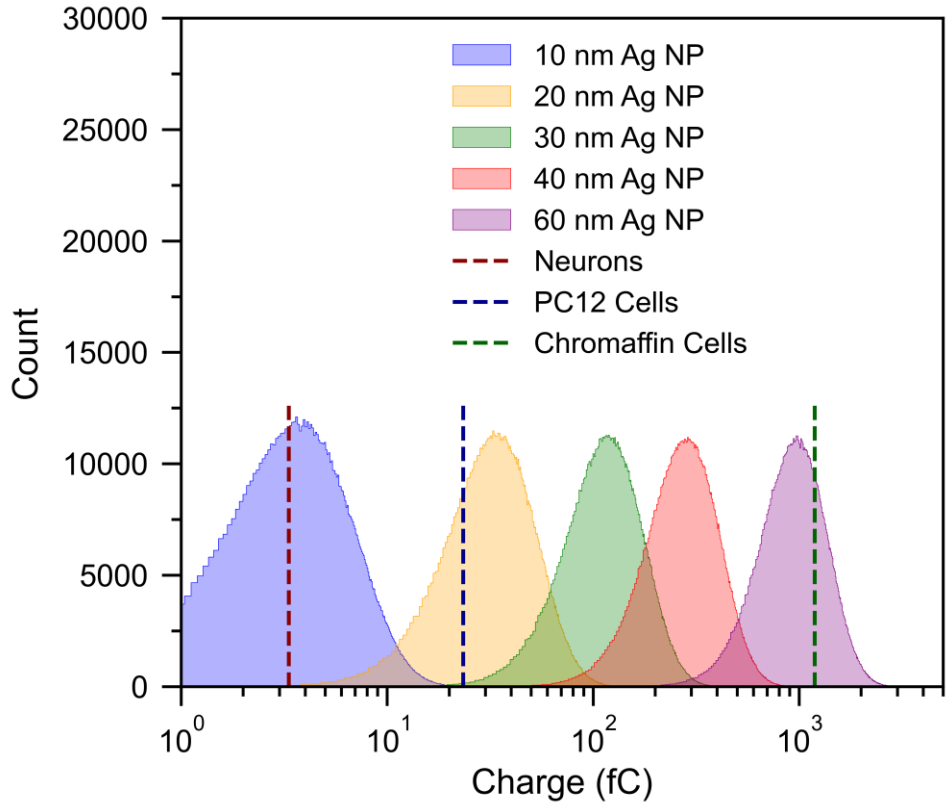

Figure 5.2. Schematic of the Imaging Reaction for Resazurin Reduction and Dihydroresorufin Oxidation.

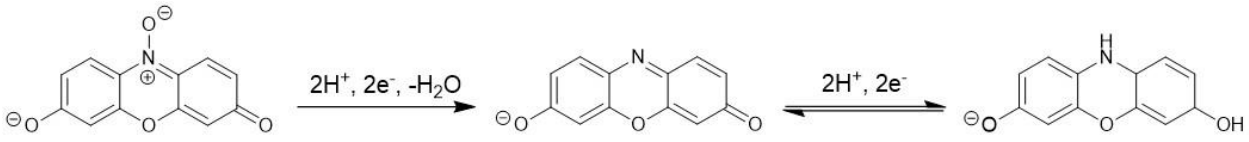

Resazurin (**S**)

Weakly Fluorescent

Φ = 0.11

Resorufin (**P**)

Fluorescent

Φ = 0.75

Dihydroresorufin ($\mathbf{PH_2}$)

Non-Fluorescent

Φ = 0

Figure 5.3. Correlated Optical Cyclic Voltammogram for Resazurin Reduction with a Directly-Connected (Non-Bipolar) Electrode.

Solution conditions consisted of 250 µM resazurin in 50 mM PB at pH 7.4. Here, the camera's EM gain was set to 0 to prevent overloading of the camera.

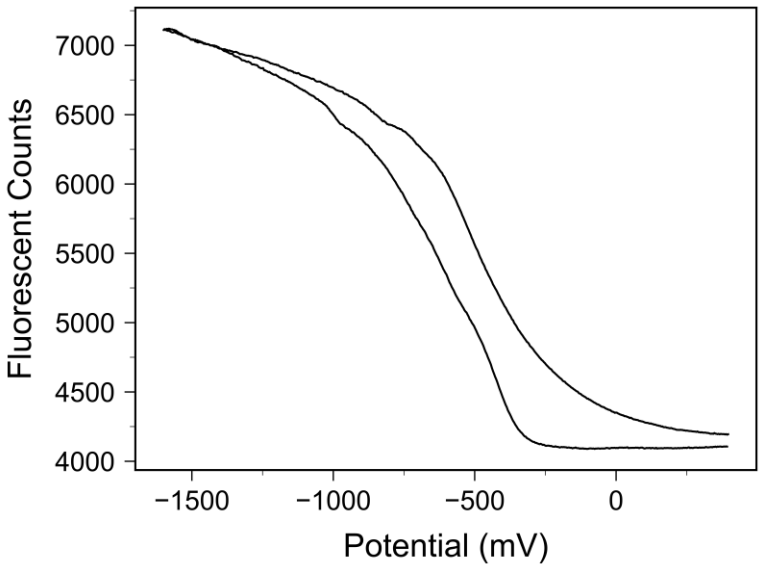

Figure 5.4. Experimental Diagram of Bipolar Ag NP Collisions Coupled to Resazurin Reduction.

The resazurin (Rz) pole is positioned on top of an inverted microscope to record the optical signal.

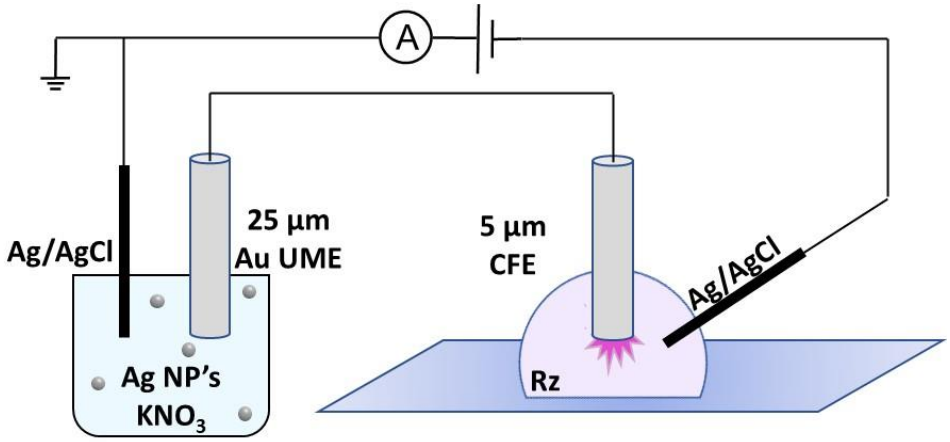

Figure 5.5. Correlated Optical-Electrochemical Responses for Bipolar Ag NP Collision Coupled to Resazurin Reduction.

A single electrochemical peak is highlighted, since it contained the largest integrated charge of 6000 fC (and therefore the best opportunity for observing correlated optical signal) amongst dozens that were recorded. Solution conditions consisted of 20 mM KNO_3 and ~30 pM Ag NP's on the detecting pole; and 50 µM Resazurin in 50 mM pH 7.4 PB on the reporting pole. 1 V was applied across the bipolar electrode.

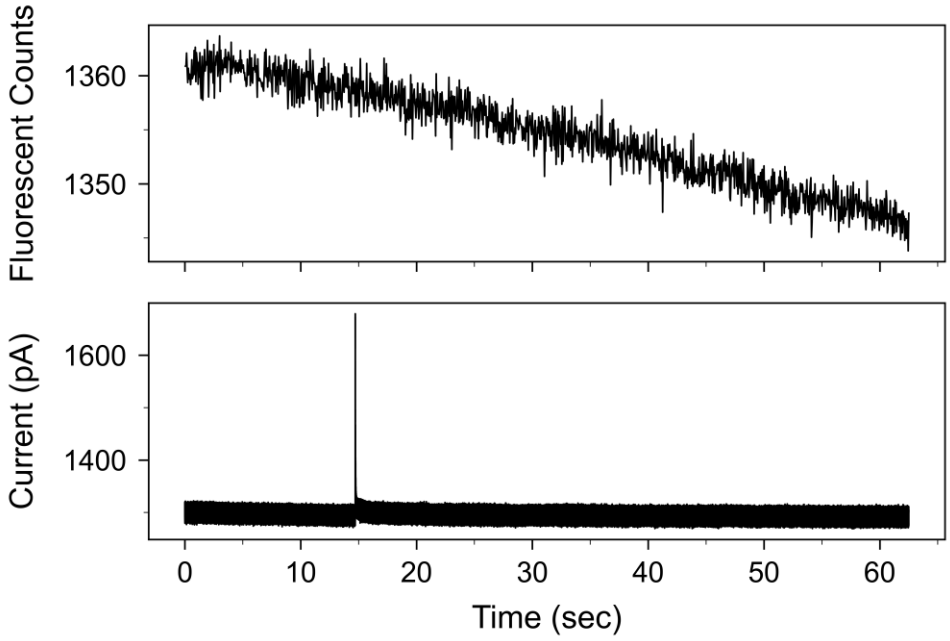

Figure 5.6. Correlated Electrochemical Bipolar Ag NP Collisions With and Without Resazurin.

(Top): Ag NP collisions with 20 mM KNO_3 and ~ 30 pM 60 nm Ag NP's are coupled to a solution of 50 µM Resazurin in 50 mM PB by applying 800 mV. Roughly the same electrochemical response is observed on the (Bottom), where resazurin is removed. Results indicate that another electron acceptor exists in the reporting solution, separate from resazurin.

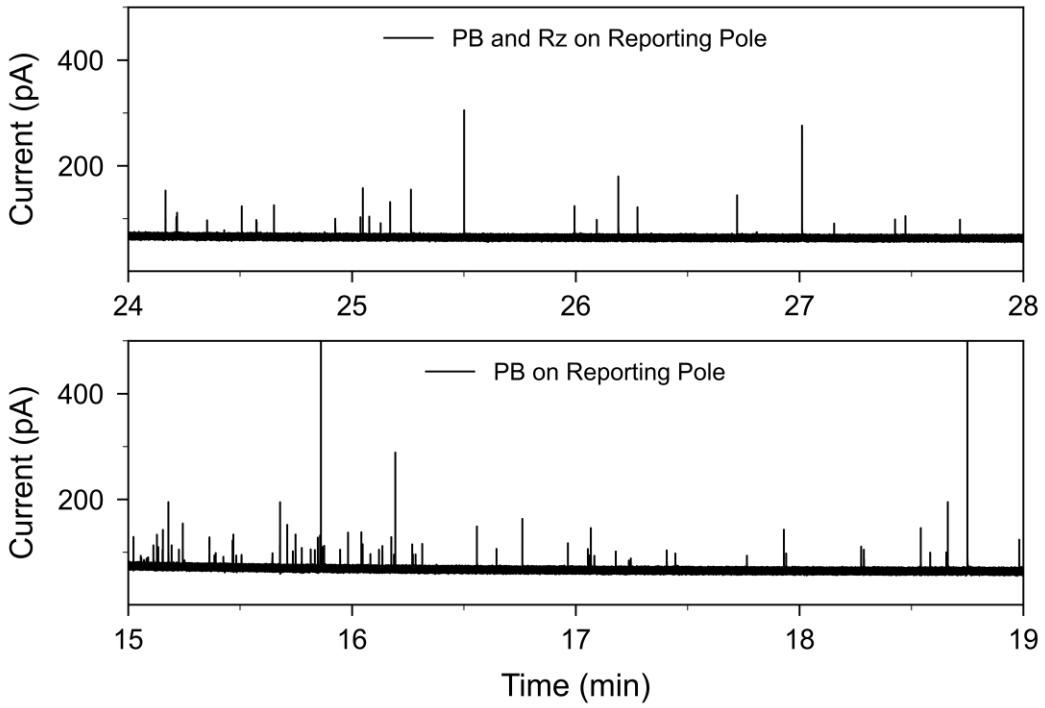

Figure 5.7. Correlated Electrochemical Bipolar Ag NP Collisions with Added Na_2SO_3.

(Top): Ag NP collisions with 20 mM KNO_3 and ~ 30 pM 60 nm Ag NP's are coupled to a solution of 3 mM Na_2SO_3 in 50 mM PB by applying 800 mV. The elimination of signal with addition of the oxygen scavenger (Na_2SO_3) suggests that dissolved O_2 is the mystery electron acceptor measured in the bottom of Figure 6. (Bottom): The same setup is employed except with the addition of 50 µM resazurin on the reporting pole. The re-addition of a reducible species recovers the Ag NP collision signal by allowing the reduction of resazurin.

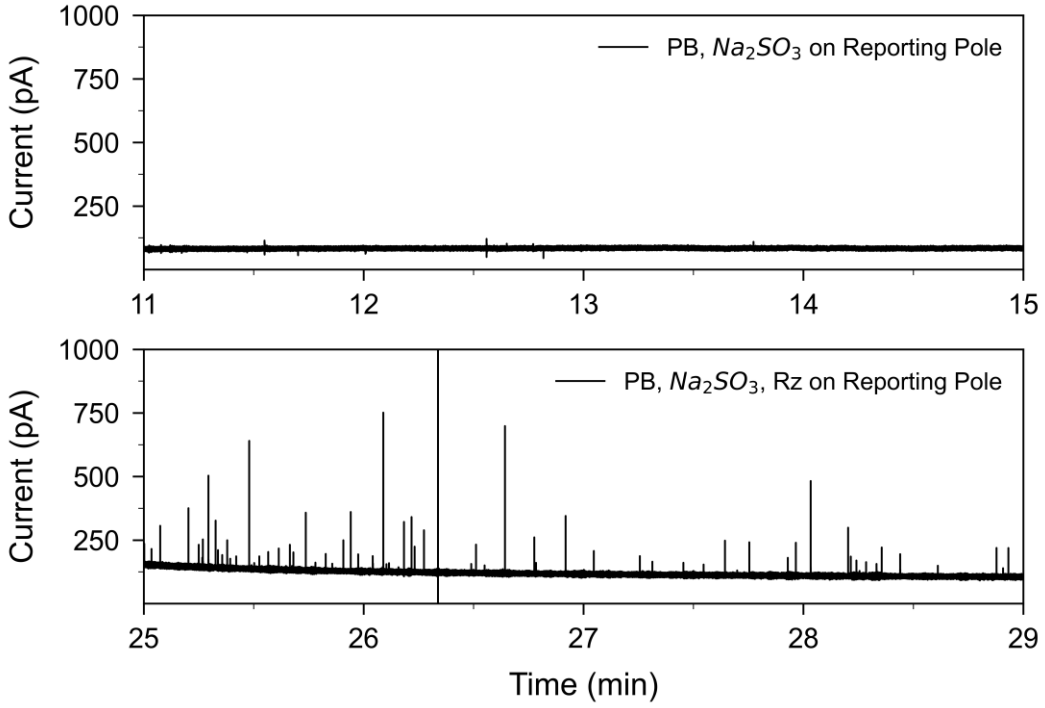

Figure 5.8. Airtight Imaging Chamber.

The pictured airtight chamber was utilized for experiments where resazurin was bubbled with nitrogen. The enclosed chamber prevented re-introduction of O_2 from the atmosphere. Resazurin solutions were purged with N_2 for 1 hour prior to experimentation.

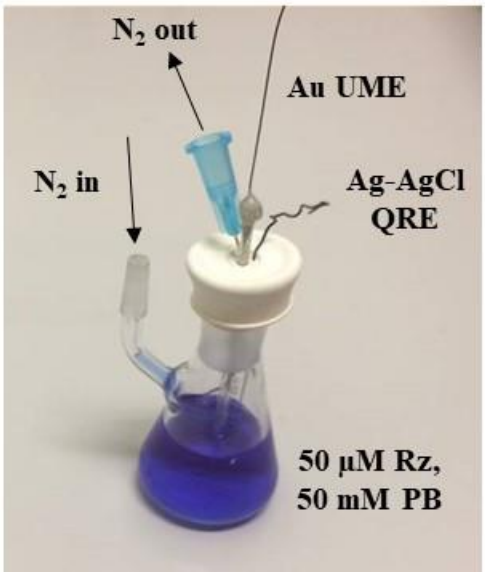

Figure 5.9. Correlated Optical Responses Comparing Ambient vs. N_2 Purged Resazurin at Constant Potential.

Display of the raw optical trace (top) and equivalent signal to noise ratio (bottom) for solutions containing ambient resazurin (A) and 1-hour N_2 purged resazurin (B) at a non-bipolar carbon fiber electrode held at -700 mV. Solutions consisted of 50 µM resazurin and 50 mM pH 7.4 PB.

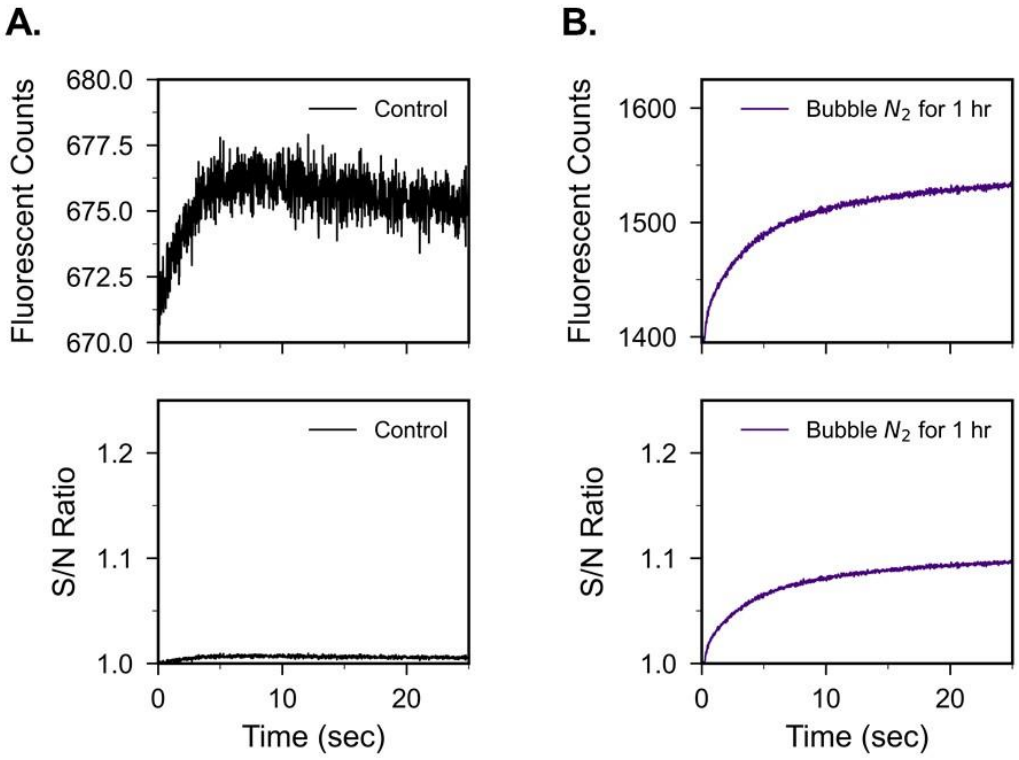

Figure 5.10. Correlated Optical-Electrochemical Responses for Bipolar Ag NP Collision Coupled to N_2-Purged Resazurin Reduction.

All coupled Ag NP collisions failed to produce measurable optical signal, despite the largest peak's integrated charge measuring 21650 fC. Solution conditions consisted of 20 mM KNO_3 and ~30 pM Ag NP's on the detecting pole; and 50 µM resazurin in 50 mM pH 7.4 PB with N_2 bubbled for 1 hour on the reporting pole. 1600 mV was applied across the bipolar electrode.

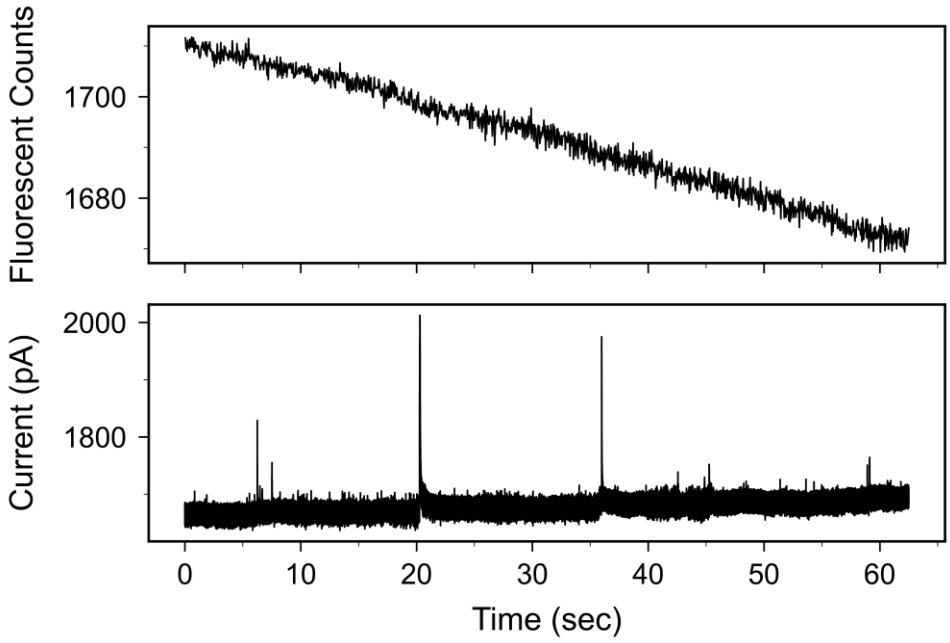

Figure 5.11. Experimental Diagram of Bipolar Pt NP Collisions Coupled to PH_2 Oxidation.

The dihydroresorufin (PH_2) pole is positioned on top of an inverted microscope to record the optical signal. Both bipolar electrode poles utilize 5 µm carbon fiber electrodes (CFEs).

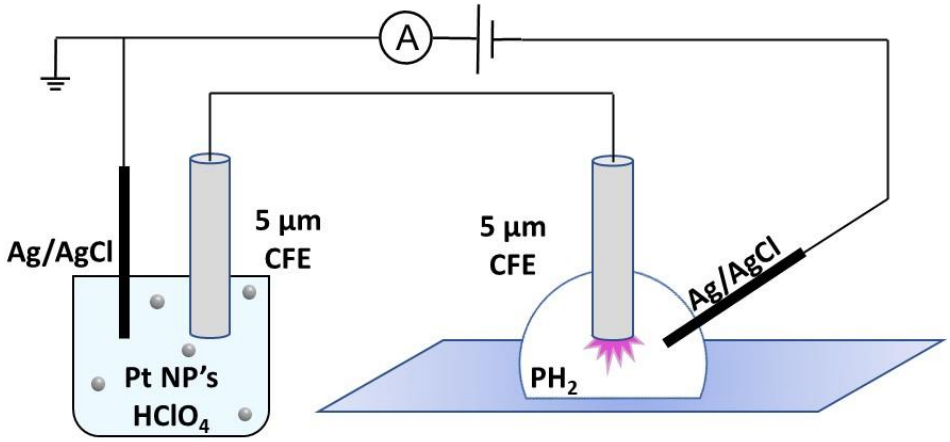

Figure 5.12. Correlated Optical-Electrochemical Bipolar Pt NP Collisions with PH_2.

Pt NP reductive collisions in 10 mM $HClO_4$ 20 mM $NaClO_4$ and ~ 300 pM 30 nm Pt NPs are coupled to a solution of 100 µM PH_2 67 mM Glucose 50 mM pH 7.4 PB by applying 300 mV. The (top) optical response matches quite well with the (bottom) electrochemical trace.

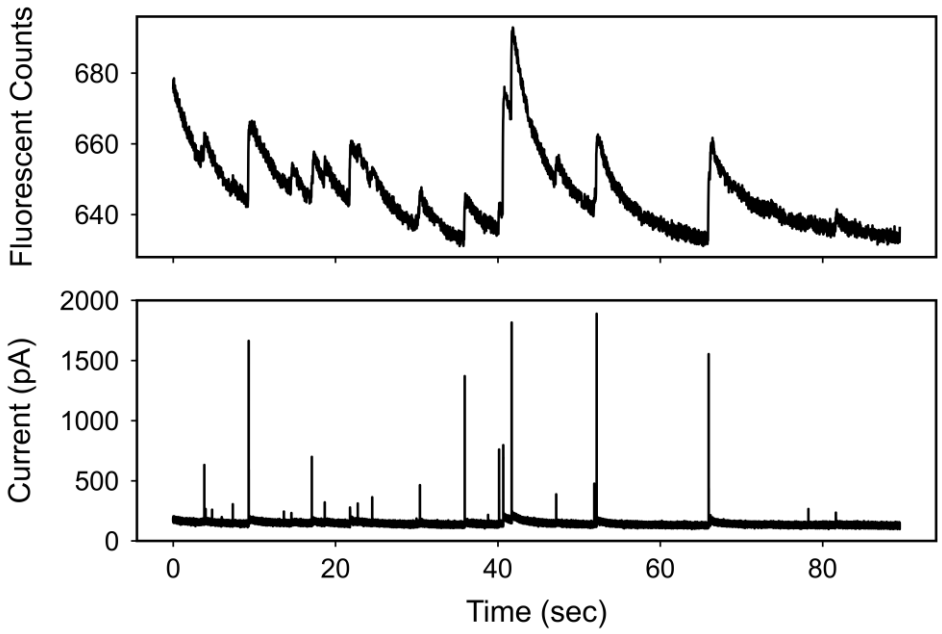

Figure 5.13. Comparison of Optical Cyclic Voltammograms for Fresh vs. Old $(NH_4)_2S_2O_8$.

Cyclic voltammograms were recorded using 1 mM $Ru(bpy)_3^{2+}$ 18 mM $(NH_4)_2S_2O_8$ 100 mM $TBAPF_6$ in 1:1 H_2O/AcN solvent. Conditions were identical except for the use of fresh vs. 1 year-old $(NH_4)_2S_2O_8$. A 99% decrease in optical signal is observed for the older chemical, highlighting the importance of this parameter.

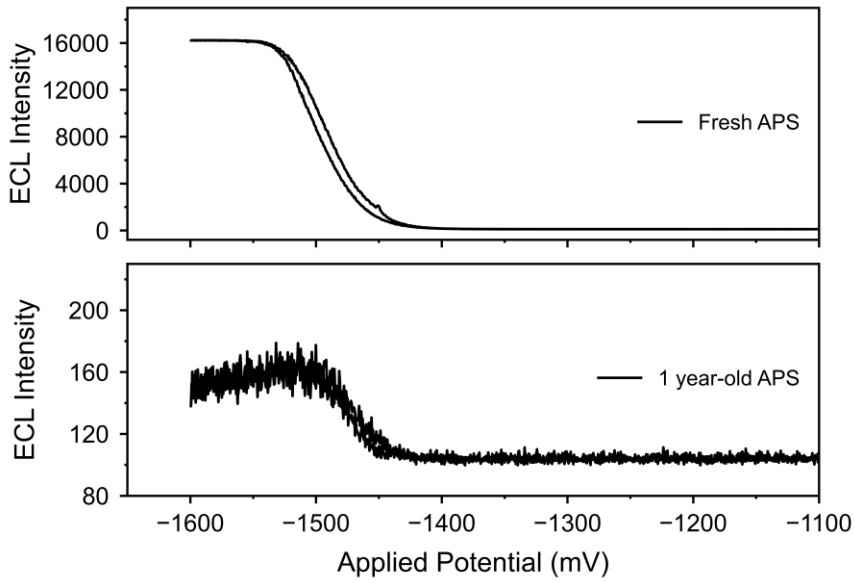

Figure 5.14. Correlated Optical-Electrochemical Cyclic Voltammogram for Cathodic ECL.

The cyclic voltammogram shows results for a non-bipolar electrode submerged in 1 mM $Ru(bpy)_3^{2+}$ 18 mM $(NH_4)_2S_2O_8$ with a solvent of 1:1 H_2O/AcN. (a-d) Show optical frames of the physical processes occurring during at four separate potentials (-1450 mV, -1580 mV, -1705 mV, -1875 mV). Notably, maximum light intensity only occurs in the potential window from -1580 mV to -1635 mV. A rapid decrease in signal intensity is caused by the electrodeposition and growth of Ruthenium wires.

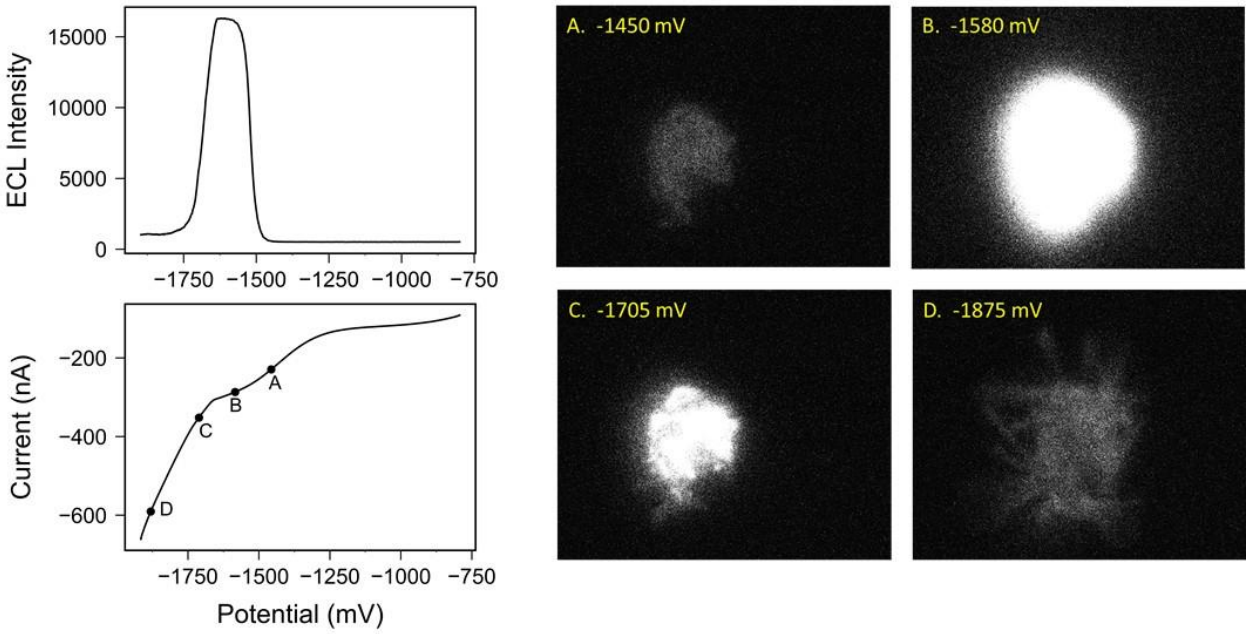

Figure 5.15. Correlated Optical-Electrochemical Cyclic Voltammogram for Anodic ECL.

The cyclic voltammogram shows results for a non-bipolar electrode submerged in 5 mM $Ru(bpy)_3^{2+}$ 20 mM DBAE. Notably, the optical signal maxes out from ~1050 mV to 1600 mV, suggesting that the optical intensity does not significantly decrease in this potential window.

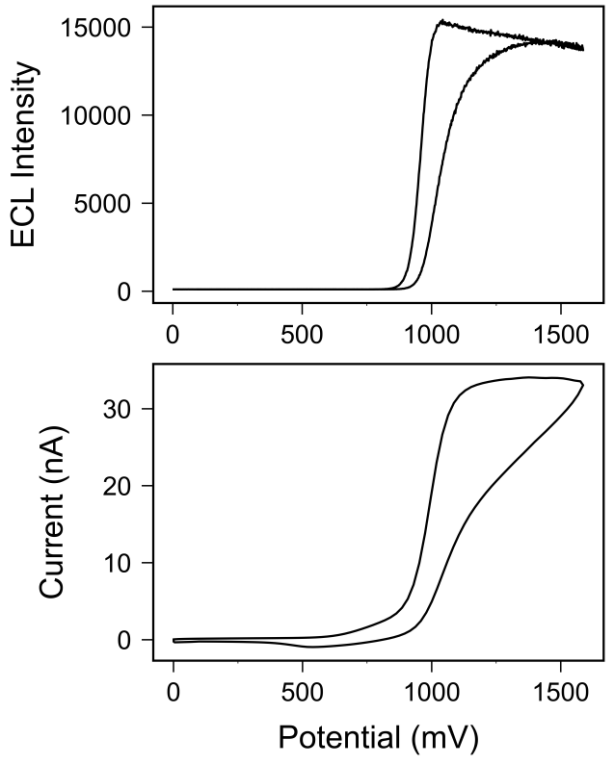

5.6 REFERENCES

(1) Guerrette, J. P.; Percival, S. J.; Zhang, B. Fluorescence Coupling for Direct Imaging of Electrocatalytic Heterogeneity. *J. Am. Chem. Soc.* **2013**, *135*, 855–861.

(2) Dunevall, J.; Majdi, S.; Larsson, A.; Ewing, A. Vesicle Impact Electrochemical Cytometry Compared to Amperometric Exocytosis Measurements. *Curr. Opin. Electrochem.* **2017**, *5* (1), 85–91.

(3) Travis, E. R.; Wightman, R. M. Spatio-Temporal Resolution of Exocytosis from Individual Cells. *Annu. Rev. Biophys. Biomol. Struct.* **1998**, *27*, 77–103.

(4) Kawagoe, K. T.; Jankowski, J. A.; Mark Wightman, R. Etched Carbon-Fiber Electrodes as Amperometric Detectors of Catecholamine Secretion from Isolated Biological Cells. *Anal. Chem.* **1991**, *63* (15), 1589–1594.

(5) Schroeder, T. J.; Jankowski, J. A.; Kawagoe, K. T.; Wightman, R. M.; Lefrou, C.; Amatore, C. Correction: Analysis of Diffusional Broadening of Vesicular Packets of Catecholamines Released from Biological Cells during Exocytosis. *Anal. Chem.* **1992**, *64*, 3077–6083.

(6) Jankowski, J. A.; Schroeder, T. J.; Ciolkowski, E. L.; Wightman, R. M. Temporal Characteristics of Quantal Secretion of Catecholamines from Adrenal Medullary Cells. *J. Biol. Chem.* **1993**, *268* (20), 14694–14700.

(7) Wightman, R. M.; Schroeder, T. J.; Finnegan, J. M.; Ciolkowski, E. L.; Pihel, K. Time Course of Release of Catecholamines from Individual Vesicles during Exocytosis at Adrenal Medullary Cells. *Biophys. J.* **1995**, *68* (1), 383–390.

(8) Omiatek, D. M.; Dong, Y.; Heien, M. L.; Ewing, A. G. Only a Fraction of Quantal Content Is Released During Exocytosis as Revealed by Electrochemical Cytometry of Secretory Vesicles. *ACS Chem. Neurosci.* **2010**, *1*, 234–245.

(9) Van Kempen, G. T. H.; Vanderleest, H. T.; Van Den Berg, R. J.; Eilers, P.; Westerink, R. H. S. Three Distinct Modes of Exocytosis Revealed by Amperometry in Neuroendocrine Cells. *Biophys. J.* **2011**, *100* (4), 968–977.

(10) Schroeder, T. J.; Jankowski, J. A.; Senyshyn, J.; Holz, R. W.; Wightman, R. M. Zones of Exocytotic Release on Bovine Adrenal Medullary Cells in Culture. *J. Biol. Chem.* **1994**, *269* (25), 17215–17220.

(11) Zhang, B.; Adams, K. L.; Luber, S. J.; Eves, D. J.; Heien, M. L.; Ewing, A. G. Spatially and Temporally Resolved Single-Cell Exocytosis Utilizing Individually Addressable Carbon Microelectrode Arrays. *Anal. Chem.* **2009**, *80* (5), 1394–1400.

(12) Wigström, J.; Dunevall, J.; Najafinobar, N.; Lovrić, J.; Wang, J.; Ewing, A. G.; Cans, A. S. Lithographic Microfabrication of a 16-Electrode Array on a Probe Tip for High Spatial Resolution Electrochemical Localization of Exocytosis. *Anal. Chem.* **2016**, *88*, 2080–2087.

(13) Wang, J.; Trouillon, R.; Dunevall, J.; Ewing, A. G. Spatial Resolution of Single-Cell Exocytosis by Microwell-Based Individually Addressable Thin Film Ultramicroelectrode Arrays. *Anal. Chem.* **2014**, *86*, 4515–4520.

(14) Yakushenko, A.; Kätelhön, E.; Wolfrum, B. Parallel On-Chip Analysis of Single Vesicle Neurotransmitter Release. *Anal. Chem.* **2013**, *85*, 5483–5490.

(15) Abbott, J.; Ye, T.; Krenek, K.; Qin, L.; Kim, Y.; Wu, W.; Gertner, R. S.; Park, H.; Ham, D. The Design of a CMOS Nanoelectrode Array with 4096 Current-Clamp/Voltage-Clamp Amplifiers for Intracellular Recording/Stimulation of Mammalian Neurons. *IEEE J. Solid-State Circuits* **2020**, *55* (9), 2567–2582.

(16) Obaid, A.; Hanna, M. E.; Wu, Y. W.; Kollo, M.; Racz, R.; Angle, M. R.; Müller, J.; Brackbill, N.; Wray, W.; Franke, F.; Chichilnisky, E. J.; Hierlemann, A.; Ding, J. B.; Schaefer, A. T.; Melosh, N. A. Massively Parallel Microwire Arrays Integrated with CMOS Chips for Neural Recording. *Sci. Adv.* **2020**, *6* (12).

(17) White, K. A.; Kim, B. N. Quantifying Neurotransmitter Secretion at Single-Vesicle Resolution Using High-Density Complementary Metal–Oxide–Semiconductor Electrode Array. *Nat. Commun.* **2021**, *12* (1), 1–8.

(18) Qin, X.; Li, Z.; Pan, J.; Li, J.; Wang, K.; Xia, X. Electrochemiluminescence Imaging the Hydrogen Evolution Reaction of Single Platinum Nanoparticles Using a Bipolar Nanoelectrode Array. *J. Electrochem.* **2021**, *27*, 157–167.

(19) Wightman, R. M.; Jankowski, J. A.; Kennedy, R. T.; Kawagoe, K. T.; Schroeder, T. J.; Leszczyszyn, D. J.; Near, J. A.; Diliberto, E. J.; Viveros, O. H. Temporally Resolved Catecholamine Spikes Correspond to Single Vesicle Release from Individual Chromaffin Cells. *Proc. Natl. Acad. Sci.* **1991**, *88*, 10754–10758.

(20) Staal, R. G. W.; Mosharov, E. V; Sulzer, D. Dopamine Neurons Release Transmitter via a Flickering Fusion Pore. *Nat. Neurosci.* **2004**, *7* (4), 341–346.

(21) Defnet, P. A.; Zhang, B. Detection of Transient Nanoparticle Collision Events Using Electrochemiluminescence on a Closed Bipolar Microelectrode. *ChemElectroChem* **2020**, *7*, 252–259.

(22) Oja, S. M.; Robinson, D. A.; Vitti, N. J.; Edwards, M. A.; Liu, Y.; White, H. S.; Zhang, B. Observation of Multipeak Collision Behavior during the Electro-Oxidation of Single Ag Nanoparticles. *J. Am. Chem. Soc.* **2017**, *139*, 708–718.

(23) Oja, S. M.; Guerrette, J. P.; David, M. R.; Zhang, B. Fluorescence-Enabled Electrochemical Microscopy with Dihydroresorufin as a Fluorogenic Indicator. *Anal. Chem.* **2014**, *86*, 6040–6048.

(24) Han, C.; Hao, R.; Fan, Y.; Edwards, M. A.; Gao, H.; Zhang, B. Observing Transient Bipolar Electrochemical Coupling on Single Nanoparticles Translocating through a Nanopore. *Langmuir* **2019**, *35* (22), 7180–7190.

(25) Truesdale, G. A.; Downing, A. L. Solubility of Oxygen in Water. *Nature* **1954**, *173*, 1236.

(26) Butler, I. B.; Schoonen, M. A. A.; Rickard, D. T. Removal of Dissolved Oxygen from Water: A Comparison of Four Common Techniques. *Talanta* **1994**, *41* (2), 211–215.

(27) Axelrod, D.; Burghardt, T. P.; Thompson, N. L. Total Internal Reflection Fluorescence. *Ann. Rev. Biophys. Bioeng.* **1984**, *13*, 247–268.

(28) Richter, M. M. Electrochemiluminescence (ECL). *Chem. Rev.* **2004**, *104* (3), 3003–3006.

(29) White, H. S.; Bard, A. J. Electrogenerated Chemiluminescence. 41. Electrogenerated Chemiluminescence and Chemiluminescence of the Ru(2,2′-bpy)$_3^{2+}$-$S_2O_8^{2-}$ System in Acetonitrile-Water Solutions. *J. Am. Chem. Soc.* **1982**, *104*, 6891–6895.

(30) Venkateswara Raju, C.; Senthil Kumar, S. Highly Sensitive Novel Cathodic Electrochemiluminescence of Tris(2,2′-Bipyridine)Ruthenium(II) Using Glutathione as a Co-Reactant. *Chem. Commun.* **2017**, *53* (49), 6593–6596.

(31) Choi, J. P.; Bard, A. J. Electrogenerated Chemiluminescence (ECL) 79. Reductive-Oxidation ECL of Tris(2,2′-Bipyridine)Ruthenium(II) Using Hydrogen Peroxide as a Coreactant in PH 7.5 Phosphate Buffer Solution. *Anal. Chim. Acta* **2005**, *541* (1–2), 143–150.

(32) Anderson, T. J.; Defnet, P. A.; Zhang, B. Electrochemiluminescence (ECL)-Based Electrochemical Imaging Using a Massive Array of Bipolar Ultramicroelectrodes. *Anal. Chem.* **2020**, *92*, 6748–6755.

(33) Li, X.; Majdi, S.; Dunevall, J.; Fathali, H.; Ewing, A. G. Quantitative Measurements of Transmitters in Vesicles One at a Time in Single Cell Cytoplasm with Nano-Tip Electrodes. *Angew Chem Int Ed Engl* **2015**, *54*, 11978–11982.

Chapter 6. EXPERIMENTAL DESIGN AND OPERATION OF BIPOLAR ECL IMAGING WITH MICROELECTRODE ARRAYS*

6.1 INTRODUCTION

Chapters 4 and 5 have focused on the development of closed-bipolar imaging toward the applications of transient measurements, and detection of oxidative species. These studies have relied on the use of single bipolar-microelectrodes, serving as both the detecting and optical-reporting poles. However, a notable advantage of bipolar imaging is its capacity to be seamlessly scaled using arrays containing thousands of bipolar electrodes to enable the spatial mapping of redox environments.

Bipolar electrode arrays are unique in their wireless design, whereby individual electrodes are embedded in an insulating membrane with exposed poles contacting the analyte or light-generating reactions on either side. The application of driving potential produces an equivalent potential drop at each individual electrode to couple complimentary half-reactions at either pole. The overall measured electrochemical current is a representative sum of all electrode reactions occurring simultaneously. However, individual electrode activities can be distinguished by monitoring the dynamics of the light-generating half-reaction output, using redox-mediated fluorescence or electrochemiluminescence.

It is advantageous to design bipolar arrays with small, densely packed electrode dimensions to improve the spatial resolution of the optical measurement. As a point of illustration, we can think of each electrode in the array as a pixel within a digital camera. Each pixel outputs a single

---

* This chapter is adapted with permission from:
Anderson, T. J.;‡ Defnet, P. A.;‡ Zhang, B. Electrochemiluminescence (ECL)-Based Electrochemical Imaging Using a Massive Array of Bipolar Ultramicroelectrodes. *Anal. Chem.* **2020**, *92*, 6748–6755. (‡ indicates equal contributions)

intensity value, and by itself is not so useful in accurately representing a scene. Yet shrinking the pixel size and densely packing thousands of them together allows for increased resolution of environmental features. Thus, we would equivalently obtain more accurate spatial details of measured redox environments with small densely packed electrode arrays.

The development of such arrays is facilitated using micro- and nano-fabrication technologies, enabling the precise control over electrode dimensions, and scalability within the confines of a silicon wafer. Yet, design approaches must still adhere to the immutable properties of materials science and physics. Shrinking feature sizes to the nanoscale dimension introduces unforeseen challenges of material stability and requires iterative development to ascertain a viable product.

Once a bipolar array is produced, therein lies the non-trivial task of developing an imaging protocol to enable its use. First, the experimentalist should hope that care was taken to design a system that is durable, since array imaging requires significant array handling. The utilization of thin, fragile silicon nitride windows prone to cracking, or thin polymeric membranes prone to tearing may not be practically useful, despite meeting all other fabrication goals. Second, we must consider the expected optical output. It is ideal for the intensity across each electrode to be separately interpretable. However, the overlapping diffusion layers of densely packed electrodes prevents the use of diffuse redox-mediated fluorophores due to signal overlap, as previously discussed in Chapter 1. Alternative imaging strategies utilize light-generation methodologies with short optical lifetimes, such as electrochemiluminescence (ECL)**,** or with the immobilization of solid-state electrochromic materials.[1] Lastly, optical sensitivity optimization should consider the desired temporal resolution due to their inverse proportionality, as discussed in Chapter 4.

Overall, we herein present the use of a massive array of microfabricated closed bipolar electrodes (BPEs) for imaging highly dynamic redox processes. This flexible BPE array is 1 × 1 cm^2 in size and is comprised of 146,522 8 μm-diameter carbon UMEs arranged in an ordered hexagonal lattice pattern with a 28 μm electrode spacing. The BPE array can be prepared with conventional microfabrication tools and has an electrode count over twice that of any individually addressable electrode array reported in the literature.[2–6] Using ECL as the reporter process (see Figure 6.1), the electrochemical signal can be optically recorded from all of the electrodes with a temporal resolution better than 30 ms. The use of ECL also improves the spatial resolution compared to a fluorescence-based scheme due to the absence of unhindered diffusion of the reporter species. To our knowledge, this is the first instance of ECL-based electrochemical imaging on very large, uniform BPE arrays; other array-based studies have reported a similar detection strategy but either do not focus on spatially resolving the source of the ECL signal[7–10] or are limited to a spatial resolution of ~0.5 mm.[11]

The work herein was performed in partnership with Todd J. Anderson (T.J.A.). Tasks were evenly divided between array fabrication (T.J.A.), and experimental use and data analysis (P.A.D.). The forthcoming sections will contain content for both halves of the project, as they appeared in literature.

6.2 EXPERIMENTAL

6.2.1 *Array Fabrication*

Microelectrode arrays were designed and fabricated by T.J.A, as described herein. A Si wafer (Silicon Valley Microelectronics) was cleaned by O_2 plasma (Glow Research) for 5 min (175 W, 1 Torr) and spin-coated with SU-8 2050 (MicroChem) photoresist (PR) to yield a 40 μm

thick film. The PR film was baked at 65 °C for 3 min and 95 °C for 6 min followed by selective exposure on a mask aligner (ABM-USA). The exposed wafer was then subjected to stress reduction (1 min at 65 °C) and postexposure baking (6 min at 95 °C). The PR film was then developed in SU-8 developer (MicroChem) for 5 min and rinsed with developer, isopropanol, and DI water before being spun dry.

The SU-8-patterned wafer was diced into ~2 × 2 cm^2 chips and hard baked in a tube furnace (Thermo Scientific) for 40 min at 300 °C under N_2 flow, after which the temperature was increased to 900 °C for 1 h. The furnace was left closed until it had returned to room temperature. Following pyrolysis, 20 μm of Parylene C was deposited over the patterned chips with a Labcoter 2 system (Specialty Coating Systems) at 175 and 690 °C for the vaporizer and pyrolysis furnaces, respectively, and a chamber pressure of 35 mTorr. The Parylene C films were annealed for 2 h at 400 °C under N_2. A PlasmaLab 100 ICP etcher (Oxford Instruments) was used to expose the pyrolyzed carbon structures through the overlying Parylene. The processed Parylene films were released from Si by overnight immersion in 1 M KOH at 100 °C.

6.2.2 *Array Preparation for Imaging*

A plastic well was epoxied to the array surface for containment of the top analyte solution. The well was prepared by cutting a 15 mm section from the wide end of a 1 mL pipet tip and attaching it to the array. The ECL solution below the array was contained on the microscope stage using a home-built device fabricated from three 1.0 mm thick glass slides (VWR). One slide was used as the base and two were positioned laterally about 1 cm apart, creating a 1 mm deep channel for ECL solution containment. Epoxy was used to prevent solution leakage.

6.2.3 *Bipolar Imaging*

Potential was driven across the array using a 3-electrode CV-27 potentiostat (BAS) with three Ag/AgCl electrodes. Two electrodes were placed in the bottom ECL solution, and one was placed in the top solution. Wires were freshly chlorided prior to each experiment using a 1:1 solution of 70% HNO_3 and 3 M KCl. The ECL-cyclic voltammogram (ECL-CV) and redox puffing experiments were recorded on an Andor iXon 897E EMCCD camera cooled to −80 °C with 30 ms exposure, 300 EM Gain, 5.1x preamplifier gain, 0.3 µs vertical pixel shift speed, and 10 MHz readout rate. Videos contained 1500 frames with 512 × 512 pixels. An Olympus IX70 microscope equipped with a 4x (0.1 NA Olympus Plan N) objective was used to image the array. Each pixel measured 3.92 µm, yielding a 4.0 × 106 μm^2 field of view and allowing 6005 full electrodes in each frame.

The generator-collector and depletion zone imaging experiments were recorded using an Andor Luca S 658 M EMCCD cooled to −20 °C with 30 ms exposure, 0.6 µs vertical pixel shift speed, and 13.5 MHz readout rate. Videos contained 1500 frames with 658 × 496 pixels. The same IX70 microscope and 4x objective were used. Each pixel measured 1.03 µm, yielding a 3.5 x 105 μm^2 field of view and allowing 507 full electrodes to be viewed in each frame. All videos were analyzed using ImageJ.

An optically correlated bipolar CV was driven between 100 mM $Fe(CN)_6^{3-}$ 100 mM KCl solution on top of the array and 25 mM $Ru(bpy)_3^{2+}$ 20 mM DBAE 100 mM phosphate buffer (PB) pH 7.4 below the array. Potential was scanned from 0 to +2.8 to 0 V vs Ag/AgCl at 200 mV/s using a CV-27 potentiostat. The current−potential (*i*-*V*) trace was recorded using a LabVIEW 2013 program, while the ECL intensity-potential ($I_{ECL}-V$) trace was simultaneously monitored using conditions described above.

In the generator-collector experiment, a 12.7 μm diameter Au UME was positioned using a Sutter MP-225 micromanipulator in 50 mM $Fe(CN)_6^{4-}$ 1 M KCl solution ~100 μm above the array surface. A 0.8 V potential was applied on the Au UME vs Ag/AgCl to generate $Fe(CN)_6^{3-}$ at the electrode surface. The $Fe(CN)_6^{3-}$ then diffused to the array surface, which was biased at +2.0 V and underwent electrochemical reduction by coupling to anodic ECL across each closed-bipolar electrode. The solution used in the ECL experiment was 5 mM $Ru(bpy)_3^{2+}$ 20 mM DBAE 100 mM PB pH 7.4.

To image the depletion zone, a similar procedure was followed as for the above generator-collector experiment. Important differences include the use of a 50 μm Au UME as the generator electrode and maintaining a stationary electrode position throughout the experiment. The Au electrodes for both experiments were fabricated by sealing a piece of Au wire in a glass capillary.[12] Electrodes were characterized using cyclic voltammetry in 1 mM FcMeOH 100 mM KCl solution.

For the redox concentration mapping experiment, a pulled glass micropipette[13] with a 10 μm orifice was immersed in 100 mM KCl solution and was used to inject 100 mM $Fe(CN)_6^{3-}$ 100 mM KCl solution orthogonally onto the array surface. An Eppendorf Femtojet was used to apply constant injection pressures for a controlled period ranging from 1 to 10 s with pressures ranging from 0.5 to 2 PSI. The micropipette was placed ~100 μm above the array surface and remained at a constant distance for the duration of the experiment. Following each stimulation, $Fe(CN)_6^{3-}$ was reduced across the array surface, which was coupled to an anodic ECL process to generate an optical output. A 2.8 V potential was applied across the array to drive the bipolar reaction. The solution used in the ECL experiment consisted of 25 mM $Ru(bpy)_3^{2+}$ 20 mM DBAE 100 mM PB at pH 7.4.

6.3 Results and Discussion

6.3.1 *Fabrication of Bipolar UME Arrays*

A bottom-up process was developed to fabricate the BPE arrays. As summarized in Figure 6.2, our method involves making a large, uniform array of carbon UMEs on a Si substrate, insulating it in a thin Parylene film, and exfoliating the array from the substrate. Several key factors need to be considered. First, since the array resolution is limited by the electrode size and spacing, closely spaced UMEs are desirable to attain maximum density. The insulating film must also be robust and continuous to prevent passage of ionic current. Lastly, the device must be as thin as possible to minimize electrical discontinuities which could arise from high aspect ratio electrode geometries. We adapted a procedure from Wang et al.[14] to generate large arrays of carbon micropillars. A high-temperature pyrolysis process turns an array of SU-8 micropillars into an array of conductive carbon posts. Note from Figure 6.3a,b, however, that the height and diameter of each micropillar is reduced by a factor of 2 during pyrolysis. This volume loss plays a role in determining the final device thickness and must be considered by selecting an SU-8 thickness twice that of the desired micropillar height.

The carbon array was insulated by Parylene C, a flexible coating widely used in the electronics industry[15–17] due to its excellent electrical properties and chemical resistance. A continuous film may be formed about the carbon micropillars once sufficient growth has occurred on their sidewalls (Figure 6.3c). The SU-8 precursor structures were hexagonally arranged to minimize both the edge-to-edge electrode spacing and, by extension, the thickness of Parylene C required to form a continuous film. The use of a hexagonal lattice arrangement also resulted in a 15% increase in electrode density compared to a square lattice.

We used thermal annealing to prevent stress fractures in the free-standing membranes after exfoliation. This annealing process increases the tensile strength and elongation-at-break of the Parylene film. Melting and reflowing of the Parylene also renders the substance amorphous and serves to seal any unfilled voids which would result in the passage of ionic current through the insulating layer during device operation. We used O_2 plasma etching to expose the upper carbon surfaces (Figure 6.3d). A hot KOH solution was used to dissolve the Si and free the devices. No degradation or etching of the Parylene or electrodes was observed. Note the uniformity of the electrodes and absence of defects shown in Figure 6.3e,f. A finished device is pictured in Figure 6.3g.

6.3.2 *Electrochemical Imaging*

Electrochemical imaging experiments were performed to characterize the array's response dynamics, as well as to explore a previously unreported imaging application. Four unique experiments are described along with their independent analyses. We quantify the homogeneity of the ECL response across each array electrode, provide proof for the absence of cross talk, demonstrate the capacity to image variable redox concentrations, and explore the generation of depletion zones in confined spaces using a generator-collector apparatus. Overall, we aim to highlight the excellent performance and broad applicability of our newly fabricated closed-bipolar array for electrochemical imaging.

We first investigated the homogeneity of the ECL intensity (I_{ECL}) on the array by performing a correlated ECL-CV. Here, bulk 100 mM $Fe(CN)_6^{3-}$ is placed on top of the array and coupled to anodic ECL solution below the array by reversibly scanning the potential from 0 to 2.8 V, as shown in Figure 6.4a. Both electrochemical ($i-V$) and optical ($I_{ECL}-V$) voltammograms were plotted in Figure 6.4b. The two signals match well in their overall shape, where both onset

potentials begin at ~1.1 V and approach a maximum value at ~2.1 V. Interestingly, the I_{ECL} begins to decrease despite increasing the potential at 2.3 V, possibly due to interference from other redox reactions such as water oxidation. In Figure 6.4c we observe the optical response of a ~300-electrode subset of the array during the potential scan. We observe that the I_{ECL} at each electrode is indeed uniform relative to its adjacent electrode neighbors.

We next aimed to determine if crosstalk (electron transfer between neighboring electrodes) was occurring since it has been reported for previous closed-bipolar array fabrication schemes.[18] Elimination of crosstalk is important to ensure single-electrode spatial resolution. We investigated this behavior by using a generator-collector setup as shown in Figure 6.5a, similar to the setup used in our previous work.[19] Here, a 12.7 μm Au UME was positioned ~100 μm above the array surface in a 50 mM $Fe(CN)_6^{4-}$ solution. A +0.8 V potential was applied to the Au UME, producing $Fe(CN)_6^{3-}$ which diffused toward the array. The diffusion layer was optically detected across the biased (+2 V) bipolar array by coupling to anodic ECL.

Upon activation of the generator electrode, a 3-electrode cluster in the array was immediately illuminated by ECL. The generator electrode was then moved laterally across the array with a micropositioner and the corresponding array illumination precisely followed its movement with no perceptible lag. Figure 6.5b displays four illuminated positions. This result suggests that the relatively constant size of the diffusion layer was uniformly detected. If crosstalk were present, we would expect to observe overlap of the signal from neighboring electrodes. While it is possible for toppling of the electrodes to occur prior to Parylene deposition, these occurrences are easily observable and may be screened out during the fabrication process. Nonetheless, we verified that the arrays were absent from crosstalk by scanning the generator electrode across thousands of other array electrodes in subsequent experiments.

We next aimed to explore our capacity to map variable redox concentrations across a wide area. Here, we positioned a micropipette filled with 100 mM $Fe(CN)_6^{3-}$ ~100 µm away from the array, as shown in Figure 6.6a. A pressure-injection module was used to dispense the $Fe(CN)_6^{3-}$ at pressures between 0.5 and 2 PSI and durations from 1 to 10 s. Reduction of $Fe(CN)_6^{3-}$ was coupled to anodic ECL across the bipolar array electrodes which were driven by a +2.8 V bias voltage. In Figure 6.6b we show an example $Fe(CN)_6^{3-}$ injection time lapse using 2 PSI for 5 s. Variations in ECL intensity and illuminated regions are observed depending on the time point during the injection. The illumination zone begins as a ~150 µm diameter cluster at 0.09 s and grows in area until the pressure is turned off at 5 s, resulting in a zone diameter of ~1 mm. After the pressure is turned off, the intensity gradually fades due to decreased $Fe(CN)_6^{3-}$ convection paired with dilution by the bulk KCl solution. Under constant potential, the I_{ECL} fluctuations must be due to local changes in $Fe(CN)_6^{3-}$ concentration. In Figure 6.6b we observe higher $Fe(CN)_6^{3-}$ concentrations near the center of the plume during the injection period which implies a faster convective flow velocity. This is in good agreement with simulations of convective flow profiles from a micropipette by Unwin and co-workers.[20–22]

Figure 6.6c compares the maximum intensities from 12 puffing experiments using the annotated injection pressure and duration conditions. We observe that a high pressure and short duration (2 PSI, 0.5 s) more effectively delivers $Fe(CN)_6^{3-}$ to the array compared to a low pressure over a long duration (0.5 PSI, 10 s). This effect can be attributed to increased convective mass transfer at higher pressures, thereby displacing more KCl solution from the array surface.[21] Overall, these results demonstrate that we can map changing redox concentrations during dynamic time-resolved redox processes.

We last examined the time-resolved formation of a redox depletion zone from a generator-collector setup in a confined space. The experiment used a setup similar to the one shown in Figure 6.5. A major difference was the use of a larger 50 μm Au UME with a 2 mm glass sheath held at a fixed position ~100 μm above the array. An oxidizing potential of +0.8 V was applied to the Au UME to generate $Fe(CN)_6^{3-}$ via $Fe(CN)_6^{4-}$ oxidation which then diffused to the array surface. The diffusion layer was optically probed on the bipolar array by coupling $Fe(CN)_6^{3-}$ reduction to the anodic ECL.

Interestingly, we observed a starkly different behavior than in Figure 6.5. A larger illumination zone was immediately detected which was indicative of the larger diffusion layer about the 50 μm Au UME. This illuminated area grew to ~400 μm over the first 2 s, with greater ECL intensity being observed near the center than at the edges. However, beginning at 3 s, the center of the illumination began to steadily decrease in intensity until a dark depletion zone was formed directly beneath the Au UME position. Over time, both the illumination and depletion regions pushed further outward away from the original Au UME location.

We believe the formation of the depletion zone is due to a multistep interaction between the mass transfer at the Au UME and array electrodes, as illustrated in Figure 6.7a. An initial oxidation of 50 mM $Fe(CN)_6^{4-}$ near the Au UME generates $Fe(CN)_6^{3-}$ which diffuses radially outward. Hindered diffusion due to confinement in the ~100 μm microgap steadily decreases the available $Fe(CN)_6^{4-}$ at the UME surface. While $Fe(CN)_6^{4-}$ may continue to diffuse to the UME from the sides, the center region directly beneath the UME can no longer receive $Fe(CN)_6^{4-}$. Therefore, less and less $Fe(CN)_6^{3-}$ could be generated from this region leading to the formation of the observed depletion zone, which is shown in panels 2−6 in Figure 6.7b.

In Figure 6.7c we support this mechanism by creating a heatmap that illustrates how the ECL intensity of the selected area changes over the recording duration. Importantly, the heatmap indicates that both the diffusion layer and depletion zones grow radially outward at the same rate as evidenced by the steady thickness of the I_{ECL} ring. This observation suggests that both regions are controlled by the same diffusion-limited mass transfer process and are likely emanating from the same UME point source. Consequently, we expect the size of the depletion zone to be directly influenced by the diameter of the generating UME. Overall, these results demonstrate the excellent electrochemical imaging capacity of our bipolar array for dynamic time-resolved processes.

6.4 CONCLUSION

In summary, we have successfully fabricated uniform, massive arrays of carbon bipolar UMEs using a reproducible microfabrication procedure. This process uses carbon pyrolysis and Parylene deposition to yield an ultrathin freestanding Parylene film containing >140,000 highly uniform bipolar carbon UMEs. These arrays have been used to study several dynamic processes, including tracing the motion of an Au UME, imaging the pressure-driven flow of redox species from a micropipette, and characterizing the generation, diffusion, and depletion of $Fe(CN)_6^{3-}$ on an Au UME. The spatial resolution was found to be limited by the size of the bipolar UMEs and their spacing, which can be further improved by reducing the electrode dimensions and the interelectrode spacing. The temporal resolution, on the other hand, is limited only by the data transfer rate of the camera. Our results have further confirmed that microfabricated UME arrays are uniquely suited to imaging fast and dynamic redox processes. Further efforts are ongoing in our lab toward the fabrication of viable nanoelectrode arrays, and their use for imaging biological systems.

6.5 FIGURES

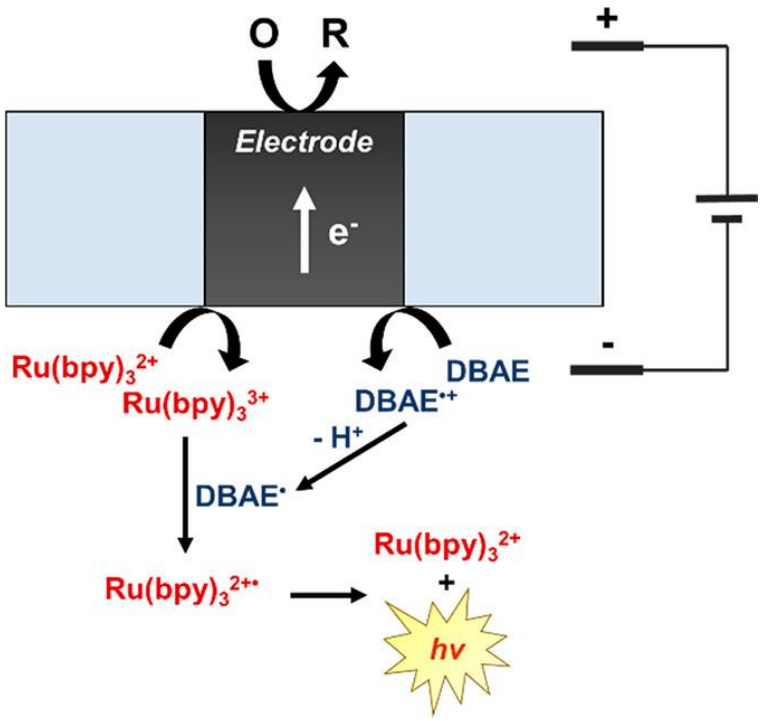

Figure 6.1. Reaction Scheme for Bipolar Anodic ECL Imaging.

Diagram of a Reduction Reaction Coupled to a $Ru(bpy)_3^{2+}$-Based ECL System with a 2-(dibutylamino)ethanol (DBAE) Co-reactant Across a Closed Bipolar Electrode

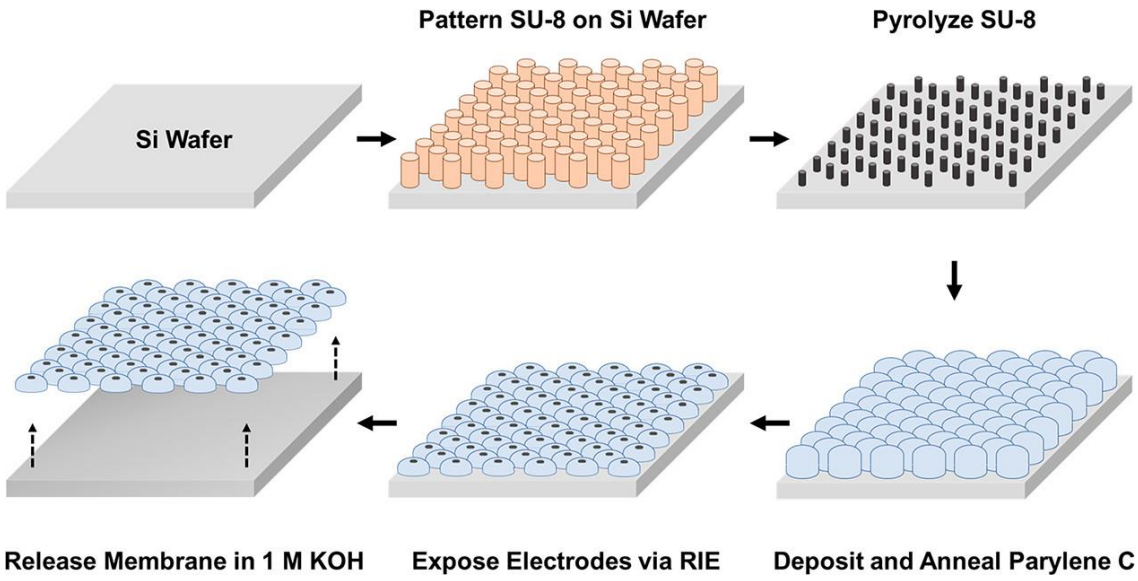

Figure 6.2. Flowchart Illustrating Bipolar Electrode Array Fabrication Process.
Note that feature sizes are drawn to scale relative to each other.

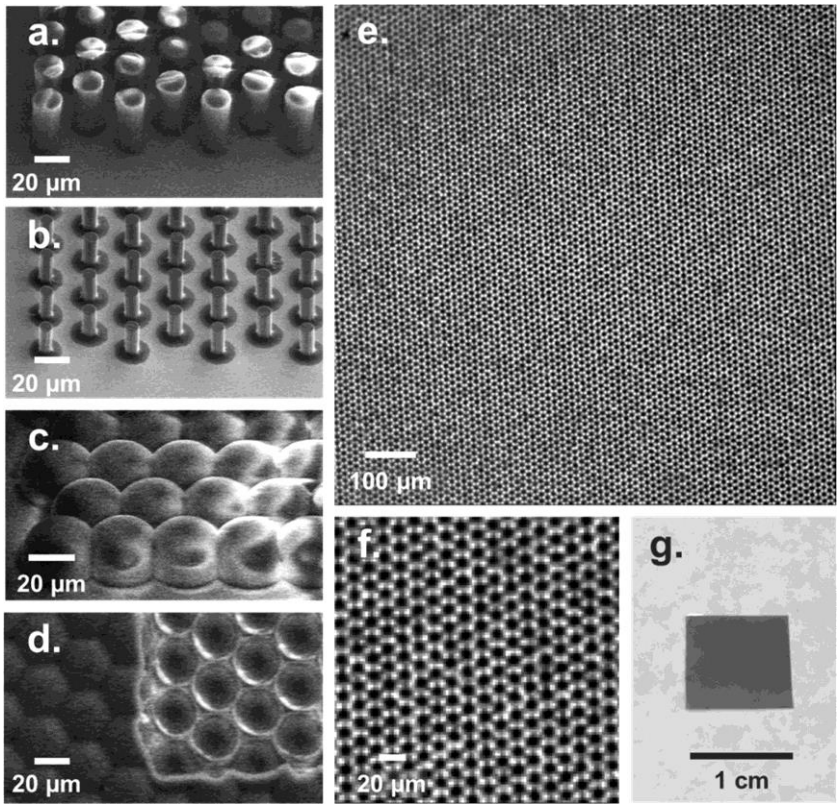

Figure 6.3. High-Resolution Images of Electrode Array.

(a) SEM images of SU-8 micropillars (18 µm diameter, 40 µm height) on Si, (b) pyrolytic carbon micropillars (8 µm diameter, 18 µm height), (c) carbon micropillars coated in a 20 µm Parylene C film, and (d) a portion of the pyrolytic carbon micropillars exposed. (e) Brightfield optical micrograph of the reporting surface of the array. (f) Close-up view of the array surface. (g) Photograph of a freestanding bipolar UME array.

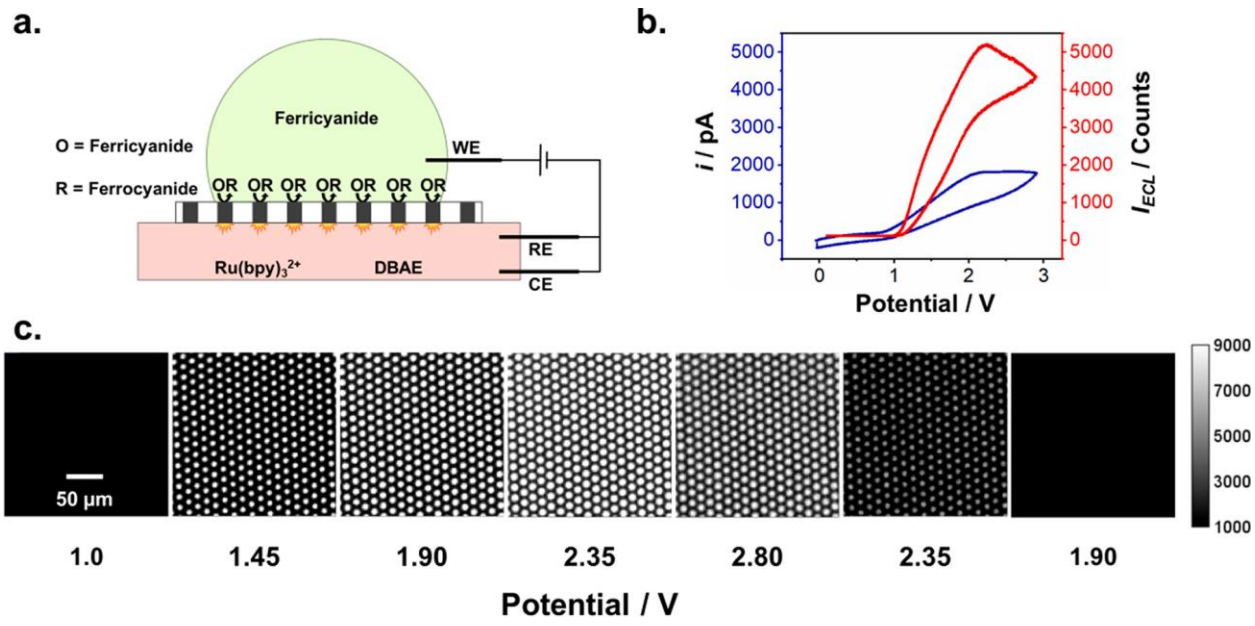

Figure 6.4. Correlated Optical and Electrochemical Cyclic Voltammetry.

(a) Schematic of an ECL-CV coupling 100 mM $Fe(CN)_6^{3-}$ to anodic ECL across the bipolar array. Potential was swept from 0 to 2.8 to 0 V at 200 mV/s. (b) Correlation of the electrochemical ($i-V$) and optical ($I_{ECL}-V$) signals. The *i-V* signal is representative of the whole array, while the optical signal was averaged across a ~300 electrode subset, including the inactive substrate between electrodes. (c) ECL response from a ~300 electrode subset demonstrating the homogeneity of the I_{ECL} at each electrode for the described potentials.

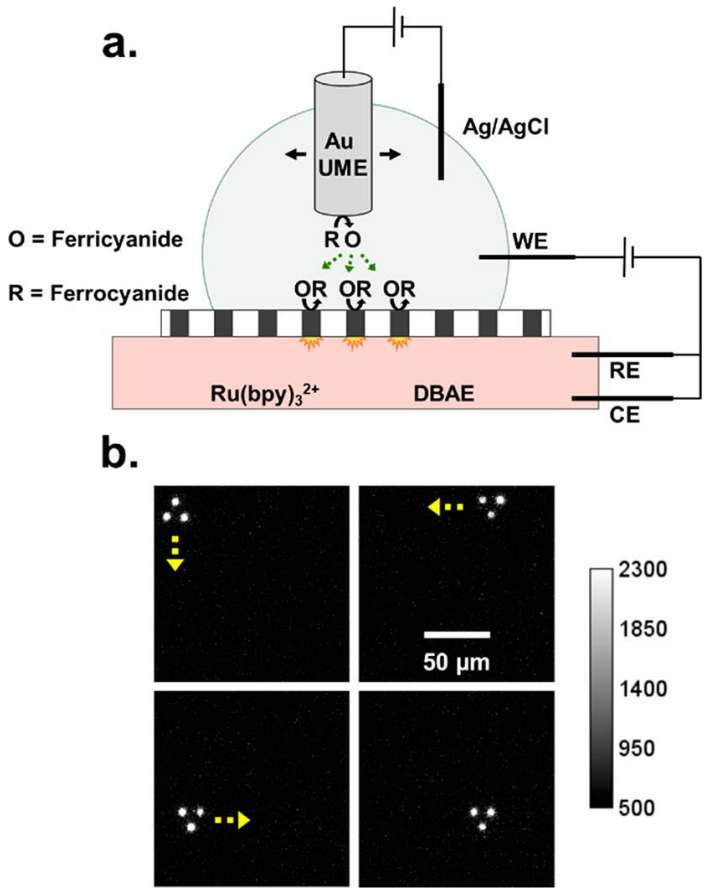

Figure 6.5. Generator-Collector Imaging of Ferricyanide Diffusion Layer.

(a) Schematic showing the anodic ECL detection of a diffusion layer on an UME. $Fe(CN)_6^{4-}$ is oxidized on a 12.7 µm Au UME at +0.8 V to produce $Fe(CN)_6^{3-}$.The incident $Fe(CN)_6^{3-}$ on the array is detected by ECL at +2.0 V bias voltage. As the UME is moved laterally across the array, the detected diffusion layer precisely follows the UME movement. (b) Optical frames displaying the UME's diffusion layer movement.

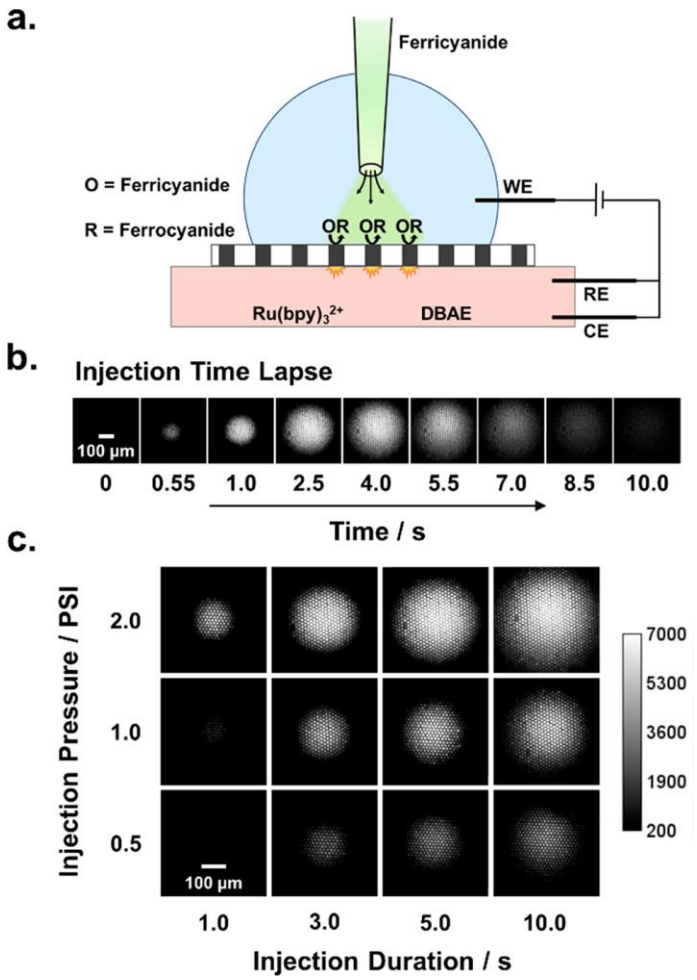

Figure 6.6. Imaging the Injection of Ferricyanide onto the Array.

(a) Schematic displaying the injection of $Fe(CN)_6^{3-}$ from a micropipette onto the array. $Fe(CN)_6^{3-}$ was detected by coupling to anodic ECL across the biased bipolar array (+2.0 V). (b) Time-lapse images of a single injection using 2 PSI for 5 s. The variable ECL intensities are due to the detected heterogeneity in $Fe(CN)_6^{3-}$ concentration. (c) Maximum intensity frames collected during 12 independent injection experiments using the described injection pressure and duration conditions. The calibration bar to the right of (c) describes the ECL intensity for panels b and c.

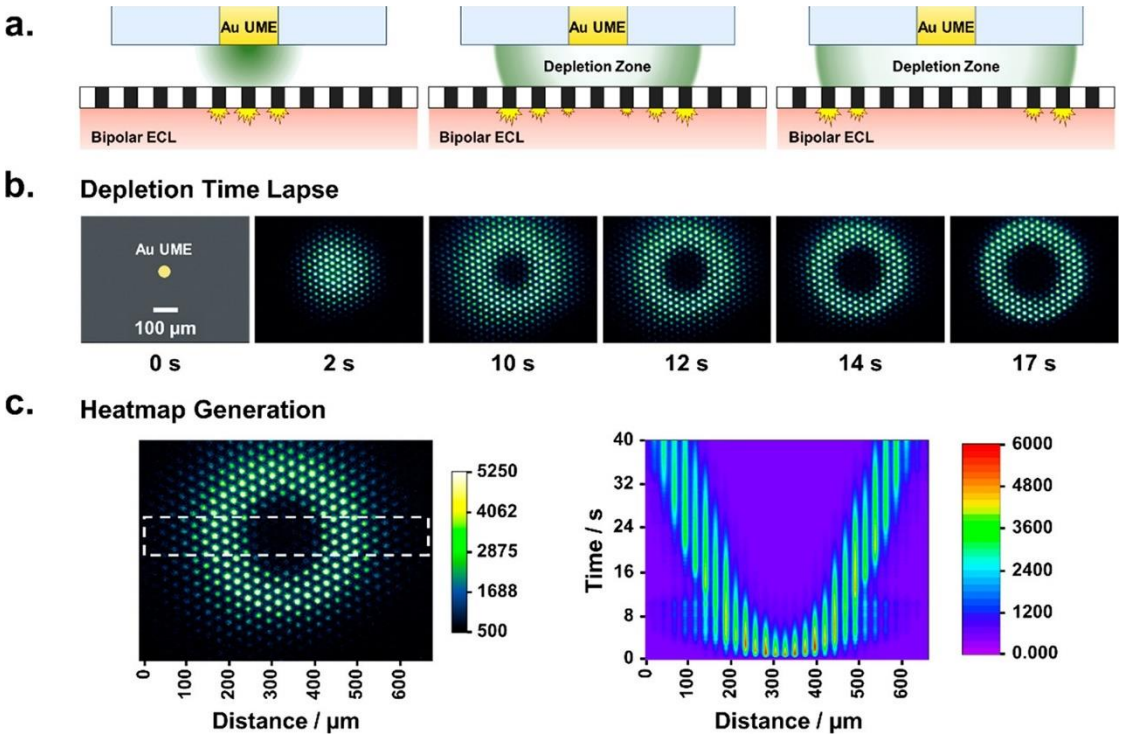

Figure 6.7. Imaging the Depletion Zone Formation in a Thin Electrochemical Cell.

(a) Schematic showing the formation of a depletion zone in a generator-collector setup. $Fe(CN)_6^{4-}$ is oxidized on a 50 µm Au UME generating $Fe(CN)_6^{3-}$.The incident $Fe(CN)_6^{3-}$ on the biased array (+2.0 V) is visually detected by anodic ECL. A dark redox depletion zone is formed due to the consumption of $Fe(CN)_6^{4-}$ in the ~100 µm microgap between the UME and array. (b) Progression of the ECL response during the depletion time lapse. (c) Heatmap generated using the section of the array enclosed in the dotted white box on the left. The result on the right shows the average intensity at each distance within the selected region for the duration of the video. The calibration bars on the left and right of the heatmap are both in units of I_{ECL}.

6.6 REFERENCES

(1) Wei, H.; Wang, E. Solid-State Electrochemiluminescence of Tris(2,2′-Bipyridyl) Ruthenium. *TrAC - Trends Anal. Chem.* **2008**, *27*, 447–459.

(2) Wydallis, J. B.; Feeny, R. M.; Wilson, W.; Kern, T.; Chen, T.; Tobet, S.; Reynolds, M. M.; Henry, C. S. Spatiotemporal Norepinephrine Mapping Using a High-Density CMOS Microelectrode Array. *Lab Chip.* **2015**, *15*, 4075–4082.

(3) Dragas, J.; Viswam, V.; Shadmani, A.; Chen, Y.; Bounik, R.; Stettler, A.; Radivojevic, M.; Geissler, S.; Obien, M. E. J.; Müller, J.; Hierlemann, A. In Vitro Multi-Functional Microelectrode Array Featuring 59 760 Electrodes, 2048 Electrophysiology Channels, Stimulation, Impedance Measurement, and Neurotransmitter Detection Channels. *IEEE J. Solid-State Circuits.* **2017**, *52*, 1576–1590.

(4) Tedjo, W.; Nejad, J. E.; Feeny, R.; Yang, L.; Henry, C. S.; Tobet, S.; Chen, T. Electrochemical Biosensor System Using a CMOS Microelectrode Array Provides High Spatially and Temporally Resolved Images. *Biosens. Bioelectron.* **2018**, *114*, 78–88.

(5) Viswam, V.; Bounik, R.; Shadmani, A.; Dragas, J.; Urwyler, C.; Boos, J. A.; Obien, M. E. J.; Muller, J.; Chen, Y.; Hierlemann, A. Impedance Spectroscopy and Electrophysiological Imaging of Cells with a High-Density CMOS Microelectrode Array System. *IEEE Trans. Biomed. Circuits Syst.* **2018**, *12*, 1356–1368.

(6) Tedjo, W.; Chen, T. An Integrated Biosensor System with a High-Density Microelectrode Array for Real-Time Electrochemical Imaging. *IEEE Trans. Biomed. Circuits Syst.* **2020**, *14*, 20–35.

(7) Lin, X.; Zheng, L.; Gao, G.; Chi, Y.; Chen, G. Electrochemiluminescence Imaging-Based High-Throughput Screening Platform for Electrocatalysts Used in Fuel Cells. *Anal. Chem.* **2012**, *84*, 7700–7707.

(8) Wu, M.-S.; Liu, Z.; Shi, H.; Chen, H.-Y.; Xu, J.-J. Visual Electrochemiluminescence Detection of Cancer Biomarkers on a Closed Bipolar Electrode Array Chip. *Anal. Chem.* **2015**, *87*, 530–537.

(9) Zhai, Q.; Zhang, X.; Han, Y.; Zhai, J.; Li, J.; Wang, E. A Nanoscale Multichannel Closed Bipolar Electrode Array for Electrochemiluminescence Sensing Platform. *Anal. Chem.* **2016**, *88*, 945–951.

(10) Ino, K.; Yaegaki, R.; Hiramoto, K.; Nashimoto, Y.; Shiku, H. Closed Bipolar Electrode Array for On-Chip Analysis of Cellular Respiration by Cell Aggregates. *ACS Sensors.* **2020**, *5*, 740–745.

(11) Iwama, T.; Inoue, K. Y.; Abe, H.; Matsue, T. Chemical Imaging Using a Closed Bipolar Electrode Array. *Chem. Lett.* **2018**, *47*, 843–845.

(12) Defnet, P. A.; Zhang, B. Detection of Transient Nanoparticle Collision Events Using Electrochemiluminescence on a Closed Bipolar Microelectrode. *ChemElectroChem.* **2020**, *7*, 252-259.

(13) Defnet, P. A.; Han, C.; Zhang, B. Temporally-Resolved Ultrafast Hydrogen Adsorption and Evolution on Single Platinum Nanoparticles. *Anal. Chem.* **2019**, *91*, 4023–4030.

(14) Ikegami, M.; Hirano, Y.; Mie, Y.; Komatsu, Y. Fabrication and Characterization of Nanoporous Gold on Microelectrode. *J. Electroanal. Chem.* **2016**, *783*, 188–191.

(15) Li, W.; Rodger, D. C.; Meng, E.; Weiland, J. D.; Humayun, M. S.; Tai, Y. C. Wafer-Level Parylene Packaging With Integrated RF Electronics for Wireless Retinal Prostheses. *J. Microelectromechanical Syst.* **2010**, *19*, 735–742.

(16) Jung, Y. H.; Qiu, Y.; Lee, S.; Shih, T. Y.; Xu, Y.; Xu, R.; Lee, J.; Schendel, A. A.; Lin, W.; Williams, J. C.; Behdad, N.; Ma, Z. A Compact Parylene-Coated WLAN Flexible Antenna for Implantable Electronics. *IEEE Antennas Wirel. Propag. Lett.* **2016**, *15*, 1382–1385.

(17) Trantidou, T.; Tariq, M.; Terracciano, C. M.; Toumazou, C.; Prodromakis, T. Parylene C-Based Flexible Electronics for PH Monitoring Applications. *Sensors.* **2014**, *14*, 11629–11639.

(18) Guerrette, J. P.; Percival, S. J.; Zhang, B. Fluorescence Coupling for Direct Imaging of Electrocatalytic Heterogeneity. *J. Am. Chem. Soc.* **2013**, *135*, 855–861.

(19) Oja, S. M.; Zhang, B. Imaging Transient Formation of Diffusion Layers with Fluorescence-Enabled Electrochemical Microscopy. *Anal. Chem.* **2014**, *86*, 12299–12307.

(20) Macpherson, J. V; Simjee, N.; Unwin, P. R. Hydrodynamic Ultramicroelectrodes: Kinetic and Analytical Applications. *Electrochim. Acta.* **2001**, *47*, 29–45.

(21) Bitziou, E.; Rudd, N. C.; Edwards, M. A.; Unwin, P. R. Visualization and Modeling of the Hydrodynamics of an Impinging Microjet. *Anal. Chem.* **2006**, *78*, 1435–1443.

(22) Macpherson, J. V; Beeston, M. A.; Unwin, P. R. Imaging Local Mass-Transfer Rates within an Impinging Jet and Studies of Fast Heterogeneous Electron-Transfer Kinetics Using the Microjet Electrode. *J. Chem. Soc. Faraday Trans.* **1995**, *91*, 899–904.

VITA

Peter Aaron Defnet (born 1993) spent his childhood in the suburbs of Brookfield, WI and moved to Pottstown, PA following the unexpected passing of his father in 2005. He graduated from Pottsgrove Senior High School in 2011 and attended Juniata College in Huntingdon, PA to study chemistry. In his freshman year, he was fortunate to be accepted into the lab of Professor Richard Hark, where he was inspired by his advisor's contagious enthusiasm for science. Under Richard's strong encouragement, Peter taught himself to code – a skill that would later pay dividends in his life. In his sophomore year, he interned at Applied Spectra Inc, a (then) small Silicon Valley startup run by Lawrence Berkeley National Lab scientists. There he was exposed first-hand to how real scientists operate and obtained his first taste of adulthood and West Coast living. Peter also pursued short-term research projects in the fields of organic synthesis, inorganic synthesis, and electrochemistry before graduating with distinction in 2015. He then joined the lab of Professor Bo Zhang at the University of Washington to pursue his Ph.D. and to study the fascinating field of Nanoscale Electrochemistry.